Mitchell J. Duffy

Development of Translational Optical Imaging Strategies to Assess Inflammatory Biomarkers in Rheumatoid Arthritis

- 2018 -

Biologie

Development of Translational Optical Imaging Strategies to Assess Inflammatory Biomarkers in Rheumatoid Arthritis

Inaugural-Dissertation
zur Erlangung des Doktorgrades
der Naturwissenschaften im Fachbereich Biologie
der Mathematisch-Naturwissenschaftlichen Fakultät
der Westfälischen Wilhelms-Universität Münster

vorgelegt von

Mitchell J. Duffy

aus Davenport, IA, USA

- 2018 -

Dekanin:	Prof. Dr. Susanne Fetzner
Erster Gutachter:	Prof. Dr. Michael Schäfers
Zweite Gutachterin:	Prof. Dr. Wiebke Herzog

Tag der mündlichen Prüfung:	28.11.2018
Tag der Promotion:	13.12.2018

Contents

1 Abstract **1**

2 Introduction **2**
2.1 Rheumatoid Arthritis . . . 2
2.1.1 Causes of Rheumatoid Arthritis . . . 2
2.1.2 Inflammation . . . 3
2.1.3 Cartilage and Bone Destruction . . . 3
2.1.4 Diagnosis . . . 5
2.1.4.1 Laboratory Values . . . 6
2.1.5 Management . . . 7
2.1.6 Role of Imaging in Arthritis . . . 8
2.2 Imaging Modalities . . . 9
2.3 Optical Imaging . . . 10
2.3.1 Fluorescence Reflectance Imaging . . . 10
2.4 Biomarkers for imaging of inflammation in RA . . . 16
2.4.1 S100A9 . . . 16
2.4.1.1 Structure and Function . . . 16
2.4.1.2 Role of S100A8/A9 in RA . . . 17
2.4.1.2.1 Initiation and Leukocyte Invasion . . . 17
2.4.1.2.2 Cartilage and Bone Destruction . . . 18
2.4.1.3 Imaging Strategies for S100 alarmins . . . 18
2.4.2 Matrix Metalloproteinases . . . 19
2.4.2.1 Structure and Function . . . 19
2.4.2.2 Role of MMPs in RA . . . 20
2.4.2.2.1 Inflammation, Invasion and Synovitis . . . 20
2.4.2.2.2 Remodelling and Degradation . . . 21
2.4.2.3 Imaging strategies for MMP activity . . . 22
2.5 Animal Models of Rheumatoid Arthritis . . . 22

3 Aim **25**

4 Materials and Methods **26**
4.1 Materials . . . 26
4.1.1 Fluorescent labels . . . 26
4.1.2 Chemicals . . . 26
4.1.3 Consumables . . . 27
4.1.4 Antibodies . . . 27
4.1.4.1 Primary Antibodies . . . 27
4.1.4.2 Secondary Antibodies . . . 27
4.1.5 Equipment . . . 27

4.1.6 Software . . . 28
4.2 Methods . . . 28
4.2.1 Mice . . . 28
4.2.2 Collagen-induced arthritis (CIA) . . . 28
4.2.3 FRI Imaging . . . 29
4.2.4 Imaging Analysis . . . 29
4.2.5 Immunohistochemistry . . . 29
4.2.5.1 H&E staining . . . 30
4.2.5.2 Immunofluorescence Staining . . . 30
4.2.5.3 Mac-3 / MRP14 Double Staining Immunofluorescence . . . 31
4.2.6 Statistical Analysis . . . 31
4.2.7 Experimental Setup . . . 32
4.2.7.1 Onset group . . . 32
4.2.7.2 Resolution group . . . 32

5 Results **33**
5.1 Onset phase . . . 34
5.1.1 Imaging results show individual inflammation of paws in CIA . . . 34
5.1.2 Two subtypes of disease progression identified . . . 34
5.1.3 Both fast and slow responders show statistically elevated S100A8/A9 and MMP levels on the day of peak inflammation . . . 36
5.1.4 S100A8/A9 and MMP SBRs correlate and are elevated in paws with high clinical scores . . . 36
5.2 Resolution phase . . . 36
5.2.1 Imaging results show inflammation resolution and low SBRs at late time point regardless of paw clenching . . . 36
5.2.2 Imaging of the resolution of a highly inflamed state shows decreasing levels of inflammatory biomarkers. . . . 37
5.3 Histology . . . 39
5.3.1 Morphological findings . . . 39
5.3.2 Immunohistochemistry corroborates target presence beginning at clinical score 2 . . . 41
5.3.3 Late stage disease shows little S100A8/A9 and MMP expression despite high clinical scores . . . 41
5.3.4 Single joint inflammation case study . . . 41
5.4 Analysis Methods . . . 42
5.4.1 Why employ the signal to background ratio? . . . 42
5.4.2 Thresholded SBR Inflammatory Area Analysis Method . . . 45
5.4.3 Thresholded SBR Inflammatory Fraction Analysis Method . . . 45
5.4.4 Receiver Operating Characteristic for optimal threshold determination 45

6 Discussion **49**
6.1 Multiplexing small molecule probes provided novel insight into concurrent expression of MMPs and S100A8/A9 49
6.2 No time shift between the expression of S100A8/A9 and MMPs was found . 50
6.3 Histology corroborated S100A9 and MMP-9 imaging data 51
6.4 Division of onset phase CIA mice into fast and slow responding groups . . . 52
6.5 The clinical score reflects externally observable markers of inflammation . . . 53
6.6 Choice of analysis method and use of signal to background ratio 54
6.7 Blood concentration of tracer is lower in CIA mice 55
6.8 Thresholded SBR Area and Fraction analyses considered 55
6.9 ROC curves indicate limited applicability of thresholding methods 56
6.10 FRI in the clinic 57
6.11 Photoacoustic imaging of Naphthalocyanine labelled ligands presents a 3D diagnostic opportunity 57

7 Conclusions and Outlook **60**

References **I**

Appendix **XVII**

A Abbreviations **XVII**

B List of Figures **XXI**

C List of Tables **XXI**

D Acknowledgements **XXII**

E Curriculum Vitae **XXV**

1 Abstract

INTRODUCTION

Rheumatoid Arthritis (RA) is a progressive and debilitating disease instigated by a loss of tolerance to one's own antigens. Through repeated inflammatory flares, the synovium thickens and both the cartilage and bone of the joints are degraded. Diagnosing a flare early, as well as monitoring the treatment of individual flares and the overall health of the patient are key to reducing morbidity in RA.

Optical imaging techniques such as Fluorescence Reflectance Imaging (FRI) and Photoacoustic (PA) imaging have the potential to improve RA diagnosis and therapeutic monitoring. To this end, we applied FRI in a study of RA progression and resolution, monitoring two biomarkers of inflammation and tissue remodelling.

AIM

We focused on the biomarkers S100A8/9, an alarmin representing an initiator of inflammatory response, and Matrix-metalloproteinases (MMPs), enzymes acting on the extracellular matrix, which are implicated in cartilage and bone destruction and tissue remodeling. We sought to better understand both a trigger (S100A8/9) and a downstream effector (MMPs) protein in the development and resolution of inflammation in RA.

METHODS

Using FRI and novel, fluorescently labelled molecular imaging agents binding specifically to our biomarkers of interest, we were able to follow, longitudinally, for the first time, the activity of S100A8/A9 and MMPs. MRP14 (S100A9) and MMP-9 immunofluorescence was used to confirm imaging findings histologically.

RESULTS

S100A8/A9 and MMP signals were similar throughout the inflammation and resolution phases of disease progression in a murine Collagen Induced Arthritis (CIA) model of RA. Signals were compared with the standard clinical score used to assess the degree of disease progression. Significant differences in signal were observed between highly inflamed paws (above 2 on a clinical score scale of 0 - 3) and controls. The upregulation of the biomarkers at and above a clinical score of 2 was corroborated by histology.

Late in the resolution phase, significant remodelling of the paws was found but while an increase in clinical score was found, the biomarkers of inflammation remained low. Additionally, a case study of single joint inflammation in a low clinical score paw was investigated and found that single joint inflammation was visible both in MMP FRI imaging as well as immunofluorescent histology.

This is the first time small molecule tracers targeting S100A8/A9 and MMPs were used in concert, longitudinally, to assess inflammatory activity in a model of RA. Therefore, several methods of analysis were considered and evaluated in detail for their applicability to this study.

CONCLUSION

This thesis has shown that two biomarkers representing the triggering of inflammation and tissue remodeling can be monitored longitudinally and has laid the foundation for non-invasive, optical, molecular imaging of the progression of RA, which could improve patient monitoring and early flare diagnosis.

2 Introduction

2.1 Rheumatoid Arthritis

Rheumatoid Arthritis (RA) is a chronic and episodic autoimmune disease most commonly associated with joint pain, stiffness and swelling followed by joint degradation (Lee and Weinblatt, 2001). In addition to these localized articular symptoms, RA exhibits a number of systemic effects including destruction of fascia, vasculature, myocardium and more, as summarized in Table 1. These effects taken together make RA a debilitating disease with elevated morbidity and mortality rates and increased comorbidities, particularly pulmonary (e.g. interstitial lung disease), cardiac (e.g. myocardial infarction and stroke), cancer (e.g. lymphoma, leukemia and melanoma), infection and other immune related diseases (e.g. psoriasis and asthma) (Michaud and Wolfe, 2007; van Eijk-Hustings et al., 2012; Maradit-Kremers et al., 2005).

RA has a prevalence of 0.5 - 1% in developed countries and can begin at any age. The onset occurs most commonly in the 5th decade of life though onset is frequent up to the 7th decade of life. RA is a significant disease affecting aging populations (Gabriel, 2001; Alamanos and Drosos, 2005; Silman et al., 2002). RA is found 2 - 3 times more often in women (Alamanos and Drosos, 2005).

2.1.1 Causes of Rheumatoid Arthritis

In recent years, research has revealed multiple factors, which could trigger or promote RA pathogenesis, however, the causes of RA remain unclear. Genetic factors including human leukocyte antigens as well as a number of single nucleotide polymorphisms are associated but not required for RA. It is also believed that bacteria such as mycoplasma, clostridia and *E. coli* as well as viruses such as Epstein-Barr may play a role in triggering RA. Smoking and traumatic/stressful events or periods in life are linked with the induction of RA. It

Table 1: Extra-articular symptoms and conditions related to Rheumatoid Arthritis.
Source: Lee and Weinblatt (2001)

Organ System	**Symptom/Condition**
Skin	Rheumatoid nodules, vasculitis
Ocular	Keratoconjunctivitis sicca, iritis, episcleritis
Oral	Salivary inflammation (sicca symptoms)
Respiratory	Pulmonary fibrosis, pleural effusion, cricoarytenoid inflammation
Cardiac	Pericardial inflammation, valvular nodule formation, myocarditis
Neurological	Mononeuritis, nerve entrapment, cervical instability
Hepatic	Increased aminotransferase concentrations
Haematological	Anaemia, thrombocytosis, leucocytosis, lymphadenopathy, Feltys syndrome: splenomegaly, thrombocytopenia
Vascular	Vasculitis

can therefore be assumed that RA onset is multifactorial, integrating both genetic and environmental factors and triggers (MacGregor et al., 2000; Fassbender, 2002; McInnes and Schett, 2011).

2.1.2 Inflammation

The disease begins with an inflammatory phase, leading to synovitis, an inflammation of the synovium. The processes are depicted in Figures 1 and 2. Resident antigen presenting cells and even synovial mesenchymal cells (SMCs) (Shiozawa et al., 2011) present infectious antigens or autoantigens to T cells, thereby activating them. These T cells proliferate and secrete cytokines attracting more dendritic cells, blood-derived monocytes, T cells, B cells and neutrophils to the synovium (Kremer et al., 2003; Choy, 2012). The B cells continue to present antigen but also differentiate to plasma cells with the help of the now present helper T cells and produce antibodies of the rheumatoid factor (RF) and the anti-citrullinated protein antibody (ACPA) classes and have even been shown to produce antibodies locally in the joint without activation (Cambridge et al., 2003; Reparon-Schuijt et al., 2001; Choy, 2012). Following stimulation by helper T cells and autoantibodies, macrophages secrete large amounts of cytokines such as TNFα, IL-6 and IL-1, further activating a feedback loop (Choy, 2012). Macrophages and their descendants are also key to synovial angiogenesis, releasing angiogenic signals e.g. VEGF and MMPs (Szekanecz et al., 2009). The presence of newly formed vessels further facilitates the influx of leukocytes. The dearth of lymphatic drainage exacerbates joint swelling (Paavonen et al., 2002). As a result of the inflammatory phase, the synovium is remodelled, thickens and develops villi (Fassbender, 2002).

2.1.3 Cartilage and Bone Destruction

Fibroblast-like synoviocytes (FLSs), are one of two cell types composing the lining of the synovium. They exhibit hyperplasia even before infiltration of the synovium by leukocytes and may in fact help drive the inflammatory process of RA (Qu et al., 1994). FLSs hyperproliferate further under a variety of stimuli including growth factors and secreted cytokines such as IL-1β, leading to tumor-like-proliferation (Mor et al., 2005; Shiozawa et al., 2011). This expansion takes place mainly at the synovium-cartilage junction and the resulting mass is called pannus. In order to maintain the expansion, neovascualization occurs. The FLSs mechanically invade the cartilage and bone and under continued stimulation of cytokines, secrete MMPs, which break down the collagen joint matrix of cartilage, rendering it vulnerable to further attacks by the pannus FLSs (Shiozawa et al., 2011). MMP-2 is expressed in normal adult articular cartilage and acts mainly upon type IV collagen but is upregulated in arthritic disease. On the other hand, MMP-9 is only expressed in disease states within articular cartilage and principally by monocytes and macrophages (Rose and Kooyman, 2016). During the course of disease, macrophages are triggered to differentiate into osteoclasts (Boyle et al., 2003) and continue to produce MMP-9 in high amounts. MMP-2 is found near osteoclasts but its cellular origin remains unclear (Andersen et al., 2004). Osteoclasts near the pannus invade

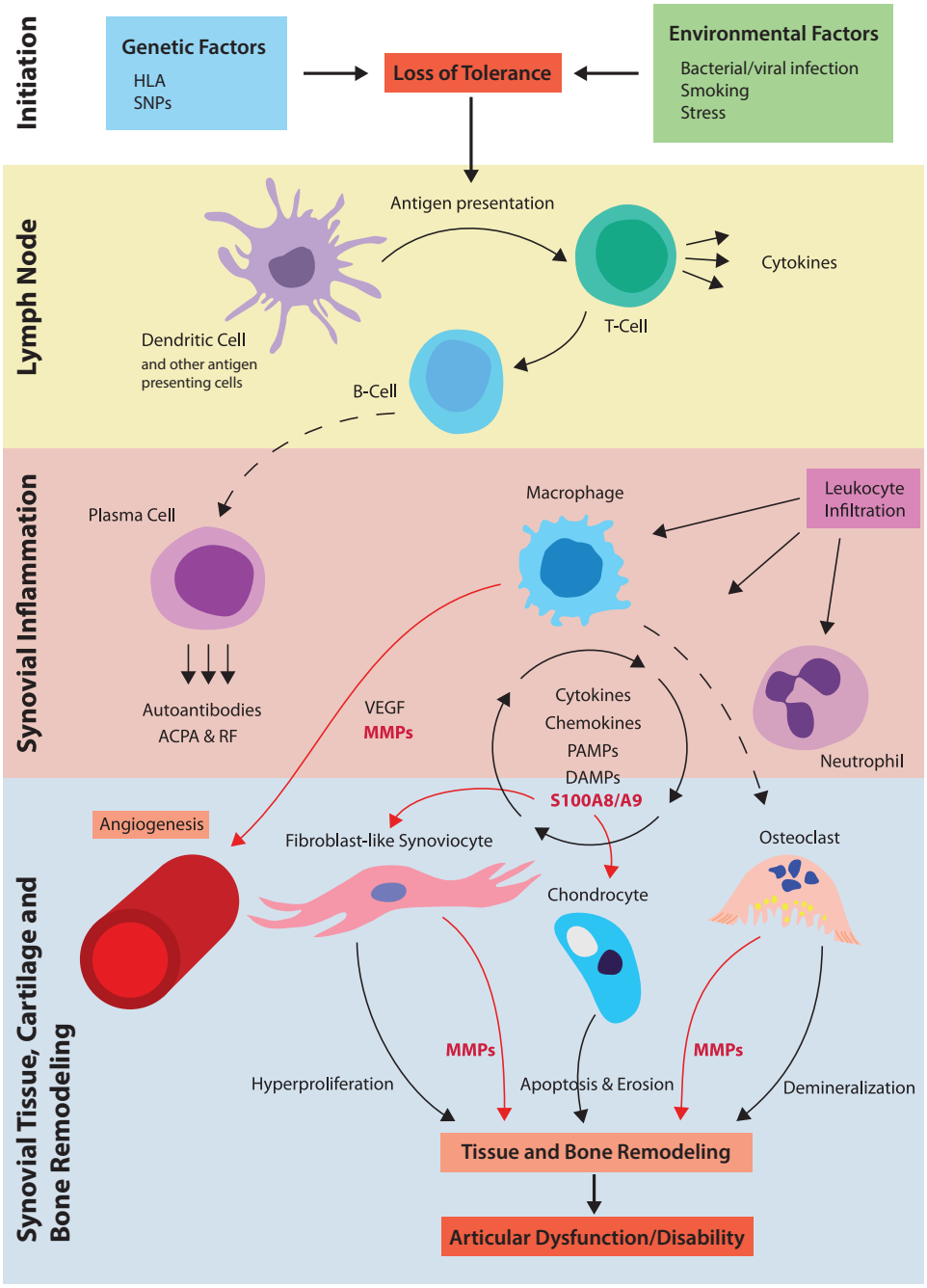

Figure 1: Overview of Rheumatoid Arthritis progression. Cellular component of the initiation and inflammatory flaring of RA. Genetic and environmental factors come together to cause a loss of self antigen tolerance. The dendritic cell, having stimulated the helper T cell sets a cascade in motion, releasing cytokines which recruit leukocytes and cause the differentiation of B cells to Plasma cells producing autoantibodies. Through a milieu of cytokines, chemokines, PAMPs and DAMPs (including, notably, the S100A8/A9 complex) and related signaling pathways, a feedback loop of activation and upregulation of inflammation is created. This in turn leads to structural changes of tissue, cartilage and bone through angiogenesis, chondrocyte death and the action of MMPs and acidic demineralization.

mineralized cartilage and bone (Schett, 2007). This expansion of the pannus and osteoclasts into the bone surrounding the pannus constitutes bone damage detected in conventional X-ray imaging in early RA. As this process subsides, osteoblasts can perform repair. Through the chronic, cyclic, destruction and attempted repair processes inherent to RA, deformation occurs. At end stages of RA, bones on either side of the joint are held together by connective tissue rendering them unusable. This is termed Fibrous ankyloses (Fassbender, 2002).

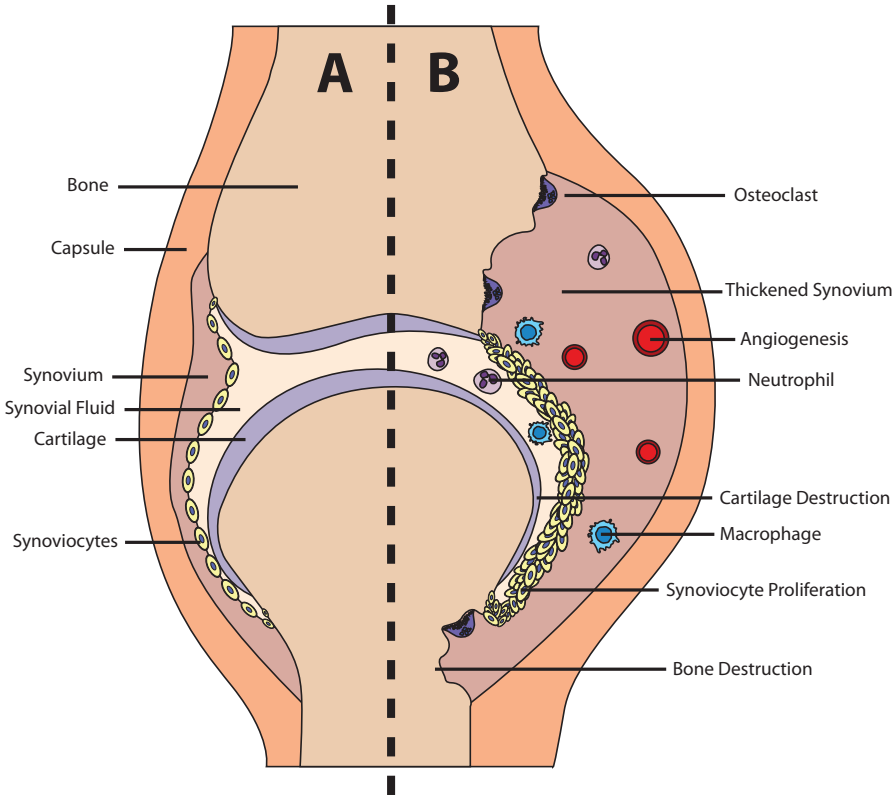

Figure 2: Arthritic Joint. *A* a healthy non-arthritic joint composed of bone, cartilage and an intact synovium. *B* a diseased joint with bone and cartilage destruction by osteoclasts and proliferating synoviocytes, a thickened synovium, angiogenesis and significant leukocyte infiltration

2.1.4 Diagnosis

Current RA diagnostic methods are rather unspecific. While improved methods and earlier treatment have managed to reduce the harm caused by RA, new diagnostics that are able to visualize the inflammatory process, are required in order to improve on these gains and realize an increasingly personalized medicine strategy for RA. The current diagnostic regimen begins through examination of the patient, noting swollen, painful joints and complaints of "morning stiffness", a stiffness upon waking defined as lasting an hour or more. The disease activity score (DAS) is made up of a composite of several scores: the Ritchie articular index, which counts tender joints (Scott and Houssien, 1996), the 44 swollen joint count

(Sokka and Pincus, 2005), the erythrocyte sedimentation rate (see below) and a general assessment of health (Fransen and van Riel, 2009). Taken together, these indicators enable diagnostic assessment and determination of remission. This assessment of disease state is used throughout treatment and monitoring. Standards of care and the rubric of the clinical score are laid out and up-dated regularly (ACR/EULAR, 2010). A significant drawback to these assessments is that they examine consequences of inflammation rather than the inflammation itself and that low, chronic inflammation might be overlooked.

2.1.4.1 Laboratory Values

A standard lab work up in a case where RA, or indeed any auto-immune disease is suspected includes:

Erythrocyte sedimentation rate (ESR) to determine if the joint issues are of rheumatoid, malignant or non-inflammatory origin.

C-reactive protein (CRP) quickly produced in the liver in response to inflammation and easily detectable in circulation as it must travel to the site of inflammation to bind to dying cells and activate the complement system (Thompson et al., 1999).

Rheumatoid factor an IgM antibody that binds to the Fc domain of IgG meaning that it can bind to many different immunoglobulins of this class as the Fc domain is relatively constant. This factor determines the label of the atheride as seropositive or seronegative; seronegative RA constituting up to 20% of cases (Smolen et al., 2016). Additionally, it is a good marker for tracking disease progression and state (Fabris et al., 2010).

Antibodies against Citrullinated Protein/Antigens including Anti-citrullinated protein antibodies (anti-CCP-antibodies), Anti-mutated-citrullinated-vimentin-antibody (anti-MCV), and RA33-antibody are autoantibodies that bind to citrulline, a peptide that is often created in RA by post-translational modification, converting arginine to citrulline. Denaturation of proteins can lead to detection by the immune system and the targeting of citrullinated proteins.

This battery of tests has very high sensitivity and specificity and has been shown to be a set of biomarkers that could be used to predict RA in high risk individuals, detect early inflammatory arthritis, differentiate between different forms of inflammatory disease as well as indicate prognosis and therapeutic direction (Niewold et al., 2007; Fabris et al., 2010; Aggarwal et al., 2009; Lashkari et al., 2014). In particular, the autoantibody titres are of interest as they are predictive of articular destruction and extra-articular manifestations of the disease (Song and Kang, 2010).

Taken together, these values can aid clinicians in the determination of the type of rheumatoid pathology as well as inform clinical decision making. However, they do not contain information regarding the location of inflammation and allow for systemic rather than joint-wise assessment.

2.1.5 Management

Upon diagnosis or a rheumatoid flare, a treatment regimen must be decided upon. This takes into account many factors such as the amount of swelling, if the patient has been treated before, as well as comorbidities (Singh et al., 2015; Smolen et al., 2016). Several treatment options are available to treat rheumatoid flares and maintain remission.

Disease-modifying antirheumatic drugs (DMARDs) are the main treatment for RA. Upon diagnosis they should be applied early and quickly to prevent further progression of disease (Puchner, 2012). Three main types exist: Traditional, Biological and Targeted Synthetic DMARDS.

Traditional DMARDs (also known as conventional synthetic DMARDs) are small molecules used to suppress the immune system in a broad manner. The most often prescribed DMARD, Methotrexate (MTX), belongs to this category. It forms the basis of RA treatment and other DMARDs, if used, are complementary to MTX and serve to modify the treatment regimen as the patient and doctor deem fit.

Biological DMARDs are antibodies or parts of antibodies that block inflammatory cytokines and immunologic processes such as TNF (Weinblatt et al., 2003; St. Clair et al., 2004; Taylor and Feldmann, 2009), IL-1 (Bresnihan et al., 1998; Nuki et al., 2002; Cohen et al., 2002), IL6 (Maini et al., 2006; Smolen et al., 2008), B cell depletion (Edwards et al., 2004; Mélet et al., 2013) and T cell costimulation through CD28 (Östör, 2008). The use of these biologics in combination with MTX has improved patient outcomes in the case where MTX treatment alone was not sufficient.

Recently targeted synthetic forms of DMARDs, Jakinibs, were introduced and have been shown to be effective (Lee et al., 2014; Boyce et al., 2016). The small molecule inhibits the janus kinases which are responsible for intracellular signal transduction of cytokine signalling (Yamaoka, 2016).

Glucocorticoids (GCs) are a type of corticosteroid. Binding cytosolic glucocorticoid receptors they are, principally, translocated to the nucleus where they modify the transcription of proteins regulating inflammation (Buttgereit et al., 2004). GCs are used during rheumatoid flares and as a bridging measure as DMARDs are administered and take effect (Shoenfeld and Meroni, 2012). They are only administered at high doses during flare events due to their wide ranging and severe side effects (Da Silva et al., 2006).

Nonsteroidal anti-inflammatory drugs (NSAIDs) are also used throughout treatment for pain and relieving symptoms but do not modify disease (Crofford, 2013).

The application of DMARDs and GCs, and the efficacy of combination treatments are under continual investigation. Due to side effects of the drugs, their application must be titrated and altered with the course of a flare (Kłak et al., 2016). By the time a patient has begun to notice symptoms, the detrimental effects of the oncoming flare have already begun. The potential for new strategies to diagnose a flare before it begins would alleviate suffering and damage as well as allow for reduced administration of pharmaceuticals with detrimental side effects. Further studies combining molecular imaging of inflammatory state with particular

treatment regimens could lead to a more personalized approach to disease treatment, deducing which drugs might be most effective for an individual and tailoring dosage of those drugs over time.

2.1.6 Role of Imaging in Arthritis

Despite the usefulness of the aforementioned markers, they lack the ability to assess the extent of disease, anatomical changes and distribution of cellular and/or molecular effectors of disease. It was recently shown by Frank-Bertoncelj et al. (2017) through the collection of synovial fluid from a number of joints that epigenetic and gene expression modifications in fibroblasts created different microenvironments in each of the joints leading to anatomically specific outcomes. This provides further impetus for a local, joint specific assessment of biomarker distribution as opposed to measuring systemic biomarker values. To this end, morphological and functional imaging is used routinely in clinical practice at all stages of disease. A number of techniques are available and are used in concert.

X-ray imaging is used in order to monitor the progression of disease and document bone erosion. It can also be useful in diagnosis of early RA due to the visualization of juxtaarticular osteoporosis (Duncan and Riddle, 1986). The spinal column can also be imaged in RA. X-ray and related computed tomography (CT) have, however, fallen out of favor due to their limited diagnostic potential as inflamed soft tissues cannot be imaged using this technique (Tins and Butler, 2013).

Ultrasound (US) can be used to monitor changes in the synovium, bone and joint fluid. It is used both as a diagnostic and to monitor disease progression. It is particularly advantageous as it can be performed quickly, cheaply and directly by physicians in the examination room. Compared with clinical examination, US performs better when assessing synovitis (Kane et al., 2003). Bone erosions are detected with higher sensitivity using US when compared with X-ray (Patil and Dasgupta, 2012).

Magnetic resonance imaging (MRI) is well suited to RA as it is able to visualize effects on a number of tissues simultaneously. Not only can bones be investigated but soft tissues and fasciae can be visualized. Synovial volume, as well as bone erosions and edema within the marrow can be monitored longitudinally and non-invasively (Hodgson et al., 2008).

Multiphase bone scintigraphy can be used in order to image the bone but also the blood pool and perfusion (Kim et al., 2016). Using a technechium-99m labelled (di- or tri-) phosphonate, the activity of osteoblasts integrating the phosphonate into the bone, as well as non-specific uptake in inflamed areas can be visualized.

X-ray, US, and MRI provide pertinent anatomical information while bone scintigraphy is a functional imaging technique allowing the clinician to determine the activity of osteoblasts responding to the bone destruction process non-invasively. However, none of the above imaging techniques provide direct information about inflammatory activity. Early diagnosis and long term monitoring of RA flares is a long term goal of personalized medicine in rheumatology. Developing non-invasive, cost effective and time efficient strategies for use

in clinics and even the offices of rheumatologists would give doctors the ability to monitor patients more closely and regularly, detecting changes in biomarkers before their symptoms begin. To this end, the development of molecular imaging techniques targeting inflammation in RA is the goal of this work.

2.2 Imaging Modalities

In order to investigate biomarkers, one can draw blood or other fluids. One can also take a biopsy of a particular tissue and perform immunohistochemistry, probing for particular biomarkers. These are useful clinical tools but they fail to capture distributions of the biomarkers outside of a narrow scope. They are limited by tissue availability and by possible sampling error (Mulholland and Doherty, 2006; Corcoran et al., 2012). Molecular imaging, on the other hand, is able to depict, across a broad scale of fields of view, the underlying distributions of molecular biomarkers in time and space non-invasively.

A number of modalities have been developed which allow researchers and physicians to assess anatomy and function. As mentioned before, X-ray and CT are available but mainly assess anatomy. MRI, is mostly used for anatomical assessments but is also widely used in molecular imaging. It has the drawback of having a sensitivity too low to assess many biomarkers (Figure 3) (Kiessling et al., 2017). Ultrasound provides anatomical information and in some cases, using targeted microbubbles for instance, can be an interesting molecular imaging tool but the size of the microbubbles confines them primarily to the circulatory system (Wang et al., 2018) and whole body assessments are difficult. The advantages of ultrasound can be combined with optical imaging to produce a hybrid modality called photoacoustics. Given

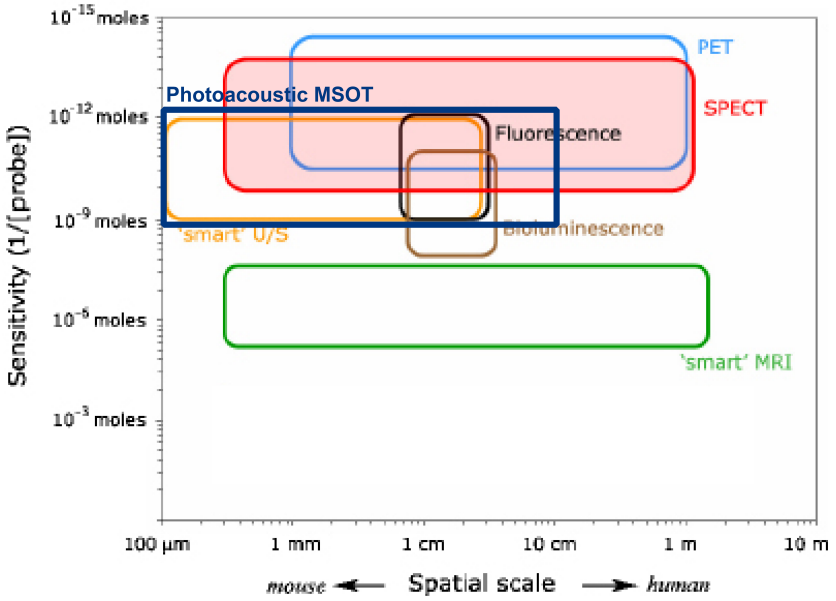

Figure 3: Imaging modalities as a function of sensitivity and spatial scale. *Source: modified from Meikle et al. (2005) with information from Razansky et al. (2009)*

that we are looking at distributions of biomarkers for which we require high sensitivity, we have the choice of nuclear and optical imaging modalities.

Nuclear imaging has very good sensitivity and also a large field of view, allowing for full body measurements in preclinical imaging and with the potential to capture full body images in humans if multiple bed positions are acquired. It has the drawback, however, that the infrastructure is costly to set up and maintain. Positron emission tomography (PET) and single photon emission computed tomography (SPECT) machines are expensive and depending upon the isotope and kind of scan desired, require a cyclotron, generator or expensive shipment of radioactive materials. This limits the applicability of the techniques in both research institutions and clinics. Nuclear imaging also carries a radiation burden for the patient who receives it (Kiessling et al., 2017). A PET/CT for instance can be equivalent to 1 - 8 years of average background radiation (Boellaard et al., 2015; Beiderwellen et al., 2015).

We, therefore, chose to develop in the direction of optical imaging. These techniques do not require patients to receive radiation doses and the tracers (another name for probes, which can be used in small or "trace" amounts and bind to or "trace" a particular target) can be shipped and stored easily (Kiessling et al., 2017). Optical imaging systems are also cheaper and with small footprints, could even be incorporated into small clinics or the offices of general practitioners for frequent monitoring of patient health. They have the drawback of only being able to image superficially relative to modalities such as nuclear imaging, due to absorption and scattering of light in tissue. This leads to a loss of sensitivity and makes quantification difficult. It also reduces the number of applications for which optical imaging can be used.

Finally, it is important to note that although we chose to focus on optical imaging, these probes could, in the future be further radiochemically modified should a PET or SPECT tracer be of interest to a particular preclinical or clinical application. The development path chosen is not exclusive, and optical tracers often serve as a proof of concept and characterization method, as a step toward radiotracer development.

2.3 Optical Imaging

2.3.1 Fluorescence Reflectance Imaging

Optical imaging techniques, using light to produce images, are a set of powerful tools used throughout medical practice and are among the most used medical imaging techniques. One could argue that the simple visual checks that a doctor performs constitute optical imaging, but the beginning of optical imaging is usually accredited to the discovery of microscopy over 400 years ago. Microscopy, and later telescopy, were the impetus for the continued study of light and its properties, and its use to this day enables physicians to diagnose patients through the analysis of immunohistochemical images (Mait, 2006). Beyond normal white light microscopy, a number of other microscopy technologies have been developed including fluorescence, confocal, super resolution and total internal reflectance which are useful both for medical and basic science applications (Stephens and Allan, 2003; Huang et al., 2009).

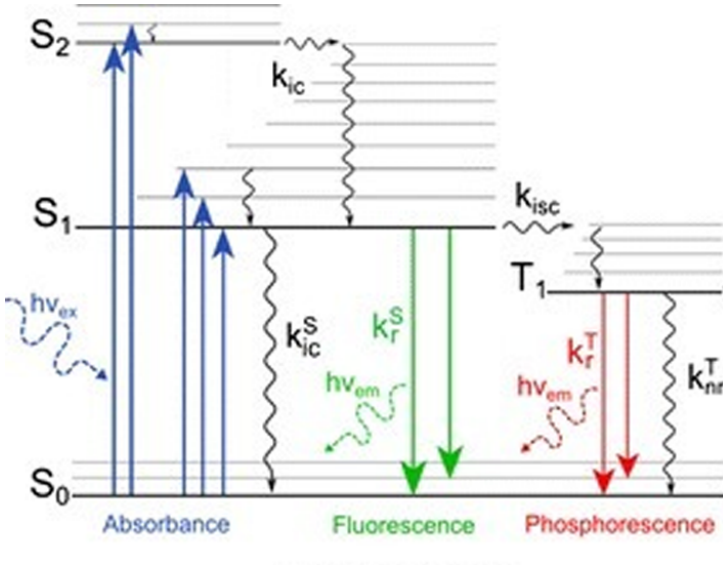

Figure 4: Jablonski diagram. Generic Jablonski diagram depicting the excitation (hv_{ex}) of an electron from the ground state (S_0) to an excited singlet state (S_1, S_2). Within all states there exist vibrational states, depicted as grey lines. The radiationless transition from a singlet excited state to either another singlet excited state or the ground state takes place through internal conversion (k_{ic}). A transition from S_1 to S_0 with the emission of a photon (hv_{em} in green) is fluorescence (k_r^S). The transition from a singlet state to a triplet state (T_1) is called intersystem crossing (k_{isc}). Non-radiative decay from T_1 to S_0 (k_{nr}^T) and radiative decay, termed phosphorescence (k_r^T) emitting a photon (hv_{em}). Taken together they represent the basic avenues of electron excited state resolution in photophysical chemistry. *Source: modified from Quaranta et al. (2012)*

Optical imaging is not only limited to microscopy, however. The scale of mesoscopy (the imaging of a set of tissues) and even macroscopy (the imaging of whole organs, systems or organisms) can also be imaged using photographic imaging, bioluminescence imaging (Sadikot and Blackwell, 2005), Cherenkov imaging (Thorek et al., 2012) and PA imaging. Additionally and specifically, FRI will be examined in further detail.

Fluorescence reflectance imaging allows for preclinical imaging of entire organisms and can be used in the clinic for non-invasive examinations of sections of the body e.g. breast (van de Ven et al., 2009) or lymphatic system (Ohnishi et al., 2005). The bulk distribution of a tracer or fluorescent reporter gene can be visualized using this method.

Light is shined onto a sample or experimental organism. The light penetrates and is absorbed by a molecule, exciting one of its electrons. A molecule excited by incoming light can relax its excited electron via a number of paths as depicted in a Jablonski diagram (Figure 4). One path available to it is fluorescence, where a light of lower energy (longer wavelength, lower frequency, red-shifted) is emitted. Some of these emitted photons will be reflected back out of the sample or organism and picked up by a detector. Different molecules producing fluorescence, termed fluorophores, have different wavelengths of peak excitation and emission. The difference between these is called the Stokes shift (Schulz and Semmler, 2008).

Taking advantage of this principle and the Stokes shift, fluorescent imaging uses a raster scanning laser or white light source and a low pass filter to illuminate a target with a chosen band of light. The reflected source light and the resulting emitted fluorescent light travel towards a detector and a low pass filter is used to prevent the source light from reaching the detector (Ntziachristos et al., 2003). This concept is depicted in Figure 5.

As different fluorophores have different excitation and emission wavelengths, two or more may be used simultaneously if none of these peaks overlap and given the correct filter sets. This is how multiple targets can be imaged in fluorescence microscopy to create multicolour images but can equally be used in macroscopic FRI to image multiple tracers within a single sample or organism (Kosaka et al., 2009).

Within an *in vivo* context, there are windows of opportunity where the absorption of electromagnetic (EM) radiation is at its lowest.

It is these windows that imaging modalities use in order to achieve the penetration needed to get the radiation into a body and back out to a detector. Three main windows exist as illustrated in Figure 6. The X-ray window utilizes the differential absorption of tissue types. A higher atomic number (Z) absorbs X-rays more readily, allowing calcium (Z = 20) and other elements constituting bone to attenuate the X-ray to a greater extent than soft tissue made of hydrogen, carbon, nitrogen and oxygen with an average Z of 7.068 (Janker, 2013), calculated from (Griffiths, 1989). On the other end of the spectrum, radio waves are used in Magnetic Resonance Imaging (MRI) in order to excite nuclear spin energy transitions and to read out the radio signals produced, principally by water protons, within the sample or organism being examined (Guy and Ffytche, 2005). It is because of this radio frequency window of low absorption that full body, high resolution MRI scans are possible (Kiessling

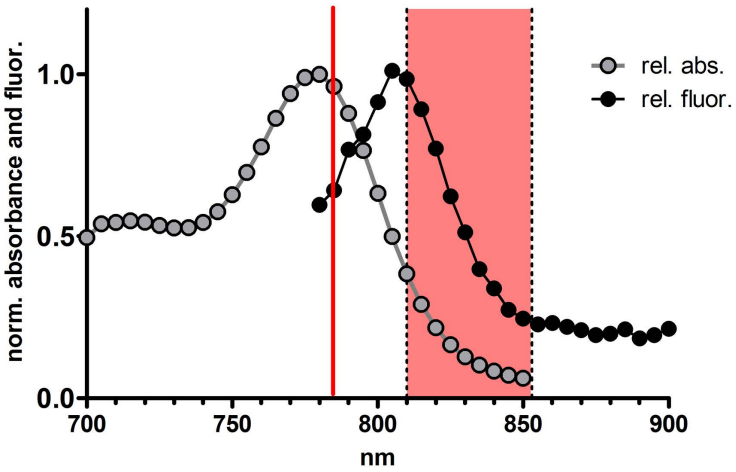

Figure 5: ICG fluorescence characteristics. ICG relative normalized absorption (grey) and fluorescent emission (black) spectra. The excitation cut-off filter (red line) and the emission filters (black dotted lines bordering the red zone) are also depicted. The difference between the peak absorption and fluorescence emission is termed the Stokes shift. *Source: modified from Jonak et al. (2011)*

et al., 2017). We are principally interested in the optical or near-infrared (NIR) imaging window, between regions of visible light, in which pigments contained in the body and Rayleigh scatter contribute to signal loss and the deeper infrared and microwaves where vibrational absorption, principally of water, a major component of *in vivo* systems, reduces the penetration and recovery depth of optical signals (Pogue, 2015).

NIR FRI falls under the term diffuse optical imaging. This term arises from the fact that the light is shined across the surface of the sample or animal (Gibson and Dehghani, 2009). In NIR imaging there is little influence of autofluorescence because natural *in vivo* fluorophores are principally excited in the ultraviolet (UV) and visible light spectrum (Monici, 2005). Two main types of interactions, absorption and scattering, play a significant role in the alteration and loss of signal which makes fluorescence imaging a challenge (Ntziachristos, 2006).

Absorption, while an order of magnitude lower in the NIR as compared to the visible spectrum, serves to reduce the amount of light reaching the fluorophore. The light emitted by the fluorophore must also be recovered from within the tissue and some light is also absorbed on the path between emission and detection as it passes through the body (Stuker et al., 2011).

Absorption follows the Beer-Lambert Law which states that the intensity at a given point within a uniform absorber is: $I = I_0 e^{-\mu d}$

This means that the intensity I observed decays exponentially based on the decay coefficient, μ, and the distance travelled, d, from its original intensity I_0. So the loss of signal on the way in and then back out is exponential (Sauer et al., 2011).

Scattering is the main effect distorting FRI images. Similar to absorption it acts both on excitation and emission light as it moves through tissue. Ballistic light, photons which have yet to be absorbed and reemitted by a particle, have a very limited penetration depth

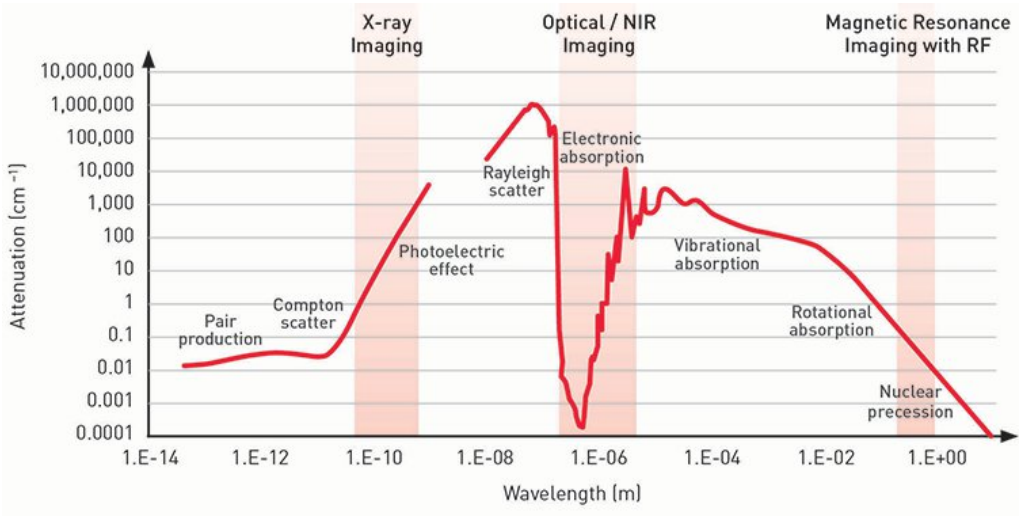

Figure 6: Imaging windows in the electromagnetic spectrum. The red areas demarcate sections of the electromagnetic spectrum amenable to imaging due to their low electromagnetic absorption in human tissue. *Source: Pogue (2015)*

(about 100 µm in tissue), which also follow the Beer-Lambert Law. The average distance travelled by a photon between interactions is called the mean free path (MFP) (Schulz and Semmler, 2008). This value is medium, and in the *in vivo* case, tissue, dependent. Due to the anisotropic (directional) scattering of light in tissue medium at NIR wavelengths, the average photon may be scattered at 100 µm in tissue but it is not directionless (random walk). The average distance until the direction of a photon in a scattering medium becomes random is termed the transport mean free path (TMFP) and this is the important consideration for fluorescence imaging as beyond this depth, the distribution of the information that is received will be random. Due to this directionality, the TMFP for breast tissue is between 1 mm and 3 mm as compared to the MFP of 100 µm (Shi and Alfano, 2017).

On the way to the fluorophore, scattering distributes the excitation light more evenly throughout the tissue volume. But for the emitted light, it creates blurring and imprecision with higher intensity and more accurately depicted light coming from closer to the surface. The three dimensional nature of tissue means that two dimensional images of samples and organisms contain volume related artifacts (Ntziachristos, 2006). The distribution at depth may not be able to be retrieved and the contribution of fluorophores at depth will not be as strong. For this reason, applications in which the target tissue is thin or near the surface are preferable (Stuker et al., 2011).

Attempts to overcome the volume problem have been made; photoacoustic imaging, to be discussed later, and Fluorescence Molecular Tomography (FMT). FMT creates tomographic, whole body, 3D fluorescence images localizing fluorophores either by using multiple light sources and detectors in a ring around the sample and moving the sample through this ring, or using one light source and detector but rotating the sample, similar to CT (Li et al., 2010). This modality utilizes complex models of photon behavior to solve the inversion problem but still has limited resolution, especially at depth (1 mm to 1 cm) (Stuker et al., 2011).

Planar NIR FRI is a commonly used preclinical imaging modality with its ease of image acquisition and its non-invasive nature (Graves et al., 2004). Due to the aforementioned depth limitations, it is often used in small animals such as mice and is of greatest use in models of neurological, cardiovascular (Leblond et al., 2010) and dermatological diseases (Ra et al., 2015), subcutaneous or brain tumors (Martelli et al., 2016), inflammatory diseases such as RA (Put et al., 2014) and *ex vivo* examination of organs (Figure 7B). Depending upon the setup of the experiment, type and concentration of the dye and the size of the organism, it is possible to visualize the superficial organs, such as the kidneys, bladder, lungs and spleen (Figure 7A). This makes FRI well suited to longitudinal studies or applications where corroboration of other modalities is needed (Leblond et al., 2010).

In the clinic, it has a number of promising applications. The short acquisition times, in comparison with other modalities, which may require reconstruction, mean that surgeons can inspect images in real time during a resection. This has led to the growing field of image guided surgery (Schols et al., 2015). In the case of metastatic cancers, migrating cells often colonize draining lymph nodes, termed sentinel lymph nodes. The injection of the FDA approved Indocyanine Green (ICG) at the site of the tumor allows clinicians to follow the

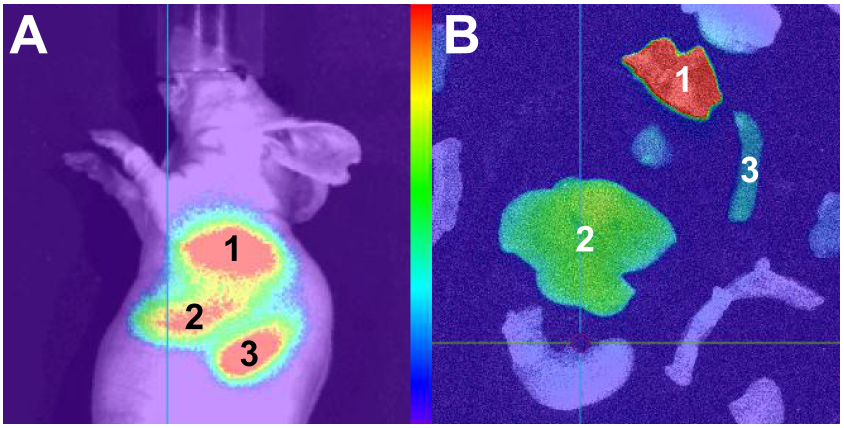

Figure 7: FRI images of tracer distribution in organs *in vivo* and *ex vivo*. Images of IRDye 800CW labelled nanoparticles and their uptake in the (1) lungs, (2) liver, (3) spleen. (A) *in vivo* image showing nanoparticle uptake in superficial organs. (B) *ex vivo* image of the organs of the mouse pictured in A.

lymphatic system using fluorescence imaging as it drains the ICG and pinpoints potentially compromised nodes, marking them for surgical removal (Marshall et al., 2010).

We are hoping to implement molecular FRI in arthritis monitoring. Initial studies of fluorescence in arthritis also used ICG due to its FDA approval. By analyzing differences in the influx and egress of the dye within joints of the hands, clinicians were able to compare the fluorescence technique to standard techniques using MRI and US (Glimm et al., 2016; Krohn et al., 2015; Werner et al., 2013; Fischer et al., 2010; Bremer et al., 2009). Each paper concluded that FRI showed promise and produced results that were comparable with established techniques. The process takes only a few minutes to perform and is more comfortable and cost effective for patients when compared with MRI. While this technique is interesting and easily implemented in clinics, it utilizes a non-specific perfusion based tracer. The use of a molecular imaging probe that specifically targets biomarkers could enhance the contrast and allow for more accurate assessment of inflammatory processes beyond edema and the enhanced permeability and retention (EPR) effect, whereby substances diffuse from malformed or leaky vessels into tissues and are not readily taken up again.

A number of fluorescently labelled probes have been tested preclinically in animal models of arthritis in order to assess their ability to visualize biomarkers of inflammation and destruction. In transgenic mice expressing luciferase concurrently with NF-$\varkappa$B expression, a model of arthritis was imaged (Carlsen et al., 2002). Macrophages have been common imaging targets in models of arthritis due to their crucial role in the progression of disease. Imaging of F4/80 positive macrophages, which are known to gather in arthritic joints, using an antibody labelled with the NIR dye Cy5.5 (Hansch et al., 2004), and folate imaging to detect activated macrophages (Chen et al., 2005), have been conducted. E-selectin antibodies were imaged to assess endothelial activation in a model of RA (Gompels et al., 2011). Cathepsin and MMPs were also imaged using activatable probes in a terminal study of RA and osteoarthritis (OA)

models of arthritis (Vermeij et al., 2014). Further use of multiplexed activatable probes by Scales et al. (2015) assessed MMPs and Cathepsin K, in addition Neutrophil Elastase and a non-specific Cathepsin were also examined. An anti-S100A9 antibody conjugated to a Cy5.5 dye was examined in collagen induced arthritis (CIA) at one time point (Vogl et al., 2014). Taken together, some very interesting and varied investigations of the underlying mechanisms of RA have been examined using targeted probes in FRI molecular imaging.

2.4 Biomarkers for imaging of inflammation in RA

Molecular imaging techniques, e.g. FRI and PA, visualize the underlying distributions of biomolecules within an organism. So it is not only the technology and labelling, but also a biologically relevant discrepancy between a disease or disease model state and a healthy, wild-type or control state, known as a biomarker, which enables molecular imaging. Although numerous biomarkers of inflammation in RA exist, we selected two which would target distinct stages of the inflammatory process. The first, S100A8/9 acts as an "alarmin", upstream initiator and regulator of cytokine and MMP production. Second, we chose the MMPs themselves due to their crucial role in the remodelling and destruction phases. In this way, we can analyse both an inflammatory initiator and an induced destructive mechanism. Both S100A8/9 and MMPs are highly expressed in many models of inflammation, hinting at further applications in other inflammatory diseases outside of RA.

2.4.1 S100A9

2.4.1.1 Structure and Function

S100A9, also known as MRP14, L1 or calgranulin B, is a member of the Ca^{2+} binding S100 family of proteins. S100 proteins are members of a larger EF-hand family, characterized by their ability to bind Ca^{2+} in a helix-loop-helix domain. S100A9 is small at around 13 kDa and is made up of 114 amino acids in humans (Itou et al., 2002). S100 proteins usually exist in dimers or tetramers, S100A9 is peculiar in that it preferentially creates heterodimers with S100A8 (MRP8, calgranulin A) (Korndörfer et al., 2007). This dimer of S100A8/A9 is also referred to as calprotectin. Dimerization is achieved through a denaturation and renaturation within granulocytes, allowing the proteins to achieve their quaternary structure. Tetramerzation requires a bivalent ion, either Ca^{2+} or Zn^{2+} (Vogl et al., 2006; Leukert et al., 2005).

S100A8/A9 is found to be a driver of inflammation and deleterious processes in many diseases, such as autoimmune disorders, inflammation both acute and chronic, atherosclerosis, cancer, cardiac disease and neurodegenerative diseases (Vogl et al., 2012; Averill et al., 2012; Shepherd et al., 2006; Markowitz and Carson, 2013; Foell and Roth, 2004). Its function and further research into the intricate role it plays in disease onset and progression is of the utmost interest.

S100A8/A9 is produced in cells of myeloid origin. Neutrophil cytoplasm and monocyte

membranes contain high concentrations - around 45% and 1% respectively (Dale et al., 1983; Bhardwaj et al., 1992; Roth et al., 1993; Hessian et al., 1993). Macrophages also express S100A8/A9 (Odink et al., 1987). Additionally, it was found to be expressed by platelets after myocardial infarction (Wang et al., 2014), in endothelium, causing changes to its permeability (Viemann et al., 2005; Wang et al., 2014), in epithelial cells during wound healing and abnormal skin conditions (Thorey et al., 2001; Henke et al., 2006; Gebhardt et al., 2006) and in osteoclasts during bone resorption (Zreiqat et al., 2007). In addition to being found within cells, it is released extracellularly as a damage-associated molecular pattern (DAMP) with a function similar to a cytokine or chemokine. It is secreted from myeloid cells through an alternative and tubulin dependent pathway as it has no secretion signal, and can also be released during cell death (Rammes et al., 1997; Foell and Roth, 2004).

Once extracellular, it can interact with Toll-like receptor 4 (TLR4) (Vogl et al., 2007) and the receptor for advanced glycation end products (RAGE) (Boyd et al., 2008), though it is unclear to what extent the latter has an intracellular effect (Leclerc et al., 2009). By binding these receptors the NF-$\varkappa$B, p38 MAPK, IRAK, ERK and PKC pathways can be activated (Riva et al., 2012; Wu et al., 2015; Kwon et al., 2013; Ehrchen et al., 2009). These have a plethora of effects depending upon cell type.

2.4.1.2 Role of S100A8/A9 in RA

2.4.1.2.1 Initiation and Leukocyte Invasion

In the initial stages of rheumatoid arthritis, S100A8/A9 plays a key role in endothelial activation, which increases permeability of vasculature (Srikrishna et al., 2001; Wang et al., 2014). Within the endothelial cells, there is an increase in inflammation response (Viemann et al., 2005), releasing cytokines and chemokines including IL-6 (Ehlermann et al., 2006).

Neutrophils are recruited from the vasculature through the process of rolling and adhesion. S100A8/A9 regulates this process through TLR4 activation of RAP1-GTP, which in turn activates β2 integrins. These integrins interact with ICAM-1 to slow and adhere the rolling neutrophil in the area of inflammation (Pruenster et al., 2015). Populations of neutrophils remain high due to the suppression of apoptosis by a TLR4 and CD11b/CD18 activated MEK-ERK pathway (Atallah et al., 2012). Due to the fact that neutrophils contain a high amount of cytoplasmic S100A8/A9, they are able to secrete it upon arrival, without the need for transcription. This could be a driver of the initial inflammatory phase (Cesaro et al., 2012).

Similar to neutrophils, monocytes also express higher levels of CD11b, allowing for their extravasation and accumulation at sites of inflammation (Bouma et al., 2004). Monocytes treated with S100A8/A9 were found to produce TNFα, IL-1β, IL-6 and IL8 (Sunahori et al., 2006; Bhardwaj et al., 1992). Monocytes treated with TNFα and IL-1β show upregulation of S100A8 and S100A9 (Suryono et al., 2005). Infiltrating monocytes are activated by S100A8/A9, upregulating their expression of proinflammatory cytokines through the NF-$\varkappa$B and p38 MAPK pathways. S100A8/A9 expression within macrophages may be upregulated

by TNFα, IFN-γ and IL-10 (Xu and Geczy, 2000; Xu et al., 2001), so there is a possibility for a positive feedback loop involving S100A8/A9, NF-κB and TNFα/IL-1β.

In addition to the extracellular function, S100A8/A9 also plays a role in the cytoskeletal arrangement within phagocytes. The heterotetrameric form of S100A8 and S100A9 serves to stabilize tubulin filaments, creating microtubules. Heterotetramers are formed through the binding of Ca^{2+}, thus as the calcium concentration is increased, the heterotetramers bind the ends of microtubules. As a counteracting force, the phosphorylation of S100A8/A9 can lead to a net breakdown of tubulin. The transendothelial migration of phagocytic cells is controlled by this process, in which the cytoskeleton is rearranged (Vogl et al., 2004; Leukert et al., 2006).

2.4.1.2.2 Cartilage and Bone Destruction

Chondrocytes of murine origin in the antigen induced arthritis model and a spontaneous arthritis model were found to express high levels of S100A8 and S100A9. When stimulated with TNFα, IL-1β, IL-17 and IFN-γ, S100A8 and S100A9 were upregulated. When chondrocytes were stimulated with S100A8, there was a significant upregulation of MMPs and other metalloproteinase mRNAs (Lent et al., 2008b). This was also tested using the cartilage of patients with osteoarthritis, where chondrocytes binding S100A8/A9 to TLR4 induce upregulation of MMPs and cytokines IL-6 and IL-8 (Schelbergen et al., 2012). S100A8 and S100A9 cause chondrocytes to take on a phenotype of cartilage catabolism (Schelbergen et al., 2010). So it is through this S100A8/A9, and therefore S100A9 dependent triggering of TLR4 and the NF-κB pathway, that a link to MMPs and their upregulation is created. Additionally, it has been posited that bone erosion by osteoclasts in RA may also be affected by S100A8/A9 (Cesaro et al., 2012). It is also speculated, through RAGE signalling that S100A8/A9 stimulates invasive behavior in RA FLSs (Steenvoorden et al., 2007). S100A8 binding of TLR4 in FLSs was shown to elevate the expression of IL-6 (Lee et al., 2013).

In summary, S100A9 and its binding partner S100A8 as S100A8/A9 play a number of roles in the regulation of immune response. Its ability to affect the progression of RA is of particular interest to this thesis. Through a positive feedback mechanism it is able to aid in the recruitment and extravasation of immune cells leading to leukocyte invasion and swelling within the synovium. Additionally, S100A8/A9 increases the production of MMPs, a rate limiting destructive force in cartilage and bone resorption and remodelling.

2.4.1.3 Imaging Strategies for S100 alarmins

Imaging of S100A8/A9 has been conducted recently, predominantly through optical imaging using labelled antibodies (Vogl et al., 2014; Becker et al., 2015; Geven et al., 2016). This strategy has proven that S100 imaging is possible and helped interrogate S100A8/A9's role in inflammation across a number of disease models. However, it has the drawbacks that the half-lives of antibodies are quite long, making serial imaging difficult and reducing translational potential.

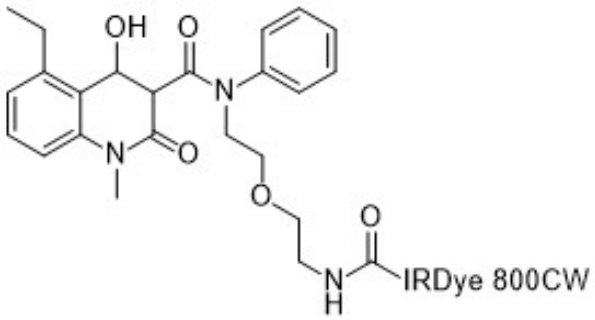

Figure 8: CES271-IRDye 800CW, S100A8/A9 tracer.

In order to monitor local inflammation activity of S100A9 and by proxy S100A8/A9, a small molecule ligand with the ability to be labelled, CES271 (Figure 8), was developed in our group. Its attachment to a fluorescent probe allows for visualization of the inflammatory process as shown in a proof-of-principle study by Faust et al. (2015). As a small molecule ligand, it has faster excretion characteristics and is more easily translatable as it has less time to create off target effects and immune reactions. It was used to track the progression of the CIA model of RA in mice. In particular, the interplay of S100A8/A9 and the downstream activation of MMPs were of interest.

2.4.2 Matrix Metalloproteinases

2.4.2.1 Structure and Function

Matrix-metalloproteinases (MMPs) represent a family of 23 zinc-dependent endopeptidases which are involved in the degradation of components of the extracellular matrix (ECM). Highly conserved in vertebrates, MMPs perform a central role in remodelling tissue but also have regulatory roles in the activation of cytokines, chemokines and growth factors (Loffek et al., 2011; Van Lint and Libert, 2007). They play a key role in physiological and pathological states, including heart and vascular disease, cancer, brain disorders, inflammatory diseases and skeletal remodelling (Malemud, 2006).

MMPs, canonically, are made up of five parts: an extracellular localization peptide, a propeptide, a catalytic region, a linker region and a hemopexin region. Within the catalytic region, three histidine residues coordinate around a zinc ion. A cysteine on the propeptide also coordinates, blocking the binding of a required water molecule and rendering the proMMP inactive. Extracellularly, the propeptide must be cleaved away to activate the MMP. This is done in a "stepwise" activation, whereby a wide range of proteinases, including those from other organisms such as bacteria, cleave a "bait" region away. Following this, other MMPs will cleave the rest of the propeptide away, rendering it an active MMP (Nagase et al., 2006).

MMPs are grouped based on their respective principle substrates. Collagenases include MMPs 1, 8, 13, and 18. Gelatinases include MMPs 2 and 9. The remaining MMPs belong to the Stromelysins, Matrilysins, Membrane-Type MMPs (MT-MMPs), which have a transmembrane

domain and some other, less easily classifiable MMPs like the Macrophage metalloelastase MMP-12 (Verma and Hansch, 2007).

As rampant degradation of the ECM would lead to disease, MMPs are controlled through alpha-2-macroglobulin and tissue inhibitors of matrix metalloproteinases (TIMPs). Alpha-2-macroglobulin, which is mainly active in fluids (Tchetverikov et al., 2003; Brew et al., 2000), encapsulates MMPs and other proteinases, rendering them inactive. TIMPs inhibit by chelating the zinc ion in the MMP active site with their N-terminus (Brew et al., 2000; Loffek et al., 2011). Four TIMPs have been identified, and they each inhibit different MMPs preferentially. Some TIMPs also play a role in the activation of MMPs, for example, proMMP-2's hemopexin domain requires an interaction with TIMP-2's C-terminal domain in order to be activated by MT-MMPs (Brew et al., 2000). The homeostatic balance of MMPs and their inhibitors is disrupted in arthritis (Yoshihara et al., 2000). Recent studies suggest that the modulation and dysregulation of epigenetic factors plays a key role in heightened production of MMPs by FLSs (Araki and Mimura, 2017).

2.4.2.2 Role of MMPs in RA

2.4.2.2.1 Inflammation, Invasion and Synovitis

MMPs are active even during the initiation of inflammation in RA. They play an integral role in the influx of leukocytes to the synovium. Migration of myeloid cells is improved by secreted and membrane bound MMPs, as they are able to cut through ECM blocking their path (Chou et al., 2016). Cell adhesion molecules such as CD44 can be cleaved by MMP14, thereby increasing migration of leukocytes (Chou et al., 2016).

Through the release of IL-1β, TNFα and other cytokines and growth factors by invading leukocytes, the expression of MMPs is increased. With the initial breakdown of cartilage, small fragments irritate the synovium and cause what is called secondary synovitis creating a positive feedback loop of inflammation (Burrage et al., 2006).

MMPs have been shown to cleave pro-TNFα, releasing it from the cell membrane and creating TNFα. This would suggest that MMPs in the synovium play a role in the instigation and maintenance of their own stimulation (Gearing et al., 1995; Mohammed et al., 2003); TNFα being one of the cytokines which leads to MMP upregulation.

Later in the inflammatory phase, cleaving of ligands CXCL2 and CXCL3 by MMP12 slows the migration of neutrophils usually attracted to them. This could serve as a mechanism to curtail the invasion of neutrophils and monocyte-derived macrophages (Chou et al., 2016).

Beyond these local articular effects during the inflammation phase, systemic effects across the body begin to take place. In *in vitro* studies as well as studies of other models, it has been found that Metalloproteinases generally have a wide variety of other cytokines and growth factors upon which they may act. These could have implications for the articular presentation RA directly but also could be responsible for systemic effects. Some of these molecules include alpha-defensin, syndecan-1, CXCL1, CX3CL1, L-Selectin, TGF-β, FGF and IGF in terms of proinflammatory effects, and MCPs 1-4 in the case of anti-inflammatory

effects (Mohammed et al., 2003).

2.4.2.2.2 Remodelling and Degradation

The ability of MMPs to act on the components of the ECM gives them the ability to change the structure and form of tissues as RA progresses. Upregulated by TNFα, IL-6, IL-17 and IL-1β, MMPs are produced by FLSs, excreted and activated by other MMPs (Shiozawa et al., 2011). They act on the components of cartilage, bone and fasciae (Burrage et al., 2006). Cartilage is made of collagen, predominantly type II collagen 45 - 50%, and proteoglycans, chiefly aggrecan, around 45%, with additional collagen types (VI, IX and XI) as well as other proteoglycans and macromolecules making up the remaining 5 - 10% (Murphy and Nagase, 2008; Parsons, 1998). To degrade it, collagen II must first be cleaved by an MMP without a hemopexin domain (MMP-1, 8, 13,) (Billinghurst et al., 1997; Klein and Bischoff, 2011) so its triple helical structure can be unwound and made available for other proteases (Klein and Bischoff, 2011). This also opens up the cartilage proteoglycans to attack by further MMPs and metalloproteases. Mechanical action of FLSs serves to further damage cartilage tissue following collagen degradation. After the destruction of type II collagen, it is replaced by type I collagen during healing (Burrage et al., 2006). These effects, taken together, cause a change of the form and characteristics of joint tissue, even to the point of cartilage depletion.

In contrast to cartilage, osteoclasts, derived from macrophages, are required to degrade bone. When binding to the bone, osteoclasts create a pocket called a lacuna into which MMPs 2, 9 and 13 as well as cathepsin K are secreted. The matrix that protects the bone, mostly made up of collagen I, is attacked by MMPs, breaking it down. This allows other metalloproteinases and cathepsin K to continue to degrade the remaining matrix. H^+ ions secreted by osteoclasts lead to bone demineralization and destruction (Rengel et al., 2007).

MMPs are also involved in neovascularization of inflamed tissue. Vascularization of the synovium and pannus regions perpetuates the inflammatory and destructive states and creates pathways for oxygen, leukocytes and signals to travel during subsequent flare events. During homeostasis, VEGF, a growth factor integral to inducing angiogenesis, creates a complex with CTGF, rendering it inactive. However, during inflammation and particularly in situations of hypoxia, MMPs can cleave the VEGF-CTGF complex, allowing for neovascularization. This occurs as pannus is formed during the degradation of cartilage. The invading cells, being poorly served with blood and already producing high amounts of MMPs, are able to stimulate the growth of new vessels through this mechanism, allowing invasion of cartilage and bone to continue and a large pannus to be served with oxygen and invading cells (Hashimoto et al., 2002; Kim et al., 2011).

In the inflammation and destruction phases, MMPs play a critical role in leukocyte migration, their own upregulation, neovascularization and the degradation of cartilage and bone. As integral actors, they are a promising target for non-invasive imaging in RA both in terms of diagnosis and monitoring.

2.4.2.3 Imaging strategies for MMP activity

A number of modalities have been used to image MMPs *in vivo*, including PET, SPECT, MRI and optical imaging (Scherer et al., 2008). Optical imaging probes can be small molecule ligands with high affinities for MMPs (Faust et al., 2008; Razavian et al., 2016). The other major form is the cleavable or activatable probes, consisting of a fluorophore and a quencher with an MMP cleavable peptide linker between them (McIntyre et al., 2004). In its original and inactive form, the fluorescent capability of the fluorophore is hampered by a proximity based Förster resonance energy transfer (FRET) interaction with the quencher, wherein the excitation energy is transferred and dissipated without photon emission. After cleavage of the linker by the appropriate MMP(s), the fluorophore is freed and can emit photons. Stated advantages include that there is a magnification effect as one MMP molecule can digest multiple probe molecules instead of a small molecule that can simply bind one MMP. Additionally, the background is lower because there is only local activation of the probe, however, this is disputed as activated probe can leak outside of the region in which it was produced, potentially reducing the signal to background ratio (Lee et al., 2010). In practice, the signal to background ratios are relatively similar, and the small molecules have the advantage of reaching their peak signal to background ratio on the order of 3 - 6 hours as opposed to 24 hours in the case of activatable probes (Waschkau et al., 2013).

In order to image MMPs, an MMP inhibitor ligand was developed and synthesized in our lab. The barbiturate based ligand, AF443 (Figure 9) binds irreversibly to activated MMPs and has a strong affinity for MMPs 2 and 9 (IC_{50} 27 ± 3 and 138 ± 19 nM respectively) (Faust et al., 2008). By modifying this ligand and attaching a fluorescent probe to it, AF443 can be visualized within an *in vivo* setting.

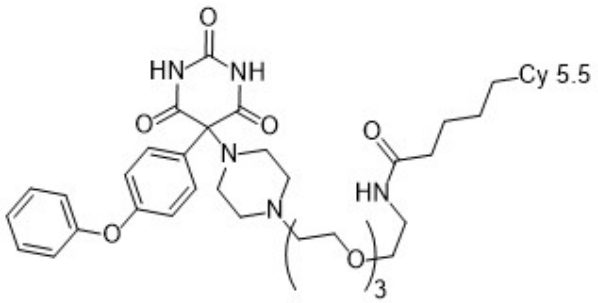

Figure 9: AF443-Cy5.5, MMP Tracer.

2.5 Animal Models of Rheumatoid Arthritis

To screen and validate new diagnosis and treatment methods as well as to carry out research into the underlying biological nature of RA, animal models are needed. No model fully

represents the disease due to its complex origins and redundant underlying pathways, so models are chosen based on the scientific question to be answered (Kollias et al., 2011). Numerous models of RA exist in rats, mice, guinea pigs, dogs and non-human primates. There are induced and, in rodents, spontaneous models.

Induced models typically couple an antigen with an adjuvant and call for the injection of the mixture intradermally, as a priming step to activate the immune system. Antigens used are model dependent and include: the yeast cell wall polysaccharide zymosan (Keystone et al., 1977), bacterial cell wall peptidoglycan (Koga et al., 1985), albumin from bovine serum or eggs (Brackertz et al., 1977), components of cartilage including proteoglycans (Finnegan et al., 1999), cartilage oligomeric matrix protein (Carlsén et al., 1998; Carlsen et al., 2008) or most famously type II collagen (Courtenay et al., 1980). These are usually mixed with Freund's Adjuvant to produce an enhanced immunological response. In the case of adjuvant arthritis and oil induced arthritis, the heat-killed mycobaterium in pure adjuvant (Pearson, 1956) or pristane oil (Wooley et al., 1989) can be administered and produce relapsing polyarthritis without additional components.

While many induced models exist, two stand out. The antigen-induced arthritis (AIA) model involves priming the animal with immunization of albumin (bovine or oval) and a subsequent intra-articular challenge. The model is invasive and requires the antigen to be injected directly into the synovium, an action difficult to achieve in mice. However, it has the advantage of inducing a predictable and local monoarthritis, which develops quickly. One can expect joint swelling around 1 day after injection and the highest levels of inflammatory activity on day 4 (Brand, 2005). The model has the advantage of localization and predictability but comes at the cost of not representing the polyarthritic nature of human RA.

The most used model, CIA, however, is polyarthritic and delocalized (Brand et al., 2007). It can be administered to mice, rats and non-human primates, allowing for assessment at several stages of drug discovery and validation (Kollias et al., 2011). Type II collagen is injected intradermally in the tail, where dendritic cells present the antigen using MHC class II, leading to helper T cell activation, secretion of IL-23 and B cell production of anti-type II collagen antibodies (Asquith et al., 2009). Usually a booster is used as a challenge, inducing the inflammatory phase of RA. Symptoms presented include synovial thickening and infiltration as well as cartilage and bone destruction (Bendele et al., 1999; Asquith et al., 2009). As explained earlier, this is the typical RA phenotype, and similar to human RA, it is highly variable in its presentation, complicating the experimental setup. The time of onset can be different within a cohort, different limbs can be affected to different extents, limbs within a mouse may develop arthritis at different times (Brand et al., 2007). The model's success is dependent upon the quality of the collagen used to prepare the model as well as the stress and environment the mice are exposed to (Kollias et al., 2011).

Spontaneous models are genetically modified or have developed spontaneous mutations that induce the spontaneous production of RA-like symptoms. These can be useful when studying the specific pathways that have been mutated and phenotypically reflect the human RA presentation i.e. spontaneous onset without external intervention coupled with

chronic recurring inflammatory episodes followed by remission. While these attributes are of considerable interest to the researchers targeting these particular pathways for diagnostics and therapy, they are not always suitable. The onset is less predictable than some induced models. Additionally, regulation steps upstream of the transgenically or mutationally altered protein will not be investigable using these models. Finally, Brand (2005) makes the case that it cannot be ruled out that human RA patients are primed and challenged with viral or bacterial material as a potential etiology for RA, thereby, hinting at a presumptuousness of stating induced models present in a similar fashion to human RA.

Mouse models provide researchers with a complex *in vivo* environment to improve understanding of the biology of RA triggering, inflammatory development and resolution. The induced CIA and AIA models and the spontaneous TNFα model, for example, have aided in the screening for, and production of, clinically used DMARDs and will continue to be used to explore future diagnoses and treatments (Hegen et al., 2008; Keffer et al., 1991).

3 Aim

Spatiotemporal patterns of molecular and cellular events underlie the initiation, progression and resolution of Rheumatoid Arthritis (RA); these patterns can potentially be used as biomarkers for diagnosis and monitoring of treatment efficacy. Molecular imaging can visualize such molecular and cellular events with the prospect of accurate diagnosis and personalized treatment. To achieve this, a combination of a comprehensive understanding of the biology underpinning the disease, targeting chemistry and imaging methodologies is required.

The aim of this thesis is the development of a translational strategy of molecular imaging of inflammatory activity in RA. We evaluated FRI to assess the potential of novel molecular imaging ligands targeting the inflammatory proteins S100A8/A9 and MMPs over time in an animal model of RA. We aimed to understand the expression pattern of both proteins as inflammation developed and resolved. The study was conducted with the hypothesis that they might be predictive of RA inflammatory flares. This investigation will serve as a step towards clinical translation of FRI imaging of biomarkers for RA patients.

4 Materials and Methods

4.1 Materials

4.1.1 Fluorescent labels

Cy5.5	Lumiprobe GmbH, Hannover, Germany
IRDye 800CW	LI-COR Biosciences, Lincoln, NE, USA

4.1.2 Chemicals

2-Propanol	Medite GmbH, Burgdorf, Germany
Antiperoxidase	DAKO (Agilent), Santa Clara, CA, USA
Bovine Collagen Type II	MD Biosciences, Oakdale, MN, USA
Citric Acid	Merck KGaA, Darmstadt, Germany
EDTA-Decalcification Solution 20 %	Morphisto GmbH, Frankfurt am Main, Germany
Entellan	Merck KGaA, Darmstadt, Germany
Eosin	Carl Roth GmbH + Co. KG, Karlsruhe, Germany
Fetal Calf Serum (FCS)	Gibco, Darmstadt, Germany
Haematoxylin	Medite GmbH, Burgdorf, Germany
Heat-killed Mycobacterium Tuberculosis (HKMT)	InvivoGen, San Diego, CA, USA
Incomplete Freund's Adjuvant	Sigma Aldrich, St. Louis, MO, USA
Isoflurane	AbbVie Deutschland GmbH, Ludwigshafen, Germany
Mac-3	BD Pharmingen Inc., San Diego, CA, USA
Paraffin	Medite GmbH, Burgdorf, Germany
Paraformaldehyde (PFA)	Carl Roth GmbH + Co. KG, Karlsruhe, Germany
PBS	Applichem GmbH, Darmstadt, Germany
Saline (0.9 % NaCl)	B. Braun Melsungen AG, Melsungen, Germany
Sodium hydroxide	Sigma Aldrich, St. Louis, MO, USA
Streptavidin	DAKO (Agilent), Santa Clara, CA, USA
Tris-NaCl-blocking (TNB) Buffer	PerkinElmer Life and Analytical Sciences, Shelton, CT, USA
Triton X 100	Carl Roth GmbH + Co. KG, Karlsruhe, Germany

Tyramide Signal Amplification System	PerkinElmer Life and Analytical Sciences, Shelton, CT, USA
Vectashield (DAPI)	Vector Laboratories Burlingame, CA, USA
Xylene (Isomers)	Carl Roth GmbH + Co. KG, Karlsruhe, Germany

4.1.3 Consumables

Altromin 1324 Standard Chow	Altromin Spezialfutter GmbH & Co. KG, Lage, Germany
Centrifuge Tubes (15 & 50 mL)	Corning Inc., Corning, NY, USA
Eppendorf tubes	Eppendorf, Hamburg, Germany
Insulin Syringe (Omnican F)	B. Braun Melsungen AG, Melsungen, Germany
Needle 20 G x 1.5 inch	Becton Dickinson S.A., Fraga, Spain
Syringe (1 mL) Luer-Lok Tip	Becton, Dickinson and Co., Franklin Lakes, NJ, USA

4.1.4 Antibodies

4.1.4.1 Primary Antibodies

Target	**Dist.**	**Ord. no.**	**Host**	**Reactivity**	**Dilution**	**Diluent**
IgG, N/A	Abcam	ab125938	rabbit	N/A	var.	4 % FCS, 0.5 % Triton-X in PBS
Mac-3	BD Phar.	550292	rat	mouse	1:50	4 % FCS, 0.5 % Triton-X in PBS
MMP-9	Abcam	ab3888I9	rabbit	mouse, human	1:200	4 % FCS, 0.5 % Triton-X in PBS
MRP14	Dr. Vogl	N/A	rabbit	mouse	1:1000	4 % FCS, 0.5 % Triton-X in PBS

4.1.4.2 Secondary Antibodies

Conjugate.	**Dist**	**Ord. no.**	**Host**	**Reactivity**	**Dilution**	**Diluent**
Alexa Fluor 488	life technologies	A11034	goat	rabbit	1:800	4 % FCS, 0.5 % Triton-X in PBS
Alexa Fluor 546	life technologies	A11010	goat	rabbit	1:1500	4 % FCS, 0.5 % Triton-X in PBS
Alexa Fluor 555	life technologies	A21430	goat	rabbit	1:1000	4 % FCS, 0.5 % Triton-X in PBS
Biotin	BD Phar.	550325	mouse	rat	1:500	1 % BSA

4.1.5 Equipment

In-Vivo MS FXPro	Bruker BioSpin GmbH, Rheinstetten, Germany
Landmark Anaesthesia System	Vetland L.L.C. Louisville, KY, USA

Microscope Nikon ECLIPSE Ni	Nikon, Chiyoda, Japan
Microtome RM2235	Leica, Solms, Germany

4.1.6 Software

Bruker MI 7.2	Bruker BioSpin GmbH, Rheinstetten, Germany
GraphPad Prism 7	GraphPad Software, La Jolla, CA, USA
Matlab	The Mathworks Inc., Natick, MA, USA
MEDgical	In-house Tool (EIMI), Münster, Germany
Python	Python Software Foundation, DE, USA

4.2 Methods

4.2.1 Mice

DBA/jdba1/j mice, male, aged 10 – 12 weeks, purchased from Janvier (Le Genest-Saint-Isle, France) were included in this study. Mice were group housed in semi-sterile cages with filter tops during the experiment. They had access *ad libitum* to water and Altromin 1324 standard chow. A regular light/dark cycle as well as constant temperature of 23° C and constant relative humidity of 40 % were maintained during housing. All applicable institutional and national guidelines for the care and use of animals were followed. All mouse experiments were approved by the State Review Board of North Rhine-Westphalia (Germany) under the license 84-02.04.2012.A058 and conducted according to the German Law regarding the Care and Use of Laboratory Animals.

4.2.2 Collagen-induced arthritis (CIA)

In order to ensure the ethical treatment of animals, the onset and resolution phases were investigated independently allowing for intensive serial imaging during each phase and the longitudinal monitoring of the disease course of the model without causing undue stress on individual animals. CIA was induced in DBA/jdba1/j mice as previously described (Vogl et al., 2014). Mice were immunized by intradermal injection of bovine collagen type II (bCII) at a concentration of 2 mg/mL emulsified in Complete Freund's Adjuvant (Incomplete Freund's Adjuvant containing HKMT at a concentration of 4 mg/ml), in the tail base using a Luer-Lok Tip 1 mL syringe fitted with a 20 G x 1.5 inch needle under 1.5 % isoflurane anaesthesia. 21 days later, 100 µg bCII emulsified in Incomplete Freund's Adjuvant was administered i.p. as a boost injection. Mice were controlled and scored at least 3 times a week for clinical symptoms of arthritis. Each paw was scored according a 3 point scoring system, resulting in a maximum total clinical score of 12 for each mouse. Score 0 = no swelling, score 1: mild swelling affecting entire paw or only one joint; score 2: distinct swelling affecting 2 joints; score 3: severe swelling affecting several joints or ankylosis. Naïve, control mice

were handled and scored in a similar manner to the CIA mice. All mice were scored by an experienced investigator, blinded to the experimental group (CIA, controls).

4.2.3 FRI Imaging

FRI was performed using the In-Vivo MS FXPro composed of a 400 W illumination lamp and filter settings for Cy 5.5 (excitation 625 ± 10.0 nm, emission 700 ± 17.5 nm, exposure 5 s) and IRDye 800CW (excitation 720 ± 10.0 nm, emission 790 ± 20.0 nm, exposure 10 s), a 10x lens, and a cooled CCD with 4x106 pixels. A Binning of 1, f-stop of 2.50 and field of view of 120 mm were used. For image analysis, co-registered white light and X-ray images were taken. Animals were measured at baseline and then injected intravenously (i.v.) with both S100A9-specific IRDye 800CW-CES271 (Faust et al., 2015) and the broad spectrum MMP tracer Cy5.5-AF443 (Faust et al., 2008) at 2 nmol per tracer simultaneously in 100 µL of saline. All imaging and injections were conducted under inhaled anaesthesia (2.5 % isoflurane in 100 % O_2).

4.2.4 Imaging Analysis

Using the Bruker MI 7.2 software, regions of interest (ROIs) were defined around each paw (P_x) as well as the snout/mouth region (BG_M), which served as an intrinsic background as it is not covered in fur and is well vascularized, thereby providing an approximation of tracer in blood. Finally, a system background ROI (BG_S) in a blank region on the stage, to the right of the mouse was defined (see Figure 10). The signal intensities were processed with the following formula.

$$\frac{P_x - BG_S}{BG_M - BG_S} \tag{1}$$

This yields a signal to background ratio (SBR). These intensities were graphed over time and correlated using GraphPad Prism 7.

In order to compute the Thresholded Area and Fraction methods, images and ROIs were transferred to MEDgical, an in-house, molecular imaging, image analysis software. Using a Matlab script embedded in MEDgical, the entire image was recomputed so as to convert pixels to SBRs. This was followed by masking of ROIs and images were converted to comma seperated value (CSV) files for export by Matlab. A custom built Python program imported the CSVs and computed the areas and fractions of pixels exceeding the threshold before collating the information for analysis and visualization.

4.2.5 Immunohistochemistry

After sacrifice, paws were explanted and fixed in 4 % PFA . Decalcification took place over 4 weeks in 20 % EDTA. The paws were dehydrated and embedded in Paraffin for slicing.

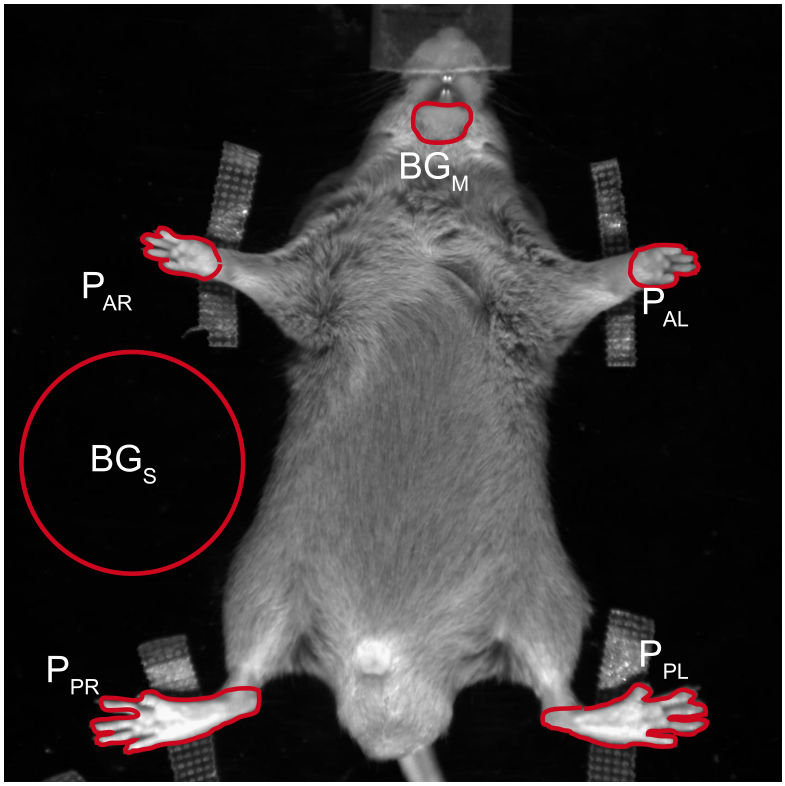

Figure 10: Image analysis Regions of Interest (ROI). Depicted as they were drawn for analysis. Paws (P_x), Mouth Background (BG_M), System Background (BG_S) are pictured.

4.2.5.1 H&E staining

Slices were incubated for 10 min in Haematoxylin before being rinsed for 10 min under running tap water. Slices were further stained with Eosin for 7 min and rinsed with distilled water for 5 min. Slices were dehydrated stepwise using baths of 50, 70, 80, 96 and 100 % 2-Propanol for 5 min each and finally Xylene for 10 min before being embedded in Entellan.

4.2.5.2 Immunofluorescence Staining

Neighboring slices were taken for fluorescence preparations. Slices were deparafinnized by heating for 60 min at 60° C and washing twice with a bath of Xylene. To rehydrate the slices, they were bathed stepwise in 100, 96, 80, and 70 % 2-Propanol for 5 min each. Slices were washed in distilled water twice for 5 min and twice in PBS for 5 min. Citrate buffer (pH 6) was used for demasking, whereby the slices were steamed for 20 min before being allowed to cool at 23° C for 20 min and washed with distilled water for 5 min followed by PBS for 5 min. Slices were incubated overnight with the primary antibody at 4° C in a dark chamber. The following morning they were washed 3 times with PBS for 5 min. The secondary antibody was added to the slices and incubated for 60 min at 23° C. Slices were washed 3 times with PBS for 5 min. The DAPI containing mounting medium Vectashield was used as a counter-staining for all fluorescence preparations. Thereafter images were acquired using a fluorescence/light

microscope.

The primary antibody for MMP-9 staining was polyclonal rabbit-anti-mouse MMP-9 with a secondary antibody of goat-anti-rabbit labelled with Alexa Fluor 488 (green). The primary antibody for S100A9 staining was polyclonal rabbit-anti-mouse MRP14 (S100A9) with a secondary antibody of goat-anti-rabbit labelled with Alexa Fluor 555 (red).

Control stainings were made to ensure the validity of the method and were conducted in the same manner as above. Rabbit IgG was added as a non-specific primary antibody at the same dilution as the antibody it was to mimic, with the secondary, fluorescent antibodies being added to visualize staining. These were successful, showing minimal staining.

4.2.5.3 Mac-3 / MRP14 Double Staining Immunofluorescence

Neighboring slices were handled as stated in the immunofluorescence Section 4.2.5.2 above until demasking. They were demasked by steaming for 30 min, using the same Citrate Buffer (pH 6) and allowed to cool at 23° C for 20 min before being washed twice in distilled water for 5 min and twice in PBS for 5 min. Slices were bathed in Antiperoxidase for 10 min to block before being rinsed 3 times for 5 min in PBS. Slices were bathed in TNB buffer for 30 min to block. Mac-3 rat-anti-mouse antibody was added and incubated overnight at 4° C. The following day slices were rinsed 3 times for 5 min in PBS. The biotinylated secondary antibody was added and incubated at 23° C for 45 min. Thereafter, slices were rinsed 3 times for 5 min in PBS. Streptavidin was added and incubated for 30 min before slices were rinsed 3 times for 5 min in PBS. The fluorophore Tyramide Signal Amplification System's amplification reagent was added and incubated for 7 min. Three PBS rinses of 5 min each were performed. The MRP14 rabbit-anti-mouse antibody was added and incubated at 23° C for 1 hour. Thereafter, slices were rinsed 3 times for 5 min in PBS. The Alexa Fluor 546 goat-anti-rabbit antibody was added and incubated for 25 min. Three PBS rinses of 5 min each were performed. The DAPI containing mounting medium Vectashield was used as a counter-staining for all fluorescence preparations. Thereafter images were acquired using a fluorescence/light microscope.

4.2.6 Statistical Analysis

Data were expressed either as mean of a group or in a paw-wise manner. Non-parametric ANOVAs were performed on the onset series where the D'Agostino and Pearson normality test failed, otherwise a parametric ANOVA was used. In the resolution phase t-tests, both parametric and non-parametric, were employed. Correlations of S100A9 and MMP SBRs were performed using Pearson's correlations. The relationship between the SBRs of different clinical scores were assessed using non-parametric ANOVAs due to the failure of the D'Agostino and Pearson normality test. The threshold for significance was set at $p < 0.05$ and all tests were performed using Graphpad Prism 7. Data are described and depicted showing the mean with error bars representing the standard deviation.

4.2.7 Experimental Setup

4.2.7.1 Onset group

7 male, DBA/jdba1/j mice (5 CIA, 2 control) were induced as explained above. FRI was performed after the initial challenge, before boosting, at the day of boost and one day post boost. Thereafter, imaging was conducted every 3 days until day 13 (see Figure 11A). After 10 days, a cohort of 3 CIA mice had reached a level of inflammation where they were required to be sacrificed. Another cohort of 2 CIA mice had considerable inflammation at day 13 and were sacrificed. Due to the observed differences in response to boosting, the CIA mice were separated into fast and slow responder groups.

4.2.7.2 Resolution group

10 male, DBA/jdba1/j mice (6 CIA, 4 control) were induced and scored as mentioned. FRI was performed 8 days after boosting, with regular imaging occurring twice a week at an alternating interval of 3 and 4 days for a period of 5 weeks after the first imaging session, at which point the animals were sacrificed (see Figure 11B).

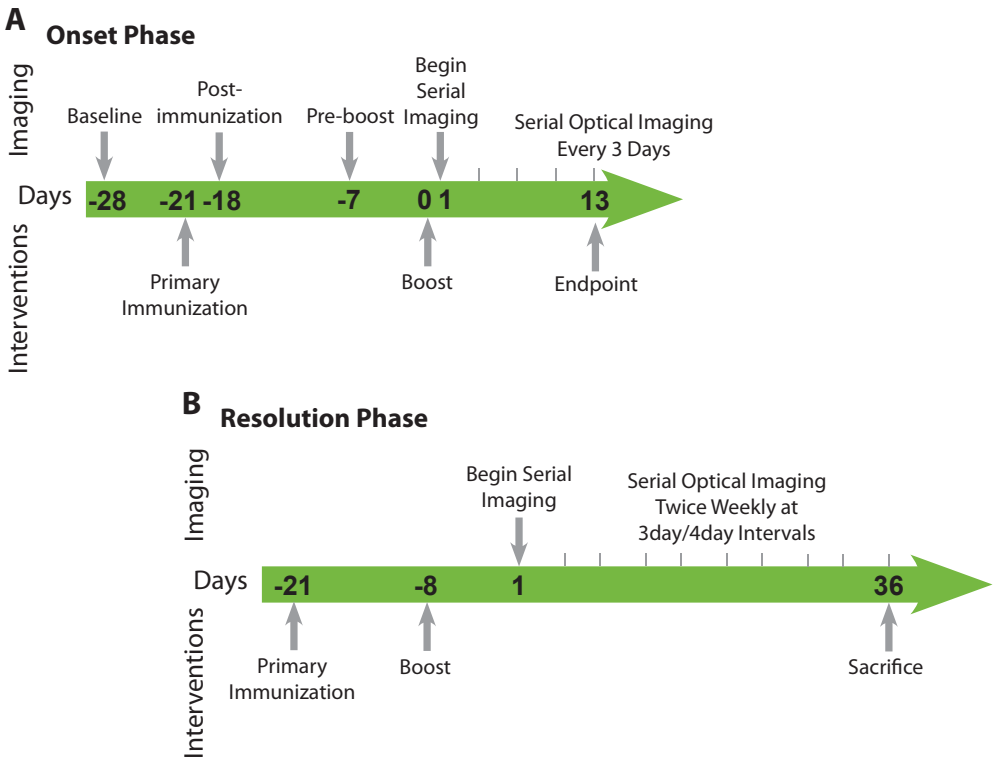

Figure 11: Experimental setup. (A) Onset phase and (B) resolution phase intervention and imaging timelines.

5 Results

By using FRI, we were able to successfully track the onset and resolution phases of inflammation in the CIA model longitudinally by non-invasive imaging of two biomarkers of inflammation, S100A8/A9 and activated MMPs. In order to investigate the biomarkers over the life-cycle of inflammation, it was necessary to divide the experiment into an onset and resolution phase. Although non-invasive imaging enables repeated measurements of an individual mouse, the intervals between imaging sessions and the overall number of imaging

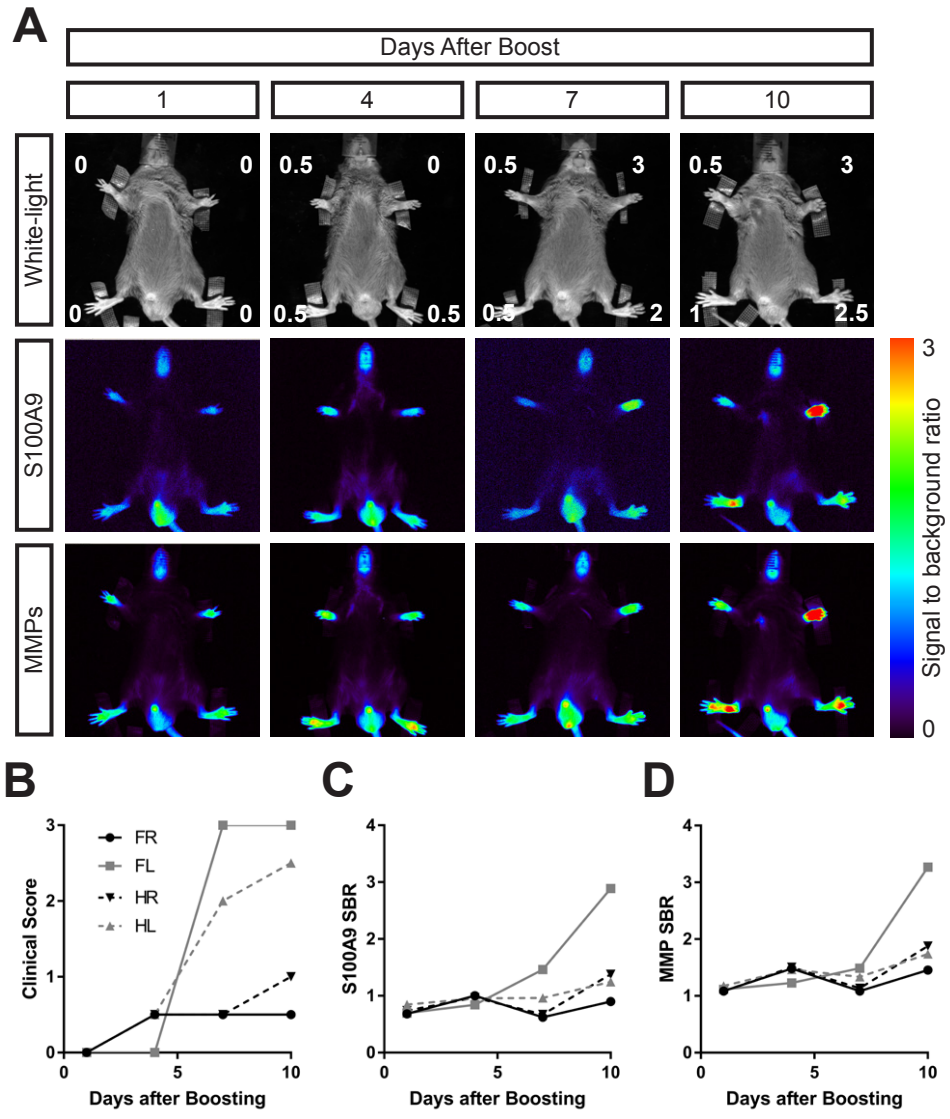

Figure 12: Onset phase longitudinal imaging. *A* Representative images, in a single mouse, of the inflammatory process in the CIA model from days 1 to 10 after boost. Paw-wise clinical scores on white-light images (top row) and accompanying FRI images depicting S100A9 (middle row) and MMP (bottom row) signal to background ratios (SBRs) as they increased until the animal was sacrificed on day 10.*B* Paw-wise clinical scores. *C* Paw-wise S100A9 SBRs. *D* Paw-wise MMP SBRs.

sessions are limited due to the stress they put on the animals. In addition, stress has been shown to affect the CIA model in rats, either causing a decrease in or an exacerbation of symptoms (Rogers et al., 1979, 1983).

5.1 Onset phase

In the onset phase, FRI was performed at baseline, after the initial challenge, before boosting, and one day after boosting. Thereafter, imaging was conducted every 3 days until a maximum of day 13, as depicted in Figure 11A. A subgroup of animals were sacrificed at day 10, having reached the criteria for sacrifice under animal ethics guidelines.

5.1.1 Imaging results show individual inflammation of paws in CIA

The mice who developed arthritis did so in a heterogeneous manner with each paw having it's own development and peak clinical score. A representative example of clinical score and imaging results in the onset phase is shown in Figure 12A. As expected, clinical scores in all paws remained low during the first 4 days after boosting as the model requires some time for inflammatory response (Figure 12B). The low clinical scores are matched by a minimal signal increase in S100A8/A9 or MMP imaging (Figure 12C, D). Days 7 and 10 show a heterogeneous response in clinical scores between different paws in the same mouse, ranging from 0.5 to 3. This shows that the paws, although systemically tied to one another, can be taken relatively independently for the purpose of analysis.

Close analysis of the S100A9 and MMP signals shows that they are qualitatively and quantitatively similar. However, the response of MMP SBRs appears to be higher in general and displays areas of intensity that are less apparent using the S100A9 tracer.

5.1.2 Two subtypes of disease progression identified

Figure 13A shows the average clinical scores in the onset phase in both CIA and control animals. Interestingly, we were able to identify two separate groups within the CIA animals: a fast responding group (mouse n = 3, paw n = 12) and a slow responding group (mouse n = 2, paw n = 8), which showed homogeneous response to the boost within their groups. The fast responders had high total clinical scores already by day 10 and it was deemed that they should be sacrificed on the grounds of animal ethics, thereby reducing the total number of paws in further measurements. The slow responders continued to develop nflammation over the following 3 days until 13 when they were sacrificed and were significantly different to controls at that time point. Therefore, due to the sacrifice cut-off criteria and faster development of symptoms, we felt it was reasonable to treat these mice as two separate subtypes.

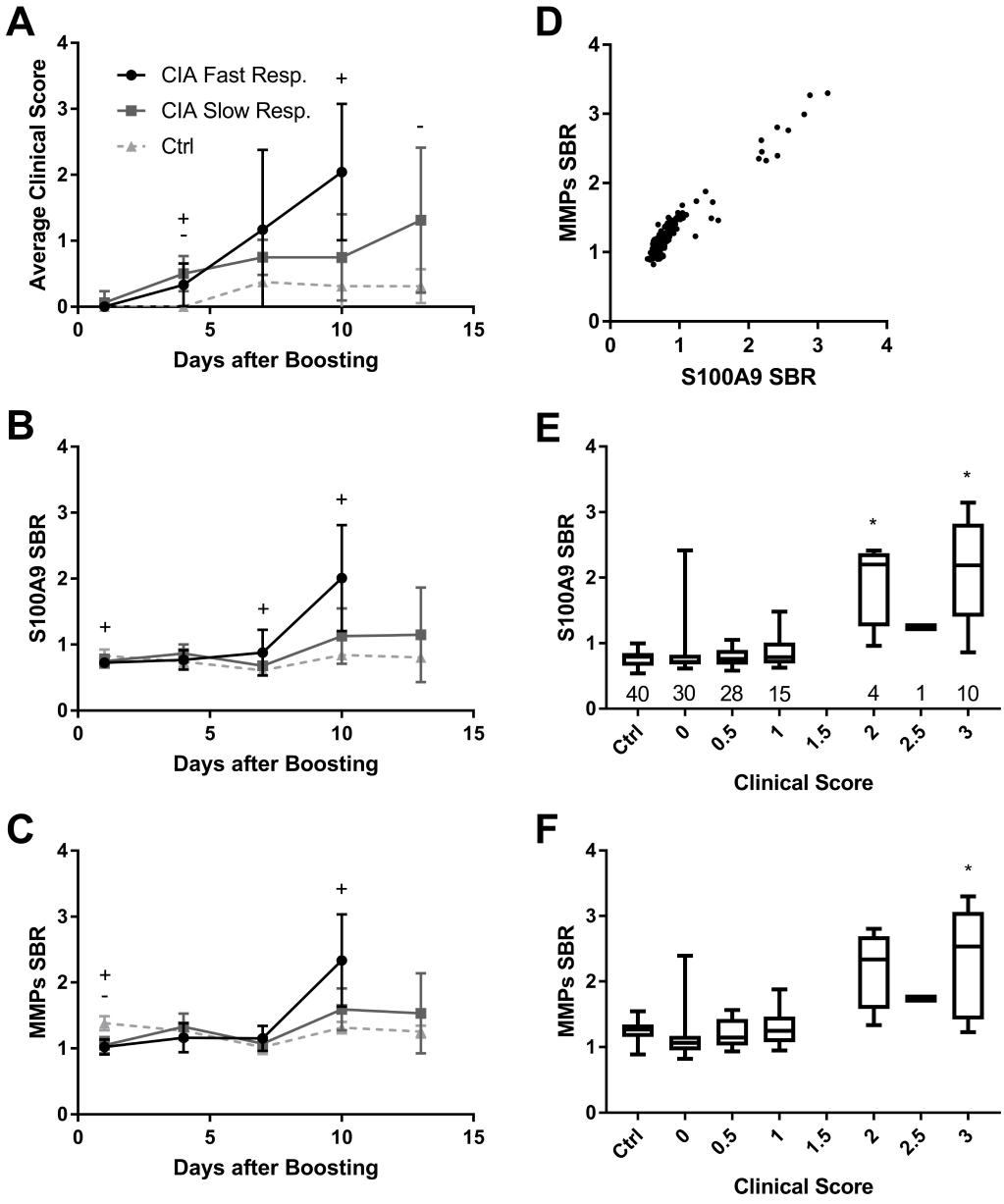

Figure 13: S100A8/A9 and MMP signal in the onset phase. (A) Average clinical scores of animals in the onset phase sorted into three groups, fast responders (n=3), slow responders (n=2) and control animals (n=2). (B) S100A9 signal to background ratios (SBRs) of animals in the onset phase. (C) MMP SBRs of animals in the onset phase. Time points showing significant differences using a nonparametric (Kruskal-Wallis) ANOVA on days 1-10 and a Mann-Whitney t-test on day 13 with significance in both cases denoted at $p < 0.05$. Between CIA high responders and controls significance is denoted with a +, CIA low responders and controls with a –. (D) Correlation of S100A9 to MMP SBRs on a per paw basis tested using the Pearson correlation coefficient. Box and whisker plots of the (E) S100A9 and (F) MMPs signal to background ratios of paws having been assessed to have a particular clinical score tested with a 1-way ANOVA. Clinical scores showing significance ($p < 0.05$) when compared with controls and clinical score of 0 and 0.5 are denoted with an *. The number of paws having each clinical score is written in the respective columns.

5.1.3 Both fast and slow responders show statistically elevated S100A8/A9 and MMP levels on the day of peak inflammation

Both S100A8/A9 and MMP SBRs roughly followed the clinical score during the onset of CIA (Figure 13A-C). The fast responding group exhibited statistically higher S100A8/A9 and MMP SBRs on day 10, the day of peak inflammation, as compared to control mice. Fast responders also showed statistically elevated S100A8/A9 SBRs at day 7. On day 1, S100A8/A9 SBRs of control mice were elevated above the averages of those for the fast responding group and MMP SBRs were higher than those in control mice for both the fast and slow responding groups.

5.1.4 S100A8/A9 and MMP SBRs correlate and are elevated in paws with high clinical scores

S100A8/A9 and MMP SBRs correlated strongly (Pearson's Correlation $r = 0.9617$, $p<0.0001$. Figure 13D), however, there is a trend towards the MMPs producing a higher SBR than S100A9 in the same paw. This could indicate higher expression of activated MMPs or increased sensitivity of the MMP tracer within this model as compared to the S100A8/A9 expression.

Paws with clinical scores of 2 and 3 in the onset phase had significantly higher S100A8/A9 SBRs than control paws as well as paws with clinical scores 0 and 0.5 (Figure 13E). Paws with clinical score 3 showed significantly higher MMP SBRs when compared to controls and clinical scores of 0 and 0.5 (Figure 13F). There were not enough instances in which a paw reached a clinical score of 2.5 in the onset phase to make a determination of significance.

5.2 Resolution phase

In the resolution phase, serial FRI imaging began 8 days after boosting at alternating intervals of 3 and 4 days. These twice weekly imaging sessions continued until day 36 as depicted in Figure 11B. Mice which died spontaneously or were sacrificed due to disease severity reduced the number of paws over time.

5.2.1 Imaging results show inflammation resolution and low SBRs at late time point regardless of paw clenching

The beginning of the resolution phase was characterized by high signals in FRI as the mice reached peak inflammatory response. Clinical scores and FRI signals were heterogeneous between paws in single mice and between mice. The longitudinal monitoring of S100A8/A9 and MMP SBRs in an example mouse during the resolution phase is pictured in Figure 14A. It can be observed that the mouse began with high clinical scores, which gradually reduced over the time course.

To depict one special example, the front left paw which drops from a clinical score of 3 to a clinical score of 1.5 on day 22 before returning to a clinical score of 3 on day 36 (Figure

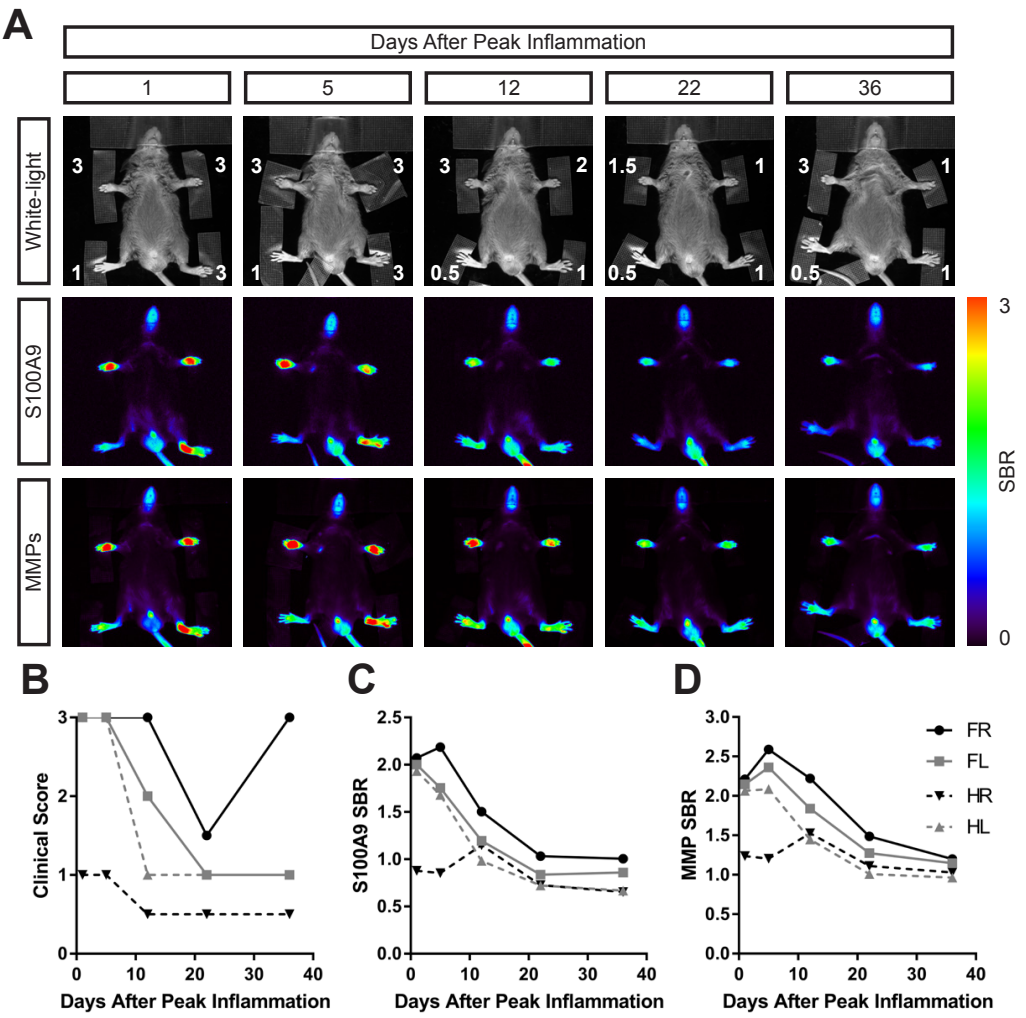

Figure 14: Resolution phase longitudinal imaging. *A* Representative images, in a single mouse from days 1 to 36. Paw-wise clinical scores on white-light images (top row) and accompanying fluorescence reflectance images depicting S100A9 (middle row) and MMP (bottom row) signal to background ratios (SBRs) as they decreased. *B* Paw-wise clinical scores. *C* Paw-wise S100A9 SBRs. *D* Paw-wise MMP SBRs.

14B). This is a paw exhibiting clenching due to remodeling of the tissue and so while the S100A8/A9 and MMP signals remain relatively low in the paw at day 36, the deformation obliges a clinical score of 3. As in the onset phase, one can observe that the SBRs for S100A8/A9 and MMPs are similar and the MMP SBRs appear to be higher than those of S100A8/A9 (Figure 14C, D).

5.2.2 Imaging of the resolution of a highly inflamed state shows decreasing levels of inflammatory biomarkers.

Resolution phase clinical scores of CIA mice begin high at an average of nearly 2, increasing from day 1 to day 5 before falling, thereafter steadily declining until day 29 (Figure 15A).

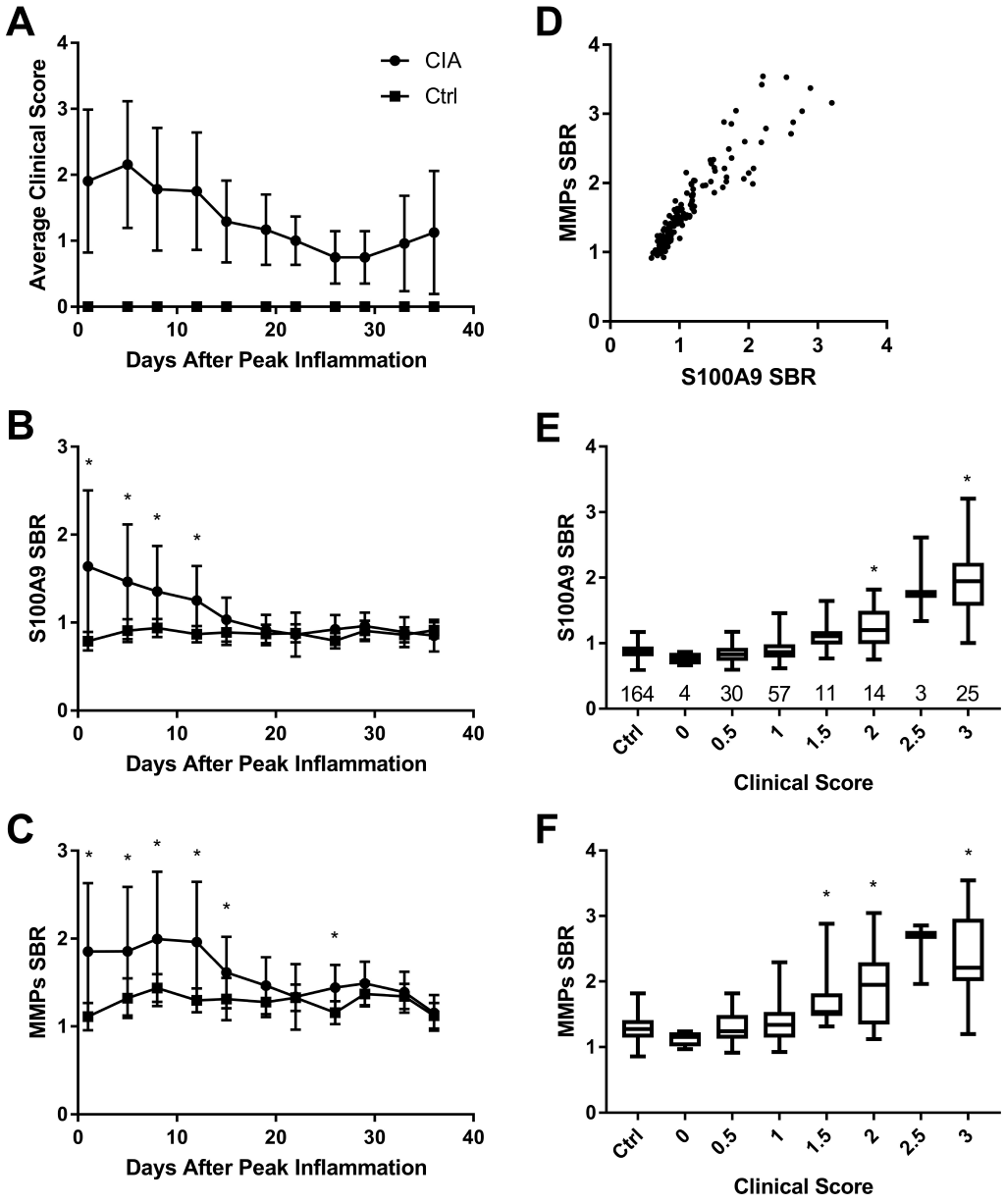

Figure 15: S100A8/A9 and MMP signal in the resolution phase. (A) Average clinical scores of animals in the resolution phase, sorted into CIA (n=4) and control (n=4) groups. All time points showed significant differences ($p < 0.05$) between the CIA animals and the hypothetical value (0) using the Wilcoxson signed-rank test. At all time points the controls were not significant using the same test and hypothetical value. (B) S100A9 signal to background ratios (SBRs) of the resolution phase were tested at each time point using a non-parametric Mann-Whitney t-test as one time point did not pass the D'Agostino & Pearson normality test. (C) MMP SBRs of the resolution phase were tested at each time point with a parametric t-test. Significant differences ($p < 0.05$) are denoted with an *. Correlation of S100A9 to MMP SBRs on a per paw basis (D) tested using the Pearson correlation coefficient. Box and whisker plots of the S100A9 (E) and MMPs (F) signal to background ratios of paws having been assessed to have a particular clinical score tested with a non-parametric (Kruskal-Wallis) ANOVA (Tables of multiple comparisons in Supplemental Table 1). Clinical scores showing significance ($p < 0.05$) when compared with controls and clinical score of 0 and 0.5 are denoted with an *. The number of paws having each clinical score is written in the respective columns.

Clinical scores of CIA mice did not reach the level of control mice and were significantly higher than controls at all time points.

Following day 29, paw clenching was observed in some mice and caused a renewed increase in the average clinical score until termination of the experiment. However, this was due to a criteria for paw clenching in the scoring rubric designed for acute, rather than resolved, inflammation and is not necessarily indicative of an inflammatory process itself. The phenomenon will be examined more closely in Section 5.3 on histology.

Image analysis showed that SBRs of S100A8/A9 and MMPs gradually decline over time in a manner similar to the clinical score (Figure 15B, C). S100A8/A9 and MMPs showed significantly higher SBRs for the CIA group as compared to controls until days 12 and 15 respectively. While quite similar to one another, S100A8/A9 shows a more rapid decline after peak inflammation, whereas MMPs seem to plateau for the first 12 days before decreasing to the level of controls. On day 26, after the resolution of inflammation and on a day of low clinical scores, MMP SBRs were elevated for a single imaging day, exhibiting a significant difference when compared with controls.

As in the onset phase, the resolution phase S100A8/A9 and MMP SBRs correlate very well with each other (Pearson's Correlation $r = 0.9231$, $p < 0.0001$. Figure 15D). In both the onset and resolution phase, the MMP tracer produced higher SBRs. Spreading of points can be observed at high SBRs in the resolution phase.

Clinical scores of 2 and 3 show significantly higher S100A8/A9 SBRs as compared to controls and clinical scores of 1 and below (Figure 15E). MMP clinical scores of 1.5, 2 and 3 show significantly higher SBRs than the control treatment as well as clinical scores of 0 and 0.5 in the resolution phase (Figure 15F).

No significant difference was found between the clinical scores of 3 between the onset and resolution phases in either S100A8/A9 or MMP signal to background ratios. This suggests that the experimental design and the behavior of the model is sound; the model develops to a similar, highly inflamed, state before resolving; the point at which the onset series ends and the resolution series begins is statistically the same.

5.3 Histology

In order to validate the imaging data and qualitatively assess the availability of target to bind the imaging ligands, histology was performed. Figure 16 shows a comparison of imaging data with both morphological H&E staining and immunohistochemistry targeting S100A9 and MMPs.

5.3.1 Morphological findings

Histological analysis (Figure 16) showed minor synovial thickening and edema at clinical score 1 when compared with control slices. Large changes in overall morphology, including synovial thickening, edema and infiltration by inflammatory cells, were observed in H&E staining in

paws of clinical score 2 and 3. Clinical score 3 shows marked swelling and deformation of the tissue, conducive with edema, which accompanies high levels of inflammation.

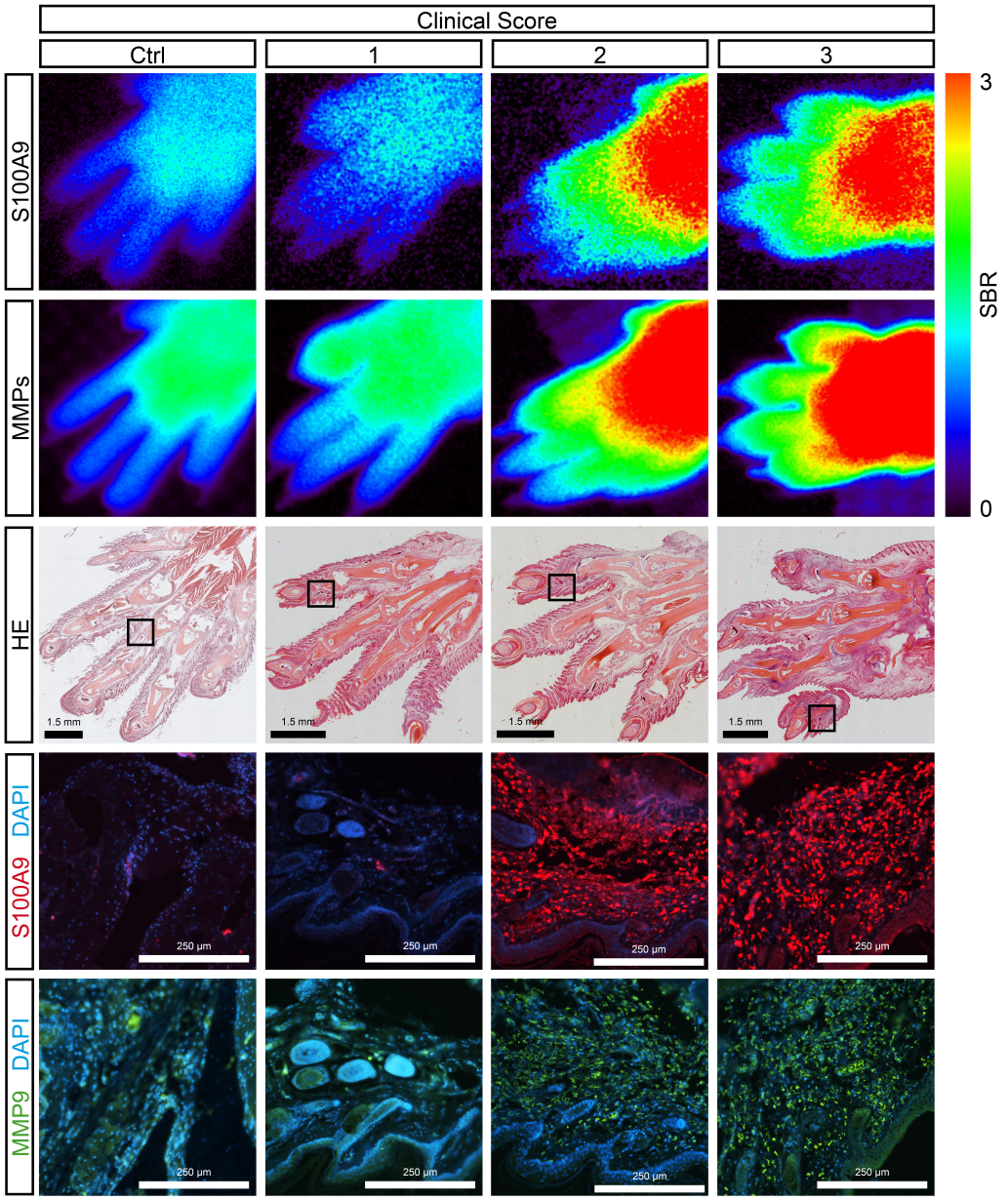

Figure 16: Imaging and histological corroboration of target presence. Imaging examples of signal to background ratios (SBR) (S100A9, top row; MMPs, 2nd row), matching histology (H&E, 3rd row) and immunohistochemistry (S100A9, MMPs, 4th and 5th row) for different clinical score grades. Histology was performed on neighbouring slices and the magnified images depict areas indicated by the black boxes on each H&E slice. S100A9 and MMP SBRs are low in control and clinical score 1 images when compared with clinical scores 2 and 3. The progressive deformation from the control paw to clinical score 3 is visible in the H&E stainings. Synovial thickening, edema and joint destruction are visible in clinical scores 2 and 3. Corroborating the imaging data, the S100A9 and MMP-9 stainings show elevated levels of each protein at clinical scores 2 and 3 in comparison to the relatively low expression levels in control and clinical score 1 histological slices.

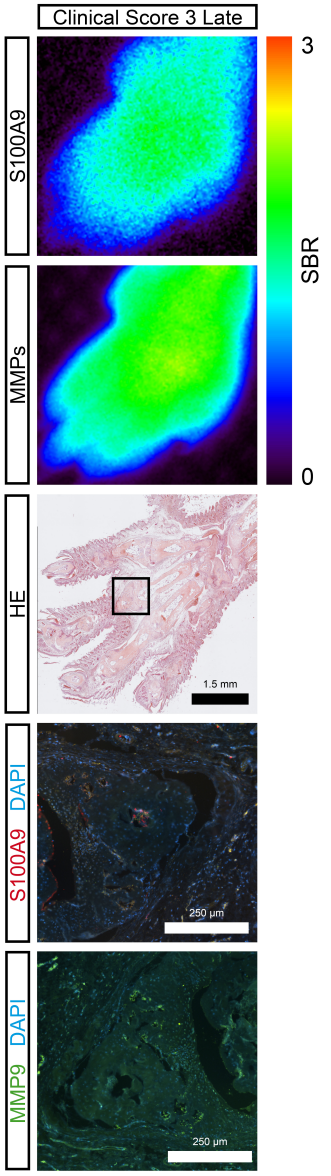

Figure 17: Resolved inflammation and deformation Histology and matching imaging data from a paw with clinical score 3 (sacrificed at day 36), after resolution of inflammation (clinical score 3 late). H&E staining along with S100A9, and MMP-9 stainings are shown. In the H&E staining, bone lesions are evident. Bone thickening, particularly in the joints is apparent and there is even evidence of fusion. The synovium is either very swollen or destroyed. S100A9 levels are low with small pockets seen at bone margins in holes in the bone. MMP levels are also low and show expression at these same bone margins.

5.3.2 Immunohistochemistry corroborates target presence beginning at clinical score 2

From the corresponding FRI images it is clear that levels of MMPs and S100A9 are elevated beginning at clinical score 2. The increased expression was corroborated by immunohistochemistry for MRP14 (S100A9) and MMP-9 (representative for MMPs), showing high levels only at clinical scores 2 and 3.

5.3.3 Late stage disease shows little S100A8/A9 and MMP expression despite high clinical scores

As stated earlier, following the return of S100A8/A9 and MMP SBRs to control levels and the clinical score to a low level, just above controls, the clinical score rose again after day 29. This occurred due to a scoring criteria for clenching of the paws.
Despite the high clinical score observed externally and the major remodeling of paws as well as the apparent joint destruction visible in the histology of paws taken at day 36, neither the imaging nor the immunohistochemistry data indicated high levels of either S100A9 or MMPs during this very late stage of the resolution phase (Figure 17).

5.3.4 Single joint inflammation case study

In an incidental finding, we were able to visualize local inflammation down to a single joint as shown in Figure 18. Using FRI this phenomena was only visible in the MMP channel. However, immunofluorescent histological staining showed upregulation of MMPs and S100A9 in the distal affected joint. The X-ray image also shows minor bone damage indicating the beginnings of bone resorption which occurs at the early stages of Rheumatoid Arthritis. This is not a common phenomenon but shows the promise of developing the method further.

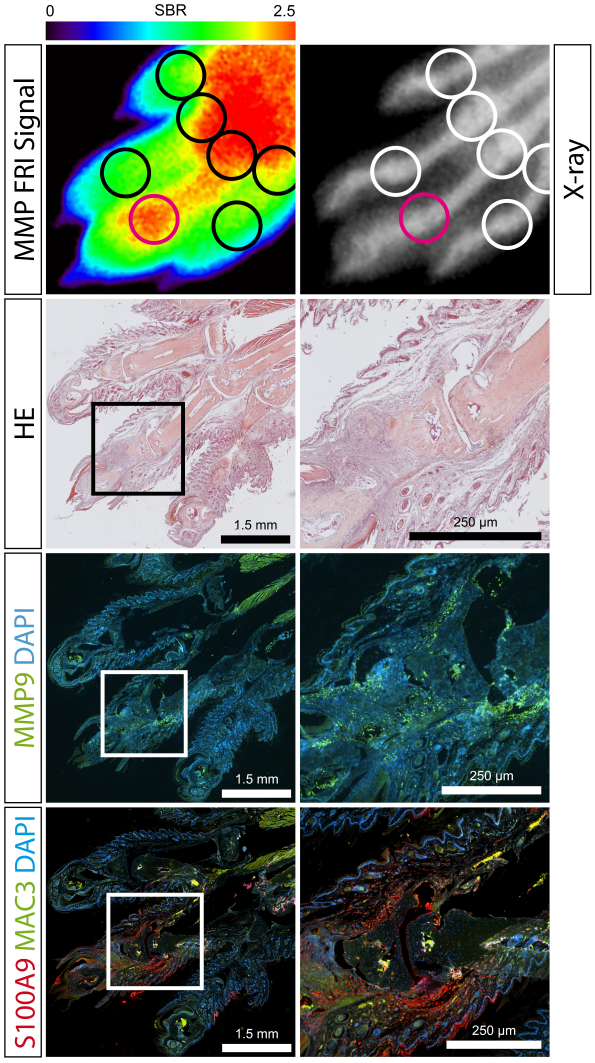

Figure 18: Single joint case study. A case study of a mouse paw that had a clinical score of 1 at sacrifice. However, imaging was able to pick up low level inflammation at the joint level using the MMP tracer Cy5.5-AF443. The inflammation was verified through immunohistochemistry of S100A9 and MMP-9 as well as structural changes in H&E staining. The accompanying X-ray is also shown. Magnified sections are denoted with black or white boxes. Circles in the FRI and X-ray data highlight single joints and with the pink joint being that which is depicted in the immunohistochemistry slices.

5.4 Analysis Methods

5.4.1 Why employ the signal to background ratio?

Several analysis methods were considered and evaluated before before arriving at the optimal, whole paw method used above. The most naïve approach would have been to analyze the raw photon counts of the paws. This, however, did not factor in small variations in the amount of tracer injected nor did it take into account the fact that with short time intervals between imaging days, there can be some residual tracer in the mouse's blood stream. This was particularly important in the resolution phase analysis where the imaging days were irregularly spaced in an alternating 3 day, 4 day configuration. Figure 19A shows the average raw signal recorded during baseline measurements before injection of the day's imaging tracer. An initial increase is observed, followed by a saturation from day 8 to 36, where the average radiant efficiency holds at an average of 851 $[p/s/cm^2/sr]/[\mu W/cm^2]$. A similar trend was observed for S100A9 (not pictured) with the mean average radiant efficiency from day 8 to 36 being 227 $[p/s/cm^2/sr]/[\mu W/cm^2]$.

An additional effect was discovered, whereby the muscle background of control mice in both tracers was consistently elevated when compared with CIA mice (see Figure 19B). Initially, this did not match expectation. However, with further consideration of the small amount of tracer injected (2 nmol), and the fact that CIA is a systemic model of disease, came a hypothesis that the tracer was also binding to targets not seen in the FRI images.

Using positron emission tomography (PET) scans of Fludeoxyglucose (FDG), a radioactively labelled glucose analogue, which is injected and is taken up in areas of high metabolism, one can image areas of inflammation. Figure 20 is an FDG-PET image of a CIA mouse with pronounced inflammation of the paws. In addition to the paws, whose signal can be captured using FRI, FDG-PET is able to visualize areas of inflammation covered by the animal's fur that would be invisible to FRI. Areas of potential inflammatory activity, which are likely to bind the S100A8/A9 and MMP tracers are marked by boxes. The area near the base of the tail where the immunization takes place is inflamed as well as other knee and elbow joints.

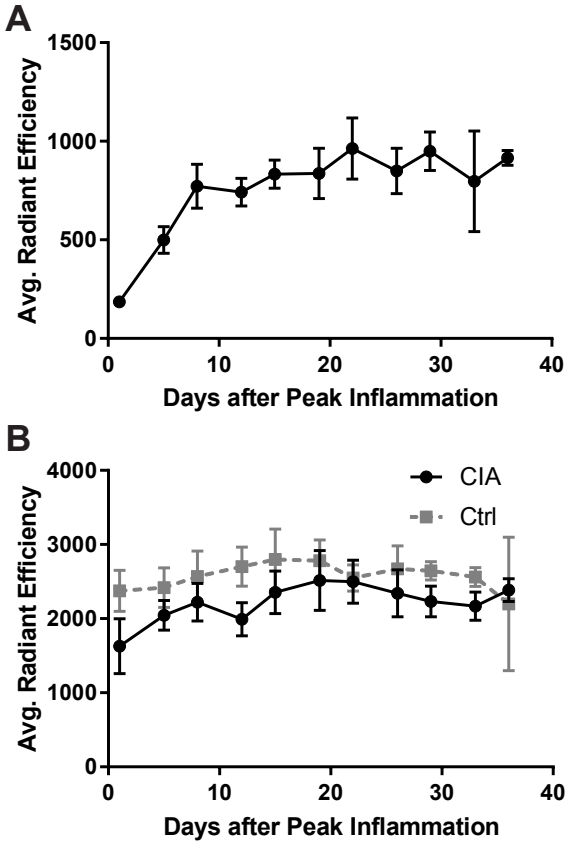

Figure 19: Blood pool concentrations of MMP tracer in mouth region pre- and post-injection. *A* Baseline average radiant efficiency of the mouth region of mice over time, in the resolution phase, before the MMP tracer is administered for imaging. This serves as a background level of the tracer remaining in the blood from previous imaging sessions. *B* Average radiant efficiency of the mouth region 3 hours post-injection, over time, in the resolution phase. This depicts the differing blood pool concentrations of the CIA and control mice over the course of the experiment.

These constitute direct inflammatory effects. There is also uptake in some lymph nodes and the spleen as they are parts of the lymphatic system, active during inflammatory processes. It is important to keep in mind that this image depicts a different tracer than those which we are using, but it serves to illustrate that there are other sites within the murine model of CIA, which are inflamed and therefore would bind the S100A9 and MMP tracers without being visible using our method.

Considering the complexity of the model and taking into consideration the confounding factors stated above, a normalization strategy was employed. The signal to background ratio using the muscle background created a robust baseline that represents the concentration of

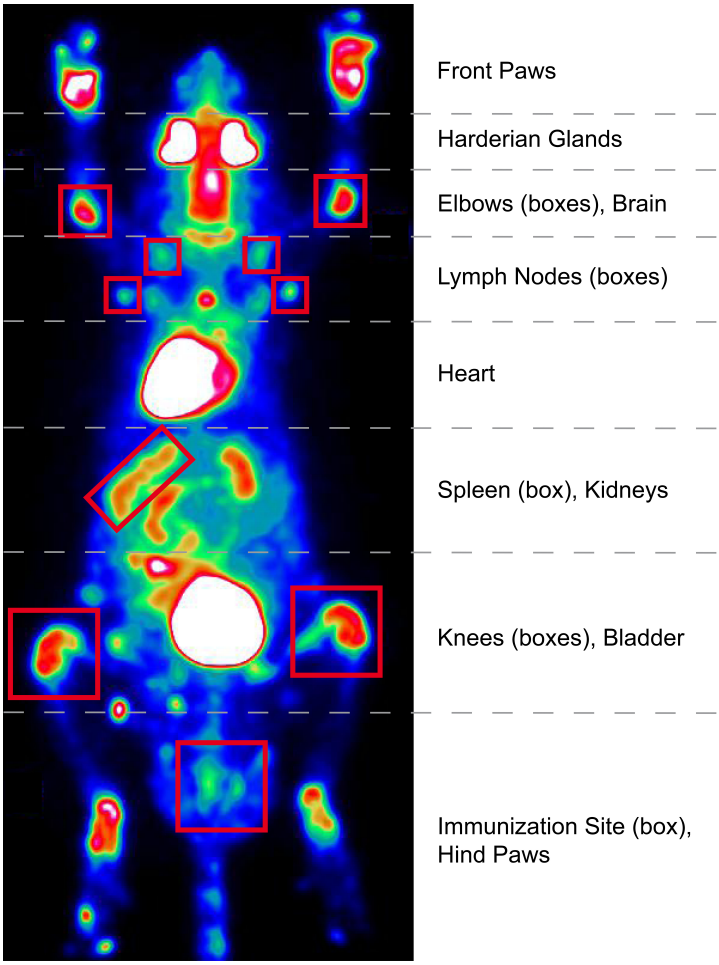

Figure 20: FDG-PET in CIA. A maximum intensity projection (MIP) of a CIA mouse having recieved FDG. This is a static PET scan from 60-75 min post injection. The tracer is generally taken up in areas of high metabolic activity, such as sites of inflammation. Here, front and rear paws exhibit high FDG uptake indicative of high inflammatory activity. Additional sites of inflammatory activity are marked with red boxes. These would not be seen via FRI due to the presence of fur. Non-specific uptake takes place in the Harderian glands. The heart and brain require consistent, high levels of energy to maintain life and therefore readily uptake FDG. The kidneys and bladder are well defined as they excrete the tracer. This image serves to illustrate the FRI-invisible areas of inflammatory activity where our tracers might bind.

tracer still available in the blood pool and normalizes for variability between experimental days, injections, and interanimal variability.

5.4.2 Thresholded SBR Inflammatory Area Analysis Method

In addition to the whole paw mean SBR analysis, which was employed to perform the analyses shown in Sections 5.1 and 5.2, other analyses were investigated. It was thought that the mean analysis might be too crude to capture cases such as the single inflamed joint pictured in Figure 18. To this end, two other analyses were developed. The first was an inflammatory area analysis, where the SBR is generated for the entire paw image, and the area exceeding a user defined SBR threshold is calculated.

Figure 21A shows a single paw example where the areas remaining after thresholding are depicted. The threshold focuses the analysis on a particular intensity of presumed inflammatory activity. As the threshold is increased, smaller areas are observed. Figure 21B-D show the resolution phase analyzed using this method with different thresholds of the SBR ranging from 1.5 to 2.5 times the mouth background. It is apparent that the success of the analysis and the conclusions that can be drawn from it are dependent upon choosing the proper threshold.

5.4.3 Thresholded SBR Inflammatory Fraction Analysis Method

The second method was an inflammatory fraction analysis, where the SBR is generated for the entire paw image and the fraction of pixels exceeding a user defined SBR threshold is calculated. This was developed in order to normalize for the differences in front and hind paw size. In this way, differences in joint size or in the tissue makeup of front and hind paws could be brought under a single analysis method without the larger hind paws having an outsized effect.

The inflammatory fraction analysis method was similarly dependent upon the choice of threshold. In order to determine the optimal threshold for both methods, a receiver operating characteristic (ROC) curve was calculated.

5.4.4 Receiver Operating Characteristic for optimal threshold determination

The ROC is a method used to assess a diagnostic test. It plots a curve comparing the true positive rate, or sensitivity, in our case the CIA mouse paws with SBRs above the threshold, as a function of the false positive rate, 100 % - specificity, in our case the control paws with SBRs above the threshold. When these rates are plotted against each other for varied thresholds, a curve emerges. While the perfect discriminator would have true positive rate of 100 % and a false positive rate of 0 % , this is rarely the case when developing diagnostics. Therefore, we must consider a tradeoff between sensitivity and specificity in determining the optimal cut-off for our application.

It is important to note that any given threshold produces the same area/pixels regardless

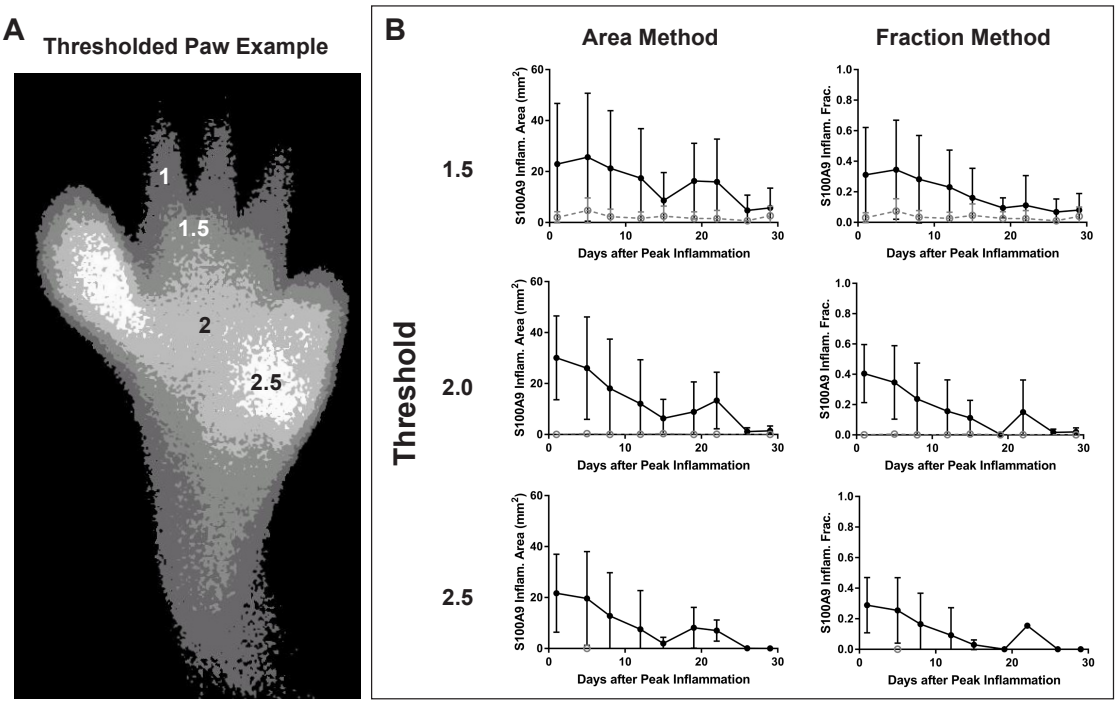

Figure 21: Thresholding of paws based on SBR to compare area and fraction methods. *A* Hind paw of a CIA mouse imaged for S100A9 on day 11 with a clinical score of 2. In this example, SBR thresholds from 1 (representing the whole paw) to 2.5 are displayed at intervals of 0.5. Increasing the threshold reveals a lower number of pixels and a smaller area. *B* Side-by-side comparison of the Area and Fraction Method outputs for S100A9 in the resolution phase. Pictured are the SBR thresholds 1.5 - 2.5. The choice of threshold creates significant changes in the shape and height of the curves in both methods. While both methods are based on the same thresholded data, the metrics produce distinct results.

of whether one performs the inflammatory area or fraction analysis method. The area and fraction are different metrics but are based on the same underlying thresholded data. This means that when a threshold exceeds the maximal SBR present in a ROI, the particular paw is no longer included at the same time in both analyses. It is for this reason that it is not necessary to calculate an ROC curve for each analysis type.

An ROC curve was created for each tracer and in both the onset phase and the resolution phase (Figure 22). A "no discrimination" line can be drawn at a 45°angle between the origin and the upper right hand corner. This line represents a random discriminator where no matter the threshold chosen, the same proportion of positive and negatives will be returned. If the curve lays below this line, one can simply reverse the decision of the discriminator (positive result is now negative and vice versa) and it will mirror over the no discriminator line and become positive.

When assessing a diagnostic it is important to choose a cut-off based on the desired sensitivity or specificity. For the purposes of screening, for instance, a choice of high sensitivity is desired so that true positives are not missed. Further assessments may be done afterwards to check the validity of the positive result. Sometimes it is more desirable to ensure healthy

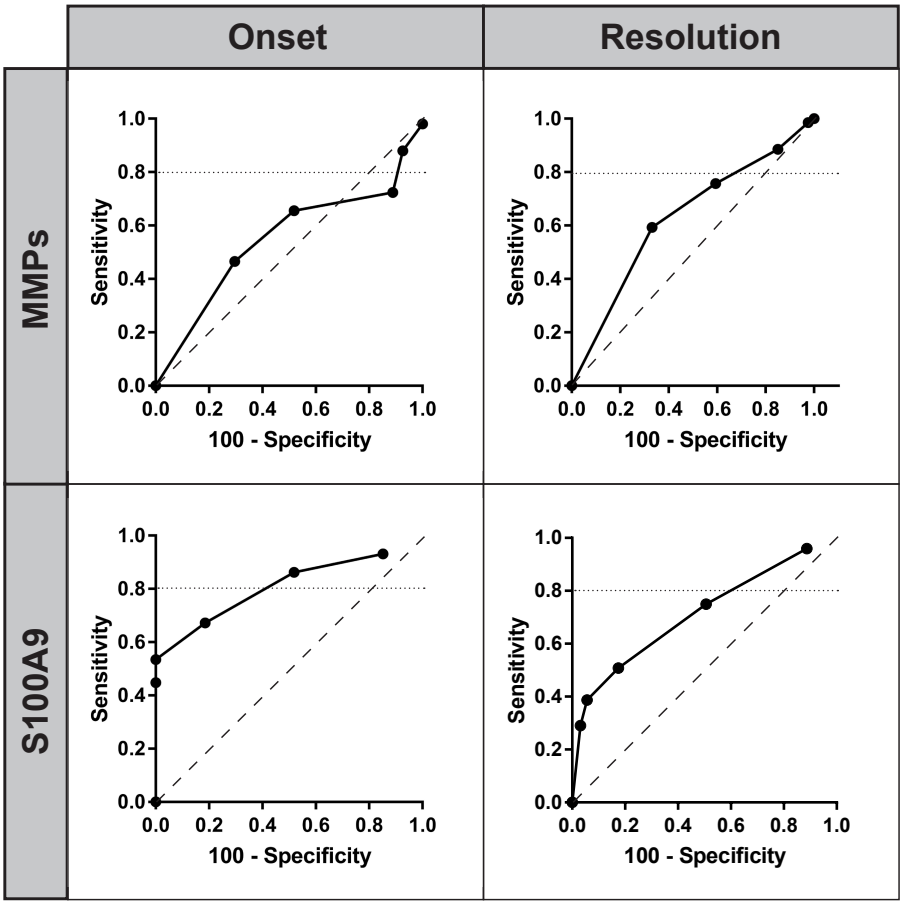

Figure 22: Receiver operating characteristics of thresholded SBR images of MMP and S100A9 tracers in the onset and resolution phase. ROC curves corresponding to each phase and tracer. A point was placed at the origin with each further point along the curve representing increasing thresholds between 1.5 and 2.5 at intervals of 0.25. The dashed line represents the line of no discrimination also termed a random discriminator. The dotted line at 0.8 sensitivity is the 80 % sensitivity cut-off chosen for threshold selection.

patients (true negatives) are identified, for instance in cases of invasive surgery for relatively benign ailments. For our purposes we chose a high cut-off of 80 % sensitivity, as in the case of arthritis, it is important to catch inflamed joints as early as possible to prevent further inflammatory development and joint destruction. A dotted line is used to demarcate the cut-off in Figure 22.

The thresholds exceeding the cut-off criteria were 2.25 for MMPs in the onset phase, 2 for MMPs in the resolution phase, 2.25 for S100A9 in the onset phase and 2.5 for S100A9 in the resolution phase. In the case of MMPs and the resolution phase of S100A9, we found that the threshold which exceeded 80 % was very close to the line of no discrimination. Only in the case of S100A9 in the onset phase were we able to find a discriminator that maintained a specificity that was not close to random. One can also observe that the thresholds exceeding the cut-off in the onset phase were the same across both tracers. However, the thresholds for

each single tracer were different for each phase.

Visual inspection of the MMP ROC curves show that they remain close to the line of no discrimination and do not appear to be good discriminators. The S100A9 curves show better characteristics, although to meet the cut-off, the resolution phase loses specificity and comes very close to the line of no discrimination.

Due to the lack of internal consistency of thresholds within tracers and that 3/4 ROC curves proved to be close to a random discriminator above the cut-off, the thresholded analyses were determined to add little value to the analysis and these methods were not followed any futher.

6 Discussion

Rheumatoid arthritis is an autoimmune disease causing pain and disability in up to 1% of the population (McInnes and Schett, 2017). Although various therapeutic options are available, interventions are typically based on symptoms and are usually administered after first signs of inflammatory flares are present (Majithia and Geraci, 2007). However, symptoms indicate that damage is already taking place. New diagnostic and prognostic tools based on biomarkers of inflammation, which predict and monitor an inflammatory flare before it strikes, are warranted to reduce harm and improve the management of RA through pre-emptive treatment (Saleem et al., 2012).

The aim of this thesis was to develop a novel, optically based, fluorescent, non-invasive, diagnostic/prognostic tool for the examination of inflammatory articular manifestations of RA. It was also important that this imaging strategy be translatable to clinics. We successfully investigated two imaging biomarkers (S100A9 and MMPs), longitudinally, using optical methods, laying the groundwork for further targeted investigations of inflammatory biomarkers with a view towards translational and individualized medicine.

We chose fluorescence due to its lack of ionizing radiation, rapid image acquisition, ability to image multiple biomarkers simultaneously and the relative low cost as well as considerable potential for bedside imaging (Ntziachristos and Razansky, 2010). Frequent serial monitoring with radionuclide-based imaging would result in cumulative radiation exposure to the patient. Additionally, scintigraphic acquisitions can be lengthy in order to collect sufficient count statistics. In contrast, an in-clinic fluorescence device allowing for quick, safe and non-radioactive administration of a tracer as well as simple acquisition and reading of the images could establish optical monitoring of disease progression and improve outcomes while reducing costs.

6.1 Multiplexing small molecule probes provided novel insight into concurrent expression of MMPs and S100A8/A9

In this study we aimed to non-invasively monitor inflammatory activity in the joints of CIA mice using molecular imaging with small, non-peptidic targeted fluorescent probes during onset and resolution of disease. We hypothesized that molecular imaging diagnostics would be more sensitive than clinical inspection and we aimed to further characterize and compare the time courses of S100A8/A9 and MMP expression. Using concurrent injection and imaging of two probes, targeting active MMPs and S100A9 in the same mouse over time we were able to show that MMP and S100A8/A9 expressions show a concurrent, dynamic rise in the onset phase and decline in the resolution phase and that signals are correlated with clinical scores.

In a previous study, Scales et al., (2015) were already able to follow MMP expression using the activatable probe MMPSense 750 FAST in CIA during the onset and beginning of the resolution phase. While the measurements were taken at longer time intervals, they were still able to show a characteristic rise and fall, which corresponded roughly with the clinical

score. Interestingly, they too were unable to observe a difference between control and CIA mice until the disease was in an advanced state. They posit that this is due to the ability of MMPSense 750 FAST to be activated by multiple types of MMPs. While this may be true, we saw in correlating histology that MMP-9 levels are relatively low until advanced states of disease and our results using a small molecule probe binding to active MMPs corroborate this finding.

Important to note is the speed with which imaging can be conducted with the small molecule probes and the achievable signal to background ratios as compared with activatable probes. Waschkau et al. (2013) examined a related small molecule MMP inhibitor coupled with Cy5.5 for FRI imaging in comparison with MMPSense 750 FAST and found that while MMPSense had slightly higher signal to background ratios, these occurred much later, at around 24 hours rather than between 45 min and 6 hours. This limits the usefulness of the probe as it must be administered well ahead of imaging. Additionally, the long circulation times and slow activation decrease the usefulness of the probe in longitudinal studies due to high background signals during subsequent imaging sessions, as can be seen in Scales et al. (2015). The fast binding and fast clearance of a small molecule ligand allows for quick repetition of measurements, every 3 or 4 days, as opposed to long circulating activatable probes that required between 7 and 14 day intervals between measurements.

In addition to monitoring of the progression of disease and inflammatory activity using the clinical score and imaging of MMP expression, we also used a novel, recently developed non-peptidic ligand coupled to a fluorescent tracer targeting S100A9 for the first time in CIA and were able to track S100A8/A9 expression through both the onset and resolution phases. Previously, we have employed fluorescently labelled anti-S100A8, developed in our group, to image the S100A8/A9 complex in a seronegative experimental arthritis model (Vogl et al., 2014; Geven et al., 2016). While the tracking of S100A8/A9 in serum has been conducted longitudinally and was found to be prognostic for the development of disease, imaging only took place at a single time point, allowing for a correlation of S100A8/A9 levels to MMP-mediated cartilage damage but not the concurrent investigation of the dynamics of both MMP activity and S100A8/A9 expression throughout the disease process. Our approach expands the scope, allowing for imaging of polyarthritis in the small joints over time in a model more closely related to the human disease presentation and using a tracer with high translational potential.

6.2 No time shift between the expression of S100A8/A9 and MMPs was found

We observed the increase and subsequent decrease of the expression of alarmin S100A9 and the extracellular matrix remodelling proteins, the MMPs, happening in relative synchrony. Initially, we had hypothesized that S100A8/A9, the upstream activator of inflammatory activity, might be an early diagnostic and prognostic biomarker as it leads to the expression of effector molecules, for instance, the MMPs. However, the time resolution of our longitudinal

study did not allow for the visualization of the steps in inflammatory upregulation with sufficient granularity to elucidate this cause and effect relationship using imaging.

While we could not detect a shift between the two mechanistically interrelated pro-inflammatory players, there seems to be a trend showing earlier peaking of S100A8/A9 expression before MMP expression in the resolution phase of CIA. A small time difference was predicted as the literature states, S100A8/A9 is an upstream regulator of MMP expression. This was shown in a model of antigen induced arthritis (AIA) (Lent et al., 2008a), where the S100A8/A9 complex was demonstrated to upregulate MMPs and injection of S100A8 by itself increased cartilage breakdown, induced further transcription of the S100A8/A9 complex and increased expression of MMPs and cytokines. With S100A8/A9 as one of the drivers and regulators of myeloid inflammation, an earlier peak expression relative to an increasing MMP activity would fit mechanistically. However, in both our study and another study (Lent et al., 2008a) it could not be corroborated with imaging. In the case of Lent et al. the peak of S100A8/A9 and MMPs on day 1 had dropped concurrently by day 3 post-induction of AIA. In both studies, the time resolution of measurements was 3 ± 1 days. This resolution is too granular to pick up differences in time to peak expression of S100A8/A9 and MMPs as these processes are highly dynamic. In an experiment in AIA (van Meurs et al., 1999), MMP mRNA levels peaked within 12 hours of challenge. This could mean that any time shift in S100A8/A9 levels and MMP levels may be on the order of hours during the onset phase, which is well below the time resolution of our current imaging setup. S100A8/9 and MMPs cannot, therefore, be used to predict an inflammatory flare. This indicates a need for investigation of further biomarkers that are present even earlier in the inflammatory cascade in order to realize pre-emptive treatments.

6.3 Histology corroborated S100A9 and MMP-9 imaging data

The histological investigation of S100A9 and MMP-9 corroborated S100A8/A9 and MMP imaging data in all examples shown. H&E staining showed the expected morphological phenotypes for controls and clinical scores 1 - 3. Large morphological changes were found to coincide with the upregulation of S100A8/A9 and MMPs, as expected.

Imaging data consistently showed co-localization of S100A9 and MMP tracers. In histology, S100A9 levels correlate well with the levels of MMP-9 in a given paw indicating their regionally co-localized expression, which follows from the fact that S100A8/A9 is an upstream activator of MMP expression and activation.

As stated previously, Scales et al. (2015) could only show a significant increase in MMP signal in an advanced disease state. Our findings corroborate this, as we could only see significant upregulation of MMP SBRs in paws with clinical scores of 3 in the onset phase and clinical scores of 1.5 and above in the resolution phase. This finding was further supported by histology where only paws of clinical score 2 and 3 showed significant presence of S100A9 and MMP-9. The absence of target at lower clinical scores could explain the inability of the method to differentiate between clinical scores 0 and 1. When there is not a significant target

concentration available to be bound by the tracer in a paw with a clinical score of 1, the signal will be low and within the range of controls.

Both the example of the clenching clinical score 3 paw showing a late stage of disease and the example of single joint inflammation further proved the validity of our imaging method. A low level of disease activity late in the resolution phase was shown in both the imaging data and histology regardless of the clinical score. Low S100A9 and MMP-9 expression is seen and low SBRs for both tracers are also shown. These results were able to show the increase in clinical score and the clenching itself was not due to a renewed, acute, inflammatory process taking place at this late time point, but rather a residual effect of the remodeling of tissue.

The single joint histology image showed the promise of the method. Colocalization of S100A9 and MMP-9 was observed and it was exclusive to the joint showing increased MMP FRI signal. The fact that such a clear signal was present in the MMP FRI signal but not in the S100A9 signal while the presence of both proteins was confirmed by histology is curious. It may be due to the generally lower SBRs seen using S100A9. The IRDye 800CW fluorophore attached to the S100A9 binding CES271 ligand has a lower quantum yield of fluorescence, and therefore a lower signal in general. While we normalize the images to mitigate these effects, it may not have been sufficient in this case. It was clear that MMPs were present as they had contributed to bone degradation, which can be seen both in H&E as well as in the X-ray image. This example pushes the limits of the method and further development is needed, but this finding is encouraging with regards to the ability of the method to image single joints.

6.4 Division of onset phase CIA mice into fast and slow responding groups

In the onset phase, the fast and slow responder groups were created as the fast responders reached criteria requiring sacrifice 3 days earlier than the time point when the slow responders showed considerable inflammation. Brand et al. (2007) lays out, in a detailed report on the induction of CIA in DBA/1 mice, that the onset of disease for mice within experimental groups varies greatly and that the speed of arthritic development varies between reproductions of the same experiment. It was summarized by Goronzy and Weyand (2001) that environmental factors including stress and light can be significant in changing the susceptibility of mice, and male DBA/1 mice in particular, to CIA. This indicates that the observed variations are typical of the model. This variability reflects a true clinical situation. Arthritic flares are unpredictable in their onset and can range from mild "morning stiffness" to severe pain in multiple joints. Their duration varies, but most are short, lasting less than a week, while others can be more persistent (Bykerk et al., 2014). Jacquemin et al. (2017) showed decreased physical activity and two increased metrics regarding the experience of pain in patients with flares lasting longer than 3 days. There is not significant literature examining the speed of flare onset clinically. It is also important to note that patients participating in clinical studies are undergoing therapy. Discontinuation of therapy has been investigated but was determined

to be unethical as severe flares occurred within 2 months (Kremer et al., 1987). Our division of the onset phase into fast and slow responders is based on the variability in the model. The heterogeneity of the model's development is well documented in the literature and not dissimilar to the variation in RA presentation in the clinic, itself highly heterogeneous.

6.5 The clinical score reflects externally observable markers of inflammation

Clinical score, as a surrogate of inflammatory activity may be useful in a clinical context, however, the standard scoring scheme used for this murine model is rather crude. It is a visual assessment of edema and reddening, which themselves are surrogates of inflammatory activity. The clinical score is used here as a ground truth, but it is not clear if this is a true reflection of inflammatory activity at the paw level. It is a tool of necessity as we do not have more direct ways of assessing inflammation, especially in a way which would be acceptable in terms of animal ethics.

Clinical score takes into account the feet as a singular entity, as characterizing such a murine model at the single joint level is untenable without anaesthesia, causing too much stress for daily control and scoring. The clinical score rubric for the whole paw can be consistently applied but remains somewhat subjective and scoring at a single joint level would likely increase error. However, similar to the human disease, one can see from images, such as those in Figure 18, that the effects on the mouse, as in humans, can occur at the level of a single joint. Figure 18 shows a mouse paw with a clinical score of 1; nevertheless, one can see swelling, infiltration and high expression of both S100A8/A9 and MMPs in fluorescence images and histology.

Another disadvantage of the clinical score is that it consolidates a number of processes into a single subjective indicator. Reddening, edema, skin damage and paw deformation are taken together to assess disease state. This means that a single indicator can have an outsize effect on the clinical score of a paw. An increase in the clinical score in CIA mice is seen in the resolution phase on days 33 and 36 while the S100A9 and MMP SBRs remained stable and decreased, respectively. Histology also confirmed a lack of target S100A9 and MMP-9 in paws with a clinical score of 3 at day 36. The increase in clinical score was due to paw clenching, which brought the clinical score of clenching paws to 3 without erythema or swelling.

The clinical score is the standard practice in clinics (ACR/EULAR, 2010) and in murine models, but it does not represent the most accurate picture of single joint inflammation or inflammatory markers. For longitudinal tracking of inflammation, it is the most efficient and low cost solution, but a more accurate gold standard would be preferred.

6.6 Choice of analysis method and use of signal to background ratio

It is important in any imaging study to consider carefully the choice of analysis method. A particular method can highlight a feature within the data or completely mask another, each method is sensitive to particular perturbances and it is important for the researcher to keep in mind the limitations of their method. In this thesis, particular attention was paid to the method used to assess the inflammatory activity in CIA. As this was a longitudinal study, we had to take into account residual amounts of tracer, small variations in tracer concentration, the number of days between imaging sessions, the effect of a mouse being naïve to the tracer versus being in a saturated state and of course inter-mouse variability.

Initial investigations into the raw average radiant efficiency data indicated that we could not simply use the raw data in order to get an accurate picture of the inflammatory activity and that a form of normalization would be necessary. We decided for signal to background ratio as it is common in molecular imaging to designate a "control" or "background" region which is similar in tissue makeup to the area of interest as a benchmark of background tracer level. Examples of this include the assessment of contralateral brain regions when analyzing stroke models (Zinnhardt et al., 2015), contralateral ears in models of contact dermatitis (Vogl et al., 2014), or regions surrounding an implanted subcutaneous tumor in mice (Korb et al., 2014; Tummers et al., 2018).

We utilized the mouth background region as it was exposed during imaging and had a mix of muscle, skin and jaw bone, similar to the paws. The only other exposed areas included the tail and the anus. The tail is the site of intravenous injection of the tracer. Therefore, it was excluded, as it can contain fluorescent tracer that is not in the blood stream but instead was sequestered in layers of skin adjacent to the injection site. The anus was also excluded as it is an excretion site and could contain tracer in the stool. Additionally, it does not contain the complex mix of muscle, skin and bone present in the mouth region. The rest of the animal's body was covered with fur. It was thought that additional shaving of the animal would cause undue stress as it must be done under anaesthesia and could prevent the model from developing normally. It would also need to be done regularly over the time course, and as hair and hair follicles readily scatter light, it could introduce an additional confounding factor.

This was the first time that the S100A9 and MMP tracers have been used for longer than 72 hours in serial imaging. In the case of the related MMP tracer Cy5.5-AF489 as well as Cy5.5 alone, an imaging study by Waschkau et al. (2013) at 72 hours showed residual tracer signal. It was, therefore, deemed important to investigate the signals originating from the tracer concentrations remaining in the blood pool over a longer time and multiple imaging sessions to aid in the choice of analysis method. We were able to show that beginning at imaging session 3, after 8 days, the residual amount of tracer stabilizes and holds relatively constant over the following 26 days. This information will instruct the design of further studies utilizing these tracers. Using the signal to background ratio, lower blood pool concentrations

during the first two imaging sessions could be accounted for.

6.7 Blood concentration of tracer is lower in CIA mice

The observed difference in the signal of the background mouth region 3 hours after injection is hypothesized to originate from the uptake of tracer in areas of inflammation. As the tracer reaches and binds its target, less tracer is available to freely move through the blood stream. A lower blood concentration in the region that we are using to normalize has a potential effect on the SBRs of CIA mice. The lower denominator in the SBR calculation could serve to artificially elevate the SBRs of the paws. However, there is no reason to believe that this lower blood pool value is not rooted in physiological fact.

As stated earlier, both tracers show elevated uptake in affected paws, particularly paws at and above a clinical score of 2. This elevated uptake removes some circulating tracer. However, in addition to the on-target uptake we can image, the potential for additional sources of the biomarker "robbing" the tracer from the blood pool cannot be excluded. Using an FDG-PET image of a CIA mouse, it was indicated that there are other sites of inflammation where uptake is likely to occur. As stated, it is important to note that FDG and the MMP and S100A9 tracers have differing targets. As the CIA model of RA is a systemic presentation of the disease, it affects joints and organ systems. The image shows that elbow and knee joints as well as the site of immunization would likely show increased tracer uptake in our study had we had the opportunity to image them. Additionally, although not visible in FDG, pulmonary inflammation is noted in RA and CIA (Schurgers et al., 2012) The lymphatic system would also be expected to show increased uptake, in particular for S100A8/A9 as increased levels of neutrophils are found in the spleen (Fishman and Isenberg, 1997) and lymph nodes (Imai et al., 1989) in RA. Lymphatic remodeling and inflammation are known in the CIA model (Billiau and Matthys, 2011). The heart and brain uptake in the FDG scan are based on the great energy needs of these organs. It is unlikely that S100A8/A9 or the MMPs would be sufficiently upregulated in the arthritis model. Potential uptake in the Harderian glands is unknown, but would be expected to be constant between the treatments and not to be affected by the immune activity. Finally, uptake in the excretion organs such as the kidney and bladder would be expected to be relatively constant between treatments.

Unfortunately, these effects can only be speculated about as no previous study has been performed looking at this effect in CIA mice using these two tracers. If a radioactive version of the tracers were to be created, this potential effect could be further investigated.

6.8 Thresholded SBR Area and Fraction analyses considered

The mean SBR of each paw was the method selected for the analysis. The method is robust as it always uses the several thousand pixels per paw to compute its metric. It also has the advantage that, similar to the clinical score, it takes a wholistic assessment of the entire section of the paw made visible to the camera.

This mean method has the drawback, however, that it averages out the effects of small but intense focal lesions such as that seen in the single joint inflammation case study. To this end, we developed two additional analyses to attempt to address this drawback. The analyses are related in that they rely on thresholding the SBR within each ROI and computing a metric on the remaining area or pixels. By increasing the threshold, areas of paws exhibiting lower SBR are excluded, highlighting the areas of higher inflammatory activity.

The area method was developed as a 2D fluorescence analog to assessments of inflammatory volume used in radiology and nuclear medicine. A 3D PET (Saboury et al., 2014), SPECT (Wang et al., 2005) or CT (Giacomini et al., 2015) image is segmented into a volume of interest and thresholded to compute the metric. In our case, we define a ROI and use thresholding to compute an inflammatory area.

We also considered the affect that fore and hind paw size might have on the analysis and created a fraction method that computed the fraction of pixels, within the ROI, exceeding the threshold. This serves to make the fore and hind paws more readily comparable.

The results produced were heavily dependent upon the threshold chosen. This is a drawback of these methods as they require the tuning of a parameter. We saw that the shape of the curves produced by both methods changed considerably as the threshold was increased. Paws falling under the threshold are no longer included. This would be an advantage if the distributions of control and CIA paws were sufficiently different from one another or mutually exclusive. However, in these methods, we found many CIA paws were also thresholded to zero.

6.9 ROC curves indicate limited applicability of thresholding methods

As explained in Section 5.4.4 an ROC curve can be used to define an optimal threshold for a desired level of sensitivity or specificity. In our case, we chose to put a high priority upon finding a true positive, in other words to find the paws of CIA mice with a clinical score of 0.5 or above. Prioritizing detection means choosing a high sensitivity at the cost of specificity. We chose the cut-off of 80 % sensitivity and assessed the first threshold which exceeded this cut-off criteria. This is high, but the imaging technique was designed to serve as a screen of paws, detecting potentially debilitating inflammation and remodeling of tissue. This is analogous to the clinical setting where the cost of missing an inflamed joint is high, potentially causing the patient severe pain and temporary or even permanent loss of function.

As a result of our choice of cut-off, the specificity achieved by the method in all but one case was unacceptable. The performance in the case of the MMP tracer in both phases and the S100A9 tracer in the resolution phase were akin to a random discriminator, where one could imagine a "diagnostic test" that given an image of a paw as input would randomly assign it to a class (CIA or control). Due to these results, these analysis methods were deemed unfit for purpose in this case and the mean SBR method was employed for the final analysis.

6.10 FRI in the clinic

As a new research direction towards improved characterization of inflammatory activity in RA, clinical FRI, e.g. with dedicated hand scanners, has been established (Hansch et al., 2004; Fischer et al., 2010; Krohn et al., 2015; Glimm et al., 2016). Although this approach seems clinically capable of measuring perfusion and blood volume when combined with clinically approved non-targeted contrast agents it is still limited by the non-availability of targeted contrast agents.

The FRI method we have established could be used for superficial imaging of the hands, for instance, and has already been used successfully with non-targeted ICG (Fischer et al., 2010; Glimm et al., 2016; Krohn et al., 2015). Based on our proof-of-principle study in CIA, future developments should focus on establishing GMP-conforming, non-toxic tracers for fluorescence imaging.

In addition, there may be a potential for S100A8/A9 based non-invasive imaging to differentiate RA from miscellaneous inflammatory arthritides (MIA). In a paper by Baillet et al. (2010) it was found that enhanced synovial levels of S100A8, S100A9 and S100A12 discriminated between RA and MIA. This involved taking synovial fluid samples from affected joints and laboratory workups using mass spectrometry, western blotting and ELISA. The S100A8/A9 tracer administered and imaged optically could be a plausible application and could reduce the need for biopsies in cases where the type of arthritis is unclear.

6.11 Photoacoustic imaging of Naphthalocyanine labelled ligands presents a 3D diagnostic opportunity

Similar to FRI, photoacoustic imaging uses light to excite molecules but detects sound originating from the light excitation as signal. This has a number of advantages when compared with FRI. Recalling the Beer-Lambert law stated in Section 2.3.1, the attenuation coefficient for sound moving through aqueous or solid media is low when compared with light. Signal produced as sound is able to travel out from deeper within the sample or organism (Yao and Wang, 2011). Whereas a photon has but one direction, sound is emitted as a wave, allowing for localization using existing ultrasound reconstruction techniques. While acoustic waves also suffer from scattering and attenuation, these phenomena are well studied and understood in the field of ultrasound imaging and occur less than these phenomenon for light in tissues (Beard, 2011). The use of light to excite the molecules allows the technique to distinguish between sonophores, the molecules emitting sound, as molecules respond variously to different wavelengths of light. Scanning through a set of wavelengths will produce a spectrum of response from a particular sonophore. By varying the wavelength of light, one can preferentially excite certain molecules over others. Mathematical models can help choose a set of excitation wavelengths that will allow for spectral unmixing (Tzoumas et al., 2014). These techniques allow for, to date, qualitative assessments of tracer distribution within the sample. For molecular imaging, this is an advantage as there is the potential to image

multiple tracers simultaneously.

When imaging arthritis, PA has the advantage of being able to image to a depth of multiple centimetres, facilitating imaging of limbs, hands and feet. Through the use of established tomographic reconstructions, 3D volumes constituting entire limbs can be examined. The ability to assess multiple parameters simultaneously using different tracers and the ease with which a tomographic photoacoustic system can capture anatomical information using conventional ultrasound come together to pose an attractive diagnostic solution that is low cost, fast, sensitive, and co-registered with anatomical information.

Photoacoustically active substances are often called dyes as they absorb light and have color. In clinical studies the FDA approved molecule ICG is prevalent. While it is proven safe and can already be used in clinics, it has a number of drawbacks. It is difficult to modify, its quantum yield of fluorescence is high and the spectrum of ICG changes based on concentration and pH, which makes multispectral unmixing more difficult (Kim et al., 2010). ICG is a member of the cyanine dye class of molecules to which Cy5.5 and IRDye 800CW also belong. These molecules do not alter their spectrum drastically as concentration or pH changes and IRDye 800CW is often linked to ligands for molecular imaging (Kim et al., 2010; Huang et al., 2012; Hsiao et al., 2013; Attia et al., 2016). Because it has the advantage of being easily modifiable and as it produces both photoacoustic and fluorescent signals, the results of a study can be corroborated in a multimodal imaging scheme (e.g. a photoacoustic scan with follow up *ex vivo* fluorescence measurements.)

Unfortunately cyanine dyes have the drawback that they readily photobleach. As a scan takes place, some excited electrons move into the triplet state and upon coming in contact with oxygen, a reactive oxygen species (ROS) is formed. This can oxidize the fluorophore and cause it to no longer be excitable, eliminating both the photoacoustic and fluorescent abilities of the molecule (Yang et al., 2001; Laufer et al., 2010). Through repeated illumination, the proportion of photobleached molecules is increased and the signal decreased (Li et al., 2013). Therefore, as a sample or organism is scanned, the scattered photons can excite molecules outside of the plane of detection and bleach some of them before they are ever detected. The calculated distribution of the tracer can be disturbed by this phenomenon.

Considering the absence of dyes with optimized characteristics for PA, Naphthalocyanines are interesting lead structures for the creation of *in vivo* sonophores because they display high stability and absorb in the NIR spectrum (Kumar and Santhosh, 2003). Their macrocycles possess a large delocalized pi-electron system. The delocalization and aromaticity gives the Nc high thermal and chemical stability (Wheeler et al., 1984). This also decreases the ability of the molecule to photobleach as it will be less likely to undergo oxidation or to dissociate by excitation of vibrational modes after radiationless deactivation into the ground state (Diaspro et al., 2006; Montalti et al., 2006; Michl, 2006). In order to design a Naphthalocyanine optimized for PA, we performed a screen and found that Nickel Naphthalocyanines with a distal substitution performed best (Duffy et al., 2018). A water soluble and targetable version of this Naphthalocyanine is currently being synthesized for use in PA imaging of RA.

Through the further analysis and future synthesis of Naphthalocyanines with properties

tailored to photoacoustic production, it could be possible to produce highly photoacoustically active species for use in diagnostics.

7 Conclusions and Outlook

Our small ligand-based molecular imaging approach accurately and concurrently monitors the inflammatory markers S100A8/A9 as well as active MMPs in the onset and resolution phases of CIA, a murine model of RA using optical and non-radioactive FRI. No time difference in the peak expression of S100A9 and MMPs could be confirmed. We were able to visualize inflammation down to the level of single joints using a novel set of MMP and S100A9 targeted fluorescent tracers, which due to their non-peptidic nature have high translational potential. Attaching the ligand CES271 targeting S100A8/A9 and AF443 targeting MMPs to different, water soluble Naphthalocyanines would allow for the use of these ligands as tracers for PA molecular imaging. PA's use in arthritis would allow for 3D images of affected joints. Currently, work is being done by a colleague on another model of RA, AIA, to establish PA molecular imaging using IRDye 800CW-CES271 to great success. Additionally, the development of probes compatible with nuclear SPECT and PET imaging is currently underway with the advantage of better quantification for precision medicine.

References

ACR/EULAR (2010). Classification Criteria for Rheumatoid Arthritis. *Classif. Criteria Rheum. Arthritis*.

Aggarwal, R., Liao, K., Nair, R., Ringold, S., and Costenbader, K. H. (2009). Anti-citrullinated peptide antibody assays and their role in the diagnosis of rheumatoid arthritis. *Arthritis Rheum.*, 61(11):1472–83.

Alamanos, Y. and Drosos, A. (2005). Epidemiology of adult rheumatoid arthritis. *Autoimmun. Rev.*, 4(3):130–136.

Andersen, T. L., del Carmen Ovejero, M., Kirkegaard, T., Lenhard, T., Foged, N. T., and Delaissé, J.-M. (2004). A scrutiny of matrix metalloproteinases in osteoclasts: evidence for heterogeneity and for the presence of MMPs synthesized by other cells. *Bone*, 35(5):1107–1119.

Araki, Y. and Mimura, T. (2017). Matrix Metalloproteinase Gene Activation Resulting from Disordred Epigenetic Mechanisms in Rheumatoid Arthritis. *Int. J. Mol. Sci.*, 18(5):905.

Asquith, D. L., Miller, A. M., McInnes, I. B., and Liew, F. Y. (2009). Animal models of rheumatoid arthritis. *Eur. J. Immunol.*, 39(8):2040–2044.

Atallah, M., Krispin, A., Trahtemberg, U., Ben-Hamron, S., Grau, A., Verbovetski, I., and Mevorach, D. (2012). Constitutive neutrophil apoptosis: regulation by cell concentration via S100 A8/9 and the MEK-ERK pathway. *PLoS One*, 7(2):e29333.

Attia, A. B. E., Ho, C. J. H., Chandrasekharan, P., Balasundaram, G., Tay, H. C., Burton, N. C., Chuang, K.-H., Ntziachristos, V., and Olivo, M. (2016). Multispectral optoacoustic and MRI coregistration for molecular imaging of orthotopic model of human glioblastoma. *J. Biophotonics*, 9(7):701–708.

Averill, M. M., Kerkhoff, C., and Bornfeldt, K. E. (2012). S100A8 and S100A9 in Cardiovascular Biology and Disease. *Arterioscler. Thromb. Vasc. Biol.*, 32(2).

Baillet, A., Trocme, C., Berthier, S., Arlotto, M., Grange, L., Chenau, J., Quetant, S., Seve, M., Berger, F., Juvin, R., Morel, F., and Gaudin, P. (2010). Synovial fluid proteomic fingerprint: S100A8, S100A9 and S100A12 proteins discriminate rheumatoid arthritis from other inflammatory joint diseases. *Rheumatology*, 49(4):671–682.

Beard, P. (2011). Biomedical photoacoustic imaging. *Interface Focus*, 1(4):602–31.

Becker, A., Große Hokamp, N., Zenker, S., Flores-Borja, F., Barzcyk, K., Varga, G., Roth, J., Geyer, C., Heindel, W., Bremer, C., Vogl, T., and Eisenblaetter, M. (2015). Optical in vivo imaging of the alarmin S100A9 in tumor lesions allows for estimation of the individual malignant potential by evaluation of tumor-host cell interaction. *J. Nucl. Med.*, 56(3):450–6.

Beiderwellen, K., Grueneisen, J., Ruhlmann, V., Buderath, P., Aktas, B., Heusch, P., Kraff, O., Forsting, M., Lauenstein, T. C., and Umutlu, L. (2015). [18F]FDG PET/MRI vs. PET/CT for whole-body staging in patients with recurrent malignancies of the female pelvis: initial results. *Eur. J. Nucl. Med. Mol. Imaging*, 42(1):56–65.

Bendele, A., Mccomb, J., Gould, T., Mcabee, T., Sennello, G., Chlipala, E., and Guy, M. (1999). Animal Models of Arthritis: Relevance to Human Disease. *Toxicol. Pathol.*, 27(1):134–142.

Bhardwaj, R. S., Zotz, C., Roth, J., Goebeler, M., Mahnke, K., Falk, M., Meinardus-Hager, G., Sorg, C., and Zwadlo-Klarwasser, G. (1992). The calcium-binding proteins MRP8 and MRP14 form a membrane-associated heterodimer in a subset of monocytes/macrophages present in acute but absent in chronic inflammatory lesions. *Eur. J. Immunol.*, 22(7):1891–1897.

Billiau, A. and Matthys, P. (2011). Collagen-induced arthritis and related animal models: How much of their pathogenesis is auto-immune, how much is auto-inflammatory? *Cytokine Growth Factor Rev.*, 22:339–344.

Billinghurst, R. C., Dahlberg, L., Ionescu, M., Reiner, A., Bourne, R., Rorabeck, C., Mitchell, P., Hambor, J., Diekmann, O., Tschesche, H., Chen, J., Van Wart, H., and Poole, A. R. (1997). Enhanced cleavage of type II collagen by collagenases in osteoarthritic articular cartilage. *J. Clin. Invest.*, 99(7):1534–45.

Boellaard, R., Delgado-Bolton, R., Oyen, W. J. G., Giammarile, F., Tatsch, K., Eschner, W., Verzijlbergen, F. J., Barrington, S. F., Pike, L. C., Weber, W. A., Stroobants, S., Delbeke, D., Donohoe, K. J., Holbrook, S., Graham, M. M., Testanera, G., Hoekstra, O. S., Zijlstra, J., Visser, E., Hoekstra, C. J., Pruim, J., Willemsen, A., Arends, B., Kotzerke, J., Bockisch, A., Beyer, T., Chiti, A., and Krause, B. J. (2015). FDG PET/CT: EANM procedure guidelines for tumour imaging: version 2.0. *Eur. J. Nucl. Med. Mol. Imaging*, 42(2):328–354.

Bouma, G., Lam-Tse, W. K., Wierenga-Wolf, A. F., Drexhage, H. A., and Versnel, M. A. (2004). Increased serum levels of MRP-8/14 in type 1 diabetes induce an increased expression of CD11b and an enhanced adhesion of circulating monocytes to fibronectin. *Diabetes*, 53(8):1979–86.

Boyce, E. G., Vyas, D., Rogan, E. L., Valle-Oseguera, C. S., and O'Dell, K. M. (2016). Impact of tofacitinib on patient outcomes in rheumatoid arthritis - review of clinical studies. *Patient Relat. Outcome Meas.*, 7:1–12.

Boyd, J. H., Kan, B., Roberts, H., Wang, Y., and Walley, K. R. (2008). S100A8 and S100A9 Mediate Endotoxin-Induced Cardiomyocyte Dysfunction via the Receptor for Advanced Glycation End Products. *Circ. Res.*, 102(10).

Boyle, W. J., Simonet, W. S., and Lacey, D. L. (2003). Osteoclast differentiation and activation. *Nature*, 423(6937):337–342.

Brackertz, D., Mitchell, G. F., and Mackay, I. R. (1977). Antigen-induced arthritis in mice. I. Induction of arthritis in various strains of mice. *Arthritis Rheum.*, 20(3):841–50.

Brand, D. D. (2005). Rodent models of rheumatoid arthritis. *Comp. Med.*, 55(2):114–22.

Brand, D. D., Latham, K. A., and Rosloniec, E. F. (2007). Collagen-induced arthritis. *Nat. Protoc.*, 2(5):1269–75.

Bremer, C., Werner, S., and Langer, H.-E. (2009). Assessing Activity of Rheumatic Arthritis with Fluorescence Optical Imaging Current Imaging Techniques in Rheumatoid Arthritis. *Eur Musculoskelet Rev*, 1(4):96–100.

Bresnihan, B., Alvaro-Gracia, J. M., Cobby, M., Doherty, M., Domljan, Z., Emery, P., Nuki, G., Pavelka, K., Rau, R., Rozman, B., Watt, I., Williams, B., Aitchison, R., McCabe, D., and Musikic, P. (1998). Treatment of rheumatoid arthritis with recombinant human interleukin-1 receptor antagonist. *Arthritis Rheum.*, 41(12):2196–2204.

Brew, K., Dinakarpandian, D., and Nagase, H. (2000). Tissue inhibitors of metalloproteinases: evolution, structure and function. *Biochim. Biophys. Acta - Protein Struct. Mol. Enzymol.*, 1477(1-2):267–283.

Burrage, P. S., Mix, K. S., and Brinckerhoff, C. E. (2006). Matrix metalloproteinases: role in arthritis. *Front. Biosci.*, 11:529–43.

Buttgereit, F., Straub, R. H., Wehling, M., and Burmester, G.-R. (2004). Glucocorticoids in the treatment of rheumatic diseases: An update on the mechanisms of action. *Arthritis Rheum.*, 50(11):3408–3417.

Bykerk, V. P., Shadick, N., Frits, M., Bingham, C. O., Jeffery, I., Iannaccone, C., Weinblatt, M., and Solomon, D. H. (2014). Flares in Rheumatoid Arthritis: Frequency and Management. A Report from the BRASS Registry. *J. Rheumatol.*, 41(2):227–234.

Cambridge, G., Leandro, M. J., Edwards, J. C. W., Ehrenstein, M. R., Salden, M., Bodman-Smith, M., and Webster, A. D. B. (2003). Serologic changes following B lymphocyte depletion therapy for rheumatoid arthritis. *Arthritis Rheum.*, 48(8):2146–2154.

Carlsen, H., Moskaug, J. Ø., Fromm, S. H., and Blomhoff, R. (2002). In vivo imaging of NF-kappa B activity. *J. Immunol.*, 168(3):1441–6.

Carlsén, S., Hansson, A. S., Olsson, H., Heinegård, D., and Holmdahl, R. (1998). Cartilage oligomeric matrix protein (COMP)-induced arthritis in rats. *Clin. Exp. Immunol.*, 114(3):477–84.

Carlsen, S., Nandakumar, K. S., Bäcklund, J., Holmberg, J., Hultqvist, M., Vestberg, M., and Holmdahl, R. (2008). Cartilage oligomeric matrix protein induction of chronic arthritis in mice. *Arthritis Rheum.*, 58(7):2000–2011.

Cesaro, A., Anceriz, N., Plante, A., Pagé, N., Tardif, M. R., and Tessier, P. A. (2012). An Inflammation Loop Orchestrated by S100A9 and Calprotectin Is Critical for Development of Arthritis. *PLoS One*, 7(9):e45478.

Chen, W.-T., Mahmood, U., Weissleder, R., and Tung, C.-H. (2005). Arthritis imaging using a near-infrared fluorescence folate-targeted probe. *Arthritis Res. Ther.*, 7(2):R310.

Chou, J., Chan, M. F., and Werb, Z. (2016). Metalloproteinases: a Functional Pathway for Myeloid Cells. *Microbiol. Spectr.*, 4(2).

Choy, E. (2012). Understanding the dynamics: pathways involved in the pathogenesis of rheumatoid arthritis. *Rheumatology*, 51(suppl 5):v3–v11.

Cohen, S., Hurd, E., Cush, J., Schiff, M., Weinblatt, M. E., Moreland, L. W., Kremer, J., Bear, M. B., Rich, W. J., and McCabe, D. (2002). Treatment of rheumatoid arthritis with anakinra, a recombinant human interleukin-1 receptor antagonist, in combination with methotrexate: Results of a twenty-four-week, multicenter, randomized, double-blind, placebo-controlled trial. *Arthritis Rheum.*, 46(3):614–624.

Corcoran, N. M., Hovens, C. M., Hong, M. K. H., Pedersen, J., Casey, R. G., Connolly, S., Peters, J., Harewood, L., Gleave, M. E., Goldenberg, S. L., and Costello, A. J. (2012). Underestimation of Gleason score at prostate biopsy refl ects sampling error in lower volume tumours. *BJU Int.*, 109(5):660–664.

Courtenay, J. S., Dallman, M. J., Dayan, A. D., Martin, A., and Mosedale, B. (1980). Immunisation against heterologous type II collagen induces arthritis in mice. *Nature*, 283(5748):666–8.

Crofford, L. J. (2013). Use of NSAIDs in treating patients with arthritis. *Arthritis Res. Ther.*, 15(Suppl 3):S2.

Da Silva, J. A. P., Jacobs, G., Kirwan, J. R., Boers, M., Saag, K. G., Inês, L. B. S., De Koning, E. J. P., Buttgereit, F., Cutolo, M., Capell, H., Rau, R., and Bijlsma, J. (2006). Safety of low dose glucocorticoid treatment in rheumatoid arthritis: published evidence and prospective trial data. *Ann Rheum Dis*, 65:285–293.

Dale, I., Fagerhol, M. K., and Naesgaard, I. (1983). Purification and Partial Characterization of a Highly Immunogenic Human Leukocyte Protein, the L1 Antigen. *Eur. J. Biochem.*, 134(1):1–6.

Diaspro, A., Chirico, G., Usai, C., Ramoino, P., and Dobrucki, J. (2006). *Photobleaching*. Springer, Boston, MA.

Duffy, M. J., Planas, O., Faust, A., Vogl, T., Hermann, S., Schäfers, M., Nonell, S., and Strassert, C. A. (2018). Towards optimized naphthalocyanines as sonochromes for photoacoustic imaging in vivo. *Photoacoustics*, 9:49–61.

Duncan, H. and Riddle, J. M. (1986). Juxtaarticular osteoporosis. *Arthritis Rheum.*, 29(1):149–150.

Edwards, J. C., Szczepański, L., Szechiński, J., Filipowicz-Sosnowska, A., Emery, P., Close, D. R., Stevens, R. M., and Shaw, T. (2004). Efficacy of B-Cell - Targeted Therapy with Rituximab in Patients with Rheumatoid Arthritis. *N. Engl. J. Med.*, 350(25):2572–2581.

Ehlermann, P., Eggers, K., Bierhaus, A., Most, P., Weichenhan, D., Greten, J., Nawroth, P. P., Katus, H. A., and Remppis, A. (2006). Increased proinflammatory endothelial response to S100A8/A9 after preactivation through advanced glycation end products. *Cardiovasc. Diabetol.*, 5(1):6.

Ehrchen, J. M., Sunderkötter, C., Foell, D., Vogl, T., and Roth, J. (2009). The endogenous Toll-like receptor 4 agonist S100A8/S100A9 (calprotectin) as innate amplifier of infection, autoimmunity, and cancer. *J. Leukoc. Biol.*, 86(3):557–66.

Fabris, M., De Vita, S., Blasone, N., Visentini, D., Pezzarini, E., Pontarini, E., Fabro, C., Quartuccio, L., Mazzolini, S., Curcio, F., and Tonutti, E. (2010). Serum levels of anti-CCP antibodies, anti-MCV antibodies and RF IgA in the follow-up of patients with rheumatoid arthritis treated with rituximab. *Autoimmun. Highlights*, 1(2):87–94.

Fassbender, H. G. (2002). *Pathology and Pathobiology of Rheumatic Diseases*. Springer Berlin Heidelberg.

Faust, A., Völler, T., Busch, F., Schäfers, M., Roth, J., Hermann, S., Vogl, T., Schober, O., Heindel, W., Schäfers, M., Bremer, C., Thuvesson, I., Björk, A., and Simon, D. I. (2015). Development and evaluation of a non-peptidic ligand for the molecular imaging of inflammatory processes using S100A9 (MRP14) as a novel target. *Chem. Commun.*, 51(86):15637–15640.

Faust, A., Waschkau, B., Waldeck, J., Höltke, C., Breyholz, H.-J., Wagner, S., Kopka, K., Heindel, W., Schäfers, M., and Bremer, C. (2008). Synthesis and Evaluation of a Novel Fluorescent Photoprobe for Imaging Matrix Metalloproteinases. *Bioconjug. Chem.*, 19(5):1001–1008.

Finnegan, A., Mikecz, K., Tao, P., and Glant, T. T. (1999). Proteoglycan (aggrecan)-induced arthritis in BALB/c mice is a Th1-type disease regulated by Th2 cytokines. *J. Immunol.*, 163(10):5383–90.

Fischer, T., Ebert, B., Voigt, J., Macdonald, R., Schneider, U., Thomas, A., Hamm, B., and Hermann, K.-G. A. (2010). Detection of Rheumatoid Arthritis Using Non-Specific Contrast Enhanced Fluorescence Imaging. *Acad. Radiol.*, 17(3):375–381.

Fishman, D. and Isenberg, D. A. (1997). Splenic involvement in rheumatic diseases. *Semin. Arthritis Rheum.*, 27(3):141–155.

Foell, D. and Roth, J. (2004). Proinflammatory S100 proteins in arthritis and autoimmune disease. *Arthritis Rheum.*, 50(12):3762–3771.

Frank-Bertoncelj, M., Trenkmann, M., Klein, K., Karouzakis, E., Rehrauer, H., Bratus, A., Kolling, C., Armaka, M., Filer, A., Michel, B. A., Gay, R. E., Buckley, C. D., Kollias, G., Gay, S., and Ospelt, C. (2017). Epigenetically-driven anatomical diversity of synovial fibroblasts guides joint-specific fibroblast functions. *Nat. Commun.*, 8:14852.

Fransen, J. and van Riel, P. L. (2009). The Disease Activity Score and the EULAR Response Criteria. *Rheum. Dis. Clin. North Am.*, 35(4):745–757.

Gabriel, S. E. (2001). The epidemiology of rheumatoid arthritis. *Rheum. Dis. Clin. North Am.*, 27(2):269–281.

Gearing, A. J., Beckett, P., Christodoulou, M., Churchill, M., Clements, J. M., Crimmin, M., Davidson, A. H., Drummond, A. H., Galloway, W. A., and Gilbert, R. (1995). Matrix metalloproteinases and processing of pro-TNF-alpha. *J. Leukoc. Biol.*, 57(5):774–7.

Gebhardt, C., Németh, J., Angel, P., and Hess, J. (2006). S100A8 and S100A9 in inflammation and cancer. *Biochem. Pharmacol.*, 72(11):1622–1631.

Geven, E. J. W., van den Bosch, M. H. J., Di Ceglie, I., Ascone, G., Abdollahi-Roodsaz, S., Sloetjes, A. W., Hermann, S., Schäfers, M., van de Loo, F. A. J., van der Kraan, P. M., Koenders, M. I., Foell, D., Roth, J., Vogl, T., and van Lent, P. L. E. M. (2016). S100A8/A9, a potent serum and molecular imaging biomarker for synovial inflammation and joint destruction in seronegative experimental arthritis. *Arthritis Res. {&} Ther.*, 18(1):247.

Giacomini, G., Miranda, J. R. A., Pavan, A. L. M., Duarte, S. B., Ribeiro, S. M., Pereira, P. C. M., Alves, A. F. F., de Oliveira, M., and Pina, D. R. (2015). Quantification of Pulmonary Inflammatory Processes Using Chest Radiography: Tuberculosis as the Motivating Application. *Medicine (Baltimore).*, 94(26):e1044.

Gibson, A. and Dehghani, H. (2009). Diffuse optical imaging. *Philos. Trans. A. Math. Phys. Eng. Sci.*, 367(1900):3055–72.

Glimm, A.-M., Werner, S. G., Burmester, G. R., Backhaus, M., and Ohrndorf, S. (2016). Analysis of distribution and severity of inflammation in patients with osteoarthitis compared to rheumatoid arthritis by ICG-enhanced fluorescence optical imaging and musculoskeletal ultrasound: a pilot study. *Ann. Rheum. Dis.*, 75(3):566 LP – 570.

Gompels, L. L., Madden, L., Lim, N. H., Inglis, J. J., McConnell, E., Vincent, T. L., Haskard, D. O., and Paleolog, E. M. (2011). In vivo fluorescence imaging of E-selectin: Quantitative detection of endothelial activation in a mouse model of arthritis. *Arthritis Rheum.*, 63(1):107–117.

Goronzy, J. J. and Weyand, C. M. (2001). *Rheumatoid arthritis*. Karger.

Graves, E., Weissleder, R., and Ntziachristos, V. (2004). Fluorescence Molecular Imaging of Small Animal Tumor Models. *Curr. Mol. Med.*, 4(4):419–430.

Griffiths, H. J. (1989). Tissue Substitutes in Radiation Dosimetry and Measurement. No. 4. *Radiology*, 173(1):202–202.

Guy, C. and Ffytche, D. (2005). *An introduction to the principles of medical imaging*. Imperial College Press.

Hansch, A., Frey, O., Sauner, D., Hilger, I., Haas, M., Malich, A., Bräuer, R., and Kaiser, W. A. (2004). In vivo imaging of experimental arthritis with near-infrared fluorescence. *Arthritis Rheum.*, 50(3):961–967.

Hashimoto, G., Inoki, I., Fujii, Y., Aoki, T., Ikeda, E., and Okada, Y. (2002). Matrix metalloproteinases cleave connective tissue growth factor and reactivate angiogenic activity of vascular endothelial growth factor 165. *J. Biol. Chem.*, 277(39):36288–95.

Hegen, M., Keith, J. C., Collins, M., and Nickerson-Nutter, C. L. (2008). Utility of animal models for identification of potential therapeutics for rheumatoid arthritis. *Ann. Rheum. Dis.*, 67(11):1505–1515.

Henke, M. O., Renner, A., Rubin, B. K., Gyves, J. I., Lorenz, E., and Koo, J. S. (2006). Upregulation of S100A8 and S100A9 Protein in Bronchial Epithelial Cells by Lipopolysaccharide. *Exp. Lung Res.*, 32(8):331–347.

Hessian, P. A., Edgeworth, J., and Hogg, N. (1993). MRP-8 and MRP-14, two abundant Ca(2+)-binding proteins of neutrophils and monocytes. *J. Leukoc. Biol.*, 53(2):197–204.

Hodgson, R. J., O'Connor, P., and Moots, R. (2008). MRI of rheumatoid arthritis image quantitation for the assessment of disease activity, progression and response to therapy. *Rheumatology*, 47(1):13–21.

Hsiao, T.-C., De-Yi Chiu, Chung, R.-J., Ming Chao, Yi-Hsuan Lee, Meng-Ju Li, and Meng-Lin Li (2013). Enhanced photoacoustic detection of calcifications with molecular targeting: Feasibility study. In *2013 IEEE Int. Ultrason. Symp.*, pages 1525–1527. IEEE.

Huang, B., Bates, M., and Zhuang, X. (2009). Super-resolution fluorescence microscopy. *Annu. Rev. Biochem.*, 78:993–1016.

Huang, R., Vider, J., Kovar, J. L., Olive, D. M., Mellinghoff, I. K., Mayer-Kuckuk, P., Kircher, M. F., and Blasberg, R. G. (2012). Integrin $\alpha v\beta 3$-targeted IRDye 800CW near-infrared imaging of glioblastoma. *Clin. Cancer Res.*, 18(20):5731–40.

Imai, Y., Sato, T., Yamakawa, M., Kasajima, T., Suda, A., and Watanabe, Y. (1989). A morphological and immunohistochemical study of lymphoid germinal centers in synovial and lymph node tissues from rheumatoid arthritis patients with special reference to complement components and their receptors. *Acta Pathol. Jpn.*, 39(2):127–34.

Itou, H., Yao, M., Fujita, I., Watanabe, N., Suzuki, M., Nishihira, J., and Tanaka, I. (2002). The crystal structure of human MRP14 (S100A9), a Ca2+-dependent regulator protein in inflammatory process. *J. Mol. Biol.*, 316(2):265–276.

Jacquemin, C., Molto, A., Servy, H., Sellam, J., Foltz, V., Gandjbakhch, F., Hudry, C., Mitrovic, S., Granger, B., Fautrel, B., and Gossec, L. (2017). Flares assessed weekly in patients with rheumatoid arthritis or axial spondyloarthritis and relationship with physical activity measured using a connected activity tracker: a 3-month study. *RMD Open*, 3(1):e000434.

Janker, R. (2013). *Röntgen-Aufnahmetechnik : Teil I: Allgemeine Grundlagen und Einstellungen.* Springer Berlin Heidelberg.

Jonak, C., Skvara, H., Kunstfeld, R., Trautinger, F., and Schmid, J. A. (2011). Intradermal Indocyanine Green for In Vivo Fluorescence Laser Scanning Microscopy of Human Skin: A Pilot Study. *PLoS One*, 6(8):e23972.

Kane, D., Balint, P. V., and Sturrock, R. D. (2003). Ultrasonography is superior to clinical examination in the detection and localization of knee joint effusion in rheumatoid arthritis. *J. Rheumatol.*, 30(5):966–71.

Keffer, J., Probert, L., Cazlaris, H., Georgopoulos, S., Kaslaris, E., Kioussis, D., and Kollias, G. (1991). Transgenic mice expressing human tumour necrosis factor: a predictive genetic model of arthritis. *EMBO J.*, 10(13):4025–31.

Keystone, E. C., Schorlemmer, H. U., Pope, C., and Allison, A. C. (1977). Zymosan-induced arthritis: a model of chronic proliferative arthritis following activation of the alternative pathway of complement. *Arthritis Rheum.*, 20(7):1396–1401.

Kiessling, F., Pichler, B. J., and Hauff, P. (2017). *Small animal imaging : basics and practical guide.* Springer.

Kim, C., Favazza, C., and Wang, L. V. (2010). In vivo photoacoustic tomography of chemicals: high-resolution functional and molecular optical imaging at new depths. *Chem. Rev.*, 110(5):2756–82.

Kim, J. Y., Choi, Y. Y., Kim, C. W., Sung, Y.-K., and Yoo, D.-H. (2016). Bone Scintigraphy in the Diagnosis of Rheumatoid Arthritis: Is There Additional Value of Bone Scintigraphy with Blood Pool Phase over Conventional Bone Scintigraphy? *J. Korean Med. Sci.*, 31(4):502–9.

Kim, K. S., Choi, H. M., Lee, Y.-A., Choi, I. A., Lee, S.-H., Hong, S.-J., Yang, H.-I., and Yoo, M. C. (2011). Expression levels and association of gelatinases MMP-2 and MMP-9 and collagenases MMP-1 and MMP-13 with VEGF in synovial fluid of patients with arthritis. *Rheumatol. Int.*, 31(4):543–547.

Kłak, A., Paradowska-Gorycka, A., Kwiatkowska, B., and Raciborski, F. (2016). Personalized medicine in rheumatology. *Reumatologia*, 54(4):177–186.

Klein, T. and Bischoff, R. (2011). Physiology and pathophysiology of matrix metalloproteases. *Amino Acids*, 41(2):271–90.

Koga, T., Kakimoto, K., Hirofuji, T., Kotani, S., Ohkuni, H., Watanabe, K., Okada, N., Okada, H., Sumiyoshi, A., and Saisho, K. (1985). Acute joint inflammation in mice after systemic injection of the cell wall, its peptidoglycan, and chemically defined peptidoglycan subunits from various bacteria. *Infect. Immun.*, 50(1):27–34.

Kollias, G., Papadaki, P., Apparailly, F., Vervoordeldonk, M. J., Holmdahl, R., Baumans, V., Desaintes, C., Di Santo, J., Distler, J., Garside, P., Hegen, M., Huizinga, T. W. J., Jüngel, A., Klareskog, L., McInnes, I., Ragoussis, I., Schett, G., Hart, B. t., Tak, P. P., Toes, R., van den Berg, W., Wurst, W., and Gay, S. (2011). Animal models for arthritis: innovative tools for prevention and treatment. *Ann. Rheum. Dis.*, 70(8):1357–62.

Korb, M. L., Warram, J. M., Grudzinski, J., Weichert, J., Jeffery, J., and Rosenthal, E. L. (2014). Breast cancer imaging using the near-infrared fluorescent agent, CLR1502. *Mol. Imaging*, 13.

Korndörfer, I. P., Brueckner, F., and Skerra, A. (2007). The Crystal Structure of the Human (S100A8/S100A9)2 Heterotetramer, Calprotectin, Illustrates how Conformational Changes of Interacting α-Helices Can Determine Specific Association of Two EF-hand Proteins. *J. Mol. Biol.*, 370(5):887–898.

Kosaka, N., Ogawa, M., Choyke, P. L., and Kobayashi, H. (2009). Clinical implications of near-infrared fluorescence imaging in cancer. *Future Oncol.*, 5(9):1501–11.

Kremer, J. M., Rynes, R. I., and Bartholomew, L. E. (1987). Severe flare of rheumatoid arthritis after discontinuation of long-term methotrexate therapy. Double-blind study. *Am. J. Med.*, 82(4):781–6.

Kremer, J. M., Westhovens, R., Leon, M., Di Giorgio, E., Alten, R., Steinfeld, S., Russell, A., Dougados, M., Emery, P., Nuamah, I. F., Williams, G. R., Becker, J.-C., Hagerty, D. T., and Moreland, L. W. (2003). Treatment of Rheumatoid Arthritis by Selective Inhibition of T-Cell Activation with Fusion Protein CTLA4Ig. *N. Engl. J. Med.*, 349(20):1907–1915.

Krohn, M., Ohrndorf, S., Werner, S. G., Schicke, B., Burmester, G.-R., Hamm, B., Backhaus, M., and Hermann, K.-G. A. (2015). Near-infrared Fluorescence Optical Imaging in Early Rheumatoid Arthritis: A Comparison to Magnetic Resonance Imaging and Ultrasonography. *J. Rheumatol.*, 42(7).

Kumar, G. and Santhosh, C. (2003). Spectral studies and radiative characteristics of naphthalocyanine molecules in DMF. *Mater. Lett.*, 57(15):2315–2319.

Kwon, C. H., Moon, H. J., Park, H. J., Choi, J. H., and Park, D. Y. (2013). S100A8 and S100A9 promotes invasion and migration through p38 mitogen-activated protein kinase-dependent NF-κB activation in gastric cancer cells. *Mol. Cells*, 35(3):226–234.

Lashkari, M., Noori, A., Hajiimanouchehri, F., Oveisi, S., and Kazemifar, A. M. (2014). Determination of specificity and sensitivity of anti-RA 33 in diagnosis of early rheumatoid arthritis. *Glob. J. Health Sci.*, 6(4):292–7.

Laufer, J., Zhang, E., and Beard, P. (2010). Evaluation of Absorbing Chromophores Used in Tissue Phantoms for Quantitative Photoacoustic Spectroscopy and Imaging. *IEEE J. Sel. Top. Quantum Electron.*, 16(3):600–607.

Leblond, F., Davis, S. C., Valdés, P. A., and Pogue, B. W. (2010). Pre-clinical whole-body fluorescence imaging: Review of instruments, methods and applications. *J. Photochem. Photobiol. B.*, 98(1):77–94.

Leclerc, E., Fritz, G., Vetter, S. W., and Heizmann, C. W. (2009). Binding of S100 proteins to RAGE: An update. *Biochim. Biophys. Acta - Mol. Cell Res.*, 1793(6):993–1007.

Lee, D.-G., Woo, J.-W., Kwok, S.-K., Cho, M.-L., and Park, S.-H. (2013). MRP8 promotes Th17 differentiation via upregulation of IL-6 production by fibroblast-like synoviocytes in rheumatoid arthritis. *Exp. Mol. Med.*, 45(4):e20.

Lee, D. M. and Weinblatt, M. E. (2001). Rheumatoid arthritis. *Lancet*, 358(9285):903–911.

Lee, J.-A., Kim, M.-K., Paek, H.-J., Kim, Y.-R., Kim, M.-K., Lee, J.-K., Jeong, J., and Choi, S.-J. (2014). Tissue distribution and excretion kinetics of orally administered silica nanoparticles in rats. *Int. J. Nanomedicine*, 9 Suppl 2(Suppl 2):251–60.

Lee, S., Xie, J., and Chen, X. (2010). Activatable molecular probes for cancer imaging. *Curr. Top. Med. Chem.*, 10(11):1135–44.

Lent, P. L., Grevers, L., Blom, A. B., Sloetjes, A., Mort, J. S., Vogl, T., Nacken, W., Berg, W. B., and Roth, J. (2008a). Myeloid-related proteins S100A8/S100A9 regulate joint inflammation and cartilage destruction during antigen-induced arthritis. *Ann Rheum Dis*, 67.

Lent, P. L., Grevers, L. C., Blom, A. B., Arntz, O. J., Loo, F. A., Kraan, P., Abdollahi-Roodsaz, S., Srikrishna, G., Freeze, H., and Sloetjes, A. (2008b). Stimulation of chondrocyte-mediated cartilage destruction by S100A8 in experimental murine arthritis. *Arthritis Rheum*, 58.

Leukert, N., Sorg, C., and Roth, J. (2005). Molecular basis of the complex formation between the two calcium-binding proteins S100A8 (MRP8) and S100A9 (MRP14). *Biol. Chem.*, 386(5):429–34.

Leukert, N., Vogl, T., Strupat, K., Reichelt, R., Sorg, C., and Roth, J. (2006). Calcium-dependent Tetramer Formation of S100A8 and S100A9 is Essential for Biological Activity. *J. Mol. Biol.*, 359(4):961–972.

Li, C., Zhang, C., Gao, L., Garcia-Uribe, A., and Wang, L. V. (2013). Photoacoustic recovery after photothermal bleaching in living cells. *J. Biomed. Opt.*, 18(10):106004.

Li, Z., Li, H., Chen, H., and Xie, W. (2010). In vivo determination of time-dependent acute myocardial ischemia based on photoacoustic imaging. In *2010 Photonics Glob. Conf.*, pages 1–4. IEEE.

Loffek, S., Schilling, O., and Franzke, C.-W. (2011). Biological role of matrix metalloproteinases: a critical balance. *Eur. Respir. J.*, 38(1):191–208.

MacGregor, A. J., Snieder, H., Rigby, A. S., Koskenvuo, M., Kaprio, J., Aho, K., and Silman, A. J. (2000). Characterizing the quantitative genetic contribution to rheumatoid arthritis using data from twins. *Arthritis Rheum.*, 43(1):30–37.

Maini, R. N., Taylor, P. C., Szechinski, J., Pavelka, K., Bröll, J., Balint, G., Emery, P., Raemen, F., Petersen, J., Smolen, J., Thomson, D., Kishimoto, T., and CHARISMA Study Group (2006). Double-blind randomized controlled clinical trial of the interleukin-6 receptor antagonist, tocilizumab, in European patients with rheumatoid arthritis who had an incomplete response to methotrexate. *Arthritis Rheum.*, 54(9):2817–2829.

Mait, J. N. (2006). A History of Imaging: Revisiting the Past to Chart the Future. *Opt. Photonics News*, 17(2):22.

Majithia, V. and Geraci, S. A. (2007). Rheumatoid Arthritis: Diagnosis and Management. *Am. J. Med.*, 120(11):936–939.

Malemud, C. J. (2006). Matrix metalloproteinases (MMPs) in health and disease: an overview. *Front. Biosci.*, 11:1696–701.

Maradit-Kremers, H., Nicola, P. J., Crowson, C. S., Ballman, K. V., and Gabriel, S. E. (2005). Cardiovascular death in rheumatoid arthritis: A population-based study. *Arthritis Rheum.*, 52(3):722–732.

Markowitz, J. and Carson, W. E. (2013). Review of S100A9 biology and its role in cancer. *Biochim. Biophys. Acta - Rev. Cancer*, 1835(1):100–109.

Marshall, M. V., Rasmussen, J. C., Tan, I.-C., Aldrich, M. B., Adams, K. E., Wang, X., Fife, C. E., Maus, E. A., Smith, L. A., and Sevick-Muraca, E. M. (2010). Near-Infrared Fluorescence Imaging in Humans with Indocyanine Green: A Review and Update. *Open Surg. Oncol. J.*, 2(2):12–25.

Martelli, C., Dico, A. L., Diceglie, C., Lucignani, G., Ottobrini, L., Martelli, C., Lo Dico, A., Diceglie, C., Lucignani, G., and Ottobrini, L. (2016). Optical imaging probes in oncology. *Oncotarget*, 7(30):48753–48787.

McInnes, I. B. and Schett, G. (2011). The Pathogenesis of Rheumatoid Arthritis. *N. Engl. J. Med.*, 365(23):2205–2219.

McInnes, I. B. and Schett, G. (2017). Pathogenetic insights from the treatment of rheumatoid arthritis. *Lancet*, 389(10086):2328–2337.

McIntyre, J. O., Fingleton, B., Wells, K. S., Piston, D. W., Lynch, C. C., Gautam, S., and Matrisian, L. M. (2004). Development of a novel fluorogenic proteolytic beacon for in vivo detection and imaging of tumour-associated matrix metalloproteinase-7 activity. *Biochem. J.*, 377(Pt 3):617–28.

Meikle, S. R., Kench, P., Kassiou, M., and Banati, R. B. (2005). Small animal SPECT and its place in the matrix of molecular imaging technologies. *Phys. Med. Biol.*, 50(22):R45–R61.

Mélet, J., Mulleman, D., Goupille, P., Ribourtout, B., Watier, H., and Thibault, G. (2013). Rituximab-Induced T Cell Depletion in Patients With Rheumatoid Arthritis: Association With Clinical Response. *Arthritis Rheum.*, 65(11):2783–2790.

Michaud, K. and Wolfe, F. (2007). Comorbidities in rheumatoid arthritis. *Best Pract. Res. Clin. Rheumatol.*, 21(5):885–906.

Michl, J. (2006). *Photophysics of Organic Molecules in Solution*. Taylor & Francis Group. LLC.

Mohammed, F. F., Smookler, D. S., and Khokha, R. (2003). Metalloproteinases, inflammation, and rheumatoid arthritis. *Ann. Rheum. Dis.*, 62(Suppl 2):ii43–ii47.

Monici, M. (2005). Cell and tissue autofluorescence research and diagnostic applications. *Biotechnol. Annu. Rev.*, 11:227–256.

Montalti, M., Credi, A., Prodi, L., Gandolfi, M. T., Michl, J., and Balzani, V. (2006). *Handbook of photochemistry*. CRC Press.

Mor, A., Abramson, S. B., and Pillinger, M. H. (2005). The fibroblast-like synovial cell in rheumatoid arthritis: a key player in inflammation and joint destruction. *Clin. Immunol.*, 115(2):118–128.

Mulholland, M. W. and Doherty, G. M. (2006). *Complications in surgery*. Lippincott Williams & Wilkins.

Murphy, G. and Nagase, H. (2008). Reappraising metalloproteinases in rheumatoid arthritis and osteoarthritis: destruction or repair? *Nat. Clin. Pract. Rheumatol.*, 4(3):128–135.

Nagase, H., Visse, R., Murphy, G., Cooper, D., Werb, Z., and Holden, J. (2006). Structure and function of matrix metalloproteinases and TIMPs. *Cardiovasc. Res.*, 69(3):562–573.

Niewold, T., Harrison, M., and Paget, S. (2007). Anti-CCP antibody testing as a diagnostic and prognostic tool in rheumatoid arthritis. *QJM*, 100(4):193–201.

Ntziachristos, V. (2006). Fluorescence Molecular Imaging. *Annu. Rev. Biomed. Eng.*, 8:1–33.

Ntziachristos, V., Bremer, C., and Weissleder, R. (2003). Fluorescence imaging with near-infrared light: new technological advances that enable in vivo molecular imaging. *Eur Radiol*, 13:195–208.

Ntziachristos, V. and Razansky, D. (2010). Molecular Imaging by Means of Multispectral Optoacoustic Tomography (MSOT). *Chem. Rev.*, 110(5):2783–2794.

Nuki, G., Bresnihan, B., Bear, M. B., McCabe, D., and European Group Of Clinical Investigators (2002). Long-term safety and maintenance of clinical improvement following treatment with anakinra (recombinant human interleukin-1 receptor antagonist) in patients with rheumatoid arthritis: Extension phase of a randomized, double-blind, placebo-controlled trial. *Arthritis Rheum.*, 46(11):2838–2846.

Odink, K., Cerletti, N., Brüggen, J., Clerc, R. G., Tarcsay, L., Zwadlo, G., Gerhards, G., Schlegel, R., and Sorg, C. (1987). Two calcium-binding proteins in infiltrate macrophages of rheumatoid arthritis. *Nature*, 330(6143):80–82.

Ohnishi, S., Lomnes, S. J., Laurence, R. G., Gogbashian, A., Mariani, G., and Frangioni, J. V. (2005). Organic alternatives to quantum dots for intraoperative near-infrared fluorescent sentinel lymph node mapping. *Mol. Imaging*, 4(3):172–81.

Östör, A. J. K. (2008). Abatacept: a T-cell co-stimulation modulator for the treatment of rheumatoid arthritis. *Clin. Rheumatol.*, 27(11):1343–1353.

Paavonen, K., Mandelin, J., Partanen, T., Jussila, L., Li, T.-F., Ristimaki, A., Alitalo, K., and Konttinen, Y. T. (2002). Vascular endothelial growth factors C and D and their VEGFR-2 and 3 receptors in blood and lymphatic vessels in healthy and arthritic synovium. *J. Rheumatol.*, 29(1).

Parsons, J. R. (1998). Cartilage. In *Handb. Biomater. Prop.*, pages 40–47. Springer US, Boston, MA.

Patil, P. and Dasgupta, B. (2012). Role of diagnostic ultrasound in the assessment of musculoskeletal diseases. *Ther. Adv. Musculoskelet. Dis.*, 4(5):341–55.

Pearson, C. M. (1956). Development of arthritis, periarthritis and periostitis in rats given adjuvants. *Proc. Soc. Exp. Biol. Med.*, 91(1):95–101.

Pogue, B. W. (2015). Optics in the Molecular Imaging Race. *Opt. Photonics News*, 26(9):24.

Pruenster, M., Kurz, A. R. M., Chung, K.-J., Cao-Ehlker, X., Bieber, S., Nussbaum, C. F., Bierschenk, S., Eggersmann, T. K., Rohwedder, I., Heinig, K., Immler, R., Moser, M., Koedel, U., Gran, S., McEver, R. P., Vestweber, D., Verschoor, A., Leanderson, T., Chavakis, T., Roth, J., Vogl, T., and Sperandio, M. (2015). Extracellular MRP8/14 is a regulator of β2 integrin-dependent neutrophil slow rolling and adhesion. *Nat. Commun.*, 6:6915.

Puchner, R. (2012). *Rheumatologie aus der Praxis : Ein Kurzlehrbuch der entzündlichen Gelenkerkrankungen mit Fallbeispielen.* Springer.

Put, S., Westhovens, R., Lahoutte, T., and Matthys, P. (2014). Molecular imaging of rheumatoid arthritis: emerging markers, tools, and techniques. *Arthritis Res. Ther.*, 16(2):208.

Qu, Z., Garcia, C. H., O'Rourke, L. M., Planck, S. R., Kohli, M., and Rosenbaum, J. T. (1994). Local proliferation of fibroblast-like synoviocytes contributes to synovial hyperplasia. Results of proliferating cell nuclear antigen/cyclin, c-myc, and nucleolar organizer region staining. *Arthritis Rheum.*, 37(2):212–20.

Quaranta, M., Borisov, S. M., and Klimant, I. (2012). Indicators for optical oxygen sensors. *Bioanal. Rev.*, 4(2-4):115–157.

Ra, H., González-González, E., Uddin, M. J., King, B. L., Lee, A., Ali-Khan, I., Marnett, L. J., Tang, J. Y., and Contag, C. H. (2015). Detection of Non-Melanoma Skin Cancer by in vivo Fluorescence Imaging with Fluorocoxib A. *Neoplasia*, 17(2):201–207.

Rammes, A., Roth, J., Goebeler, M., Klempt, M., Hartmann, M., and Sorg, C. (1997). Myeloid-related protein (MRP) 8 and MRP14, calcium-binding proteins of the S100 family, are secreted by activated monocytes via a novel, tubulin-dependent pathway. *J. Biol. Chem.*, 272(14):9496–502.

Razansky, D., Distel, M., Vinegoni, C., Ma, R., Perrimon, N., Köster, R. W., and Ntziachristos, V. (2009). Multispectral opto-acoustic tomography of deep-seated fluorescent proteins in vivo. *Nat. Photonics*, 3(7):412–417.

Razavian, M., Bordenave, T., Georgiadis, D., Beau, F., Zhang, J., Golestani, R., Toczek, J., Jung, J.-J., Ye, Y., Kim, H.-Y., Han, J., Dive, V., Devel, L., and Sadeghi, M. M. (2016). Optical imaging of MMP-12 active form in inflammation and aneurysm. *Sci. Rep.*, 6(1):38345.

Rengel, Y., Ospelt, C., and Gay, S. (2007). Proteinases in the joint: clinical relevance of proteinases in joint destruction. *Arthritis Res. Ther.*, 9(5):221.

Reparon-Schuijt, C. C., van Esch, W. J. E., van Kooten, C., Schellekens, G. A., de Jong, B. A. W., van Venrooij, W. J., Breedveld, F. C., and Verweij, C. L. (2001). Secretion of anti-citrulline-containing peptide antibody by B lymphocytes in rheumatoid arthritis. *Arthritis Rheum.*, 44(1):41–47.

Riva, M., Kallberg, E., Bjork, P., Hancz, D., Vogl, T., Roth, J., Ivars, F., and Leanderson, T. (2012). Induction of nuclear factor-kappaB responses by the S100A9 protein is Toll-like receptor-4-dependent. *Immunology*, 137.

Rogers, M. P., Trentham, D. E., Dynesius-Trentham, R., Daffner, K., and Reich, P. (1983). Exacerbation of collagen arthritis by noise stress. *J. Rheumatol.*, 10(4):651–4.

Rogers, M. P., Trentham, D. E., McCune, W. J., Ginsberg, B. I., Reich, P., and David, J. R. (1979). Abrogation of type II collagen-induced arthritis in rats by psychological stress. *Trans. Assoc. Am. Physicians*, 92:218–28.

Rose, B. J. and Kooyman, D. L. (2016). A Tale of Two Joints: The Role of Matrix Metalloproteases in Cartilage Biology. *Dis. Markers*, 2016:4895050.

Roth, J., Burwinkel, F., van den Bos, C., Goebeler, M., Vollmer, E., and Sorg, C. (1993). MRP8 and MRP14, S-100-like proteins associated with myeloid differentiation, are translocated to plasma membrane and intermediate filaments in a calcium-dependent manner. *Blood*, 82(6):1875–83.

Saboury, B., Salavati, A., Brothers, A., Basu, S., Kwee, T. C., Lam, M. G. E. H., Hustinx, R., Louis, E., Torigian, D. A., and Alavi, A. (2014). FDG PET/CT in Crohn's disease: correlation of quantitative FDG PET/CT parameters with clinical and endoscopic surrogate markers of disease activity. *Eur. J. Nucl. Med. Mol. Imaging*, 41(4):605–614.

Sadikot, R. T. and Blackwell, T. S. (2005). Bioluminescence imaging. *Proc. Am. Thorac. Soc.*, 2(6):537–40, 511–2.

Saleem, B., Brown, A. K., Quinn, M., Karim, Z., Hensor, E. M. A., Conaghan, P., Peterfy, C., Wakefield, R. J., and Emery, P. (2012). Can flare be predicted in DMARD treated RA patients in remission, and is it important? A cohort study. *Ann. Rheum. Dis.*, 71(8):1316–21.

Sauer, M., Hofkens, J., and Enderlein, J. (2011). Basic Principles of Fluorescence Spectroscopy. In *Handb. Fluoresc. Spectrosc. Imaging*, pages 1–30. Wiley-VCH Verlag GmbH & Co. KGaA, Weinheim, Germany.

Scales, H. E., Ierna, M., Smith, K. M., Ross, K., Meiklejohn, G. R., Patterson-Kane, J. C., McInnes, I. B., Brewer, J. M., Garside, P., and Maffia, P. (2015). Assessment of murine collagen-induced arthritis by longitudinal non-invasive duplexed molecular optical imaging. *Rheumatology*, 7(3):kev361.

Schelbergen, R. F., Blom, A. B., Bosch, M. H., Sloetjes, A., Abdollahi-Roodsaz, S., Schreurs, B. W., Mort, J. S., Vogl, T., Roth, J., and Berg, W. B. (2012). Alarmins S100A8 and S100A9 elicit a catabolic effect in human osteoarthritic chondrocytes that is dependent on Toll-like receptor 4. *Arthritis Rheum*, 64.

Schelbergen, R. F. P., van Lent, P. L. E. M., Blom, A. B., Sloetjes, A., Vogl, T., Roth, J., and van den Berg, W. B. (2010). Alarmins S100A8 AND S100A9 skew chondrocytes towards a cartilage breakdown phenotype. *Ann. Rheum. Dis.*, 69(Suppl 2):A44–A44.

Scherer, R. L., McIntyre, J. O., and Matrisian, L. M. (2008). Imaging matrix metalloproteinases in cancer. *Cancer Metastasis Rev.*, 27(4):679–690.

Schett, G. (2007). Cells of the synovium in rheumatoid arthritis. Osteoclasts. *Arthritis Res. Ther.*, 9(1):203.

Schols, R. M., Connell, N. J., and Stassen, L. P. S. (2015). Near-Infrared Fluorescence Imaging for Real-Time Intraoperative Anatomical Guidance in Minimally Invasive Surgery: A Systematic Review of the Literature. *World J. Surg.*, 39(5):1069–1079.

Schulz, R. B. and Semmler, W. (2008). Fundamentals of Optical Imaging. In *Handb. Exp. Pharmacol.*, chapter 1, pages 3–22. Springer.

Schurgers, E., Mertens, F., Vanoirbeek, J. A. J., Put, S., Mitera, T., De Langhe, E., Billiau, A., Hoet, P. H. M., Nemery, B., Verbeken, E., and Matthys, P. (2012). Pulmonary inflammation in mice with collagen-induced arthritis is conditioned by complete Freund's adjuvant and regulated by endogenous IFN-γ. *Eur. J. Immunol*, 42:3223–3234.

Scott, D. L. and Houssien, D. A. (1996). Joint Assessment in Rheumatoid Arthritis. *Rheumatology*, 35(suppl 2):14–18.

Shepherd, C., Goyette, J., Utter, V., Rahimi, F., Yang, Z., Geczy, C., and Halliday, G. (2006). Inflammatory S100A9 and S100A12 proteins in Alzheimer's disease. *Neurobiol. Aging*, 27(11):1554–1563.

Shi, L. and Alfano, R. R. (2017). *Deep imaging in tissue and biomedical materials : using linear and nonlinear optical methods*. Pan Stanford Publishing.

Shiozawa, S., Tsumiyama, K., Yoshida, K., and Hashiramoto, A. (2011). Pathogenesis of Joint Destruction in Rheumatoid Arthritis. *Arch. Immunol. Ther. Exp. (Warsz).*, 59(2):89–95.

Shoenfeld, Y. and Meroni, P.-L. (2012). *The general practice guide to autoimmune diseases*. Pabst Science Publishers.

Silman, A. J., Pearson, J. E., Cook, N., Manson, J., Buring, J., Hennekens, C., Bennett, P., Ollier, B., Silman, A., John, S., Worthington, J., Davison, J., Bamber, S., Silman, A., Tran, T., Delaye, A., Prince, N., Lefevre, C., Thomas, G., Poirier, M., Soubigou, S., Alibert, O., Lasbleiz, S., Fouix, S., Bouchier, C., Liote, F., Loste, M., Lepage, V., Charron, D., Gyapay, G., Lopes-Vaz, A., Kuntz,

D., Bardin, T., and Weissenbach, J. (2002). Epidemiology and genetics of rheumatoid arthritis. *Arthritis Res. Ther.*, 42(Suppl):910–917.

Singh, J. A., Saag, K. G., Louis Bridges, S. J., Akl, E. A., Bannuru, R. R., Sullivan, M. C., Vaysbrot, E., Mcnaughton, C., Osani, M., Shmerling, R. H., Curtis, J. R., Furst, D. E., Parks, D., Kavanaugh, A., King, C., Leong, A., Matteson, E. L., Schousboe, J. T., Louis Bridges Jr, S., Israel, B., Clinic, M., Drevlow, B., Grober, J., and William StClair, E. (2015). 2015 American College of Rheumatology Guideline for the Treatment of Rheumatoid Arthritis. *Arthritis Care Res. (Hoboken).*

Smolen, J. S., Aletaha, D., and McInnes, I. B. (2016). Rheumatoid arthritis. *Lancet*, 388(10055):2023–2038.

Smolen, J. S., Beaulieu, A., Rubbert-Roth, A., Ramos-Remus, C., Rovensky, J., Alecock, E., Woodworth, T., Alten, R., and OPTION Investigators (2008). Effect of interleukin-6 receptor inhibition with tocilizumab in patients with rheumatoid arthritis (OPTION study): a double-blind, placebo-controlled, randomised trial. *Lancet*, 371(9617):987–997.

Sokka, T. and Pincus, T. (2005). Quantitative joint assessment in rheumatoid arthritis. *Clin. Exp. Rheumatol.*, 23(5 Suppl 39):S58–62.

Song, Y. W. and Kang, E. H. (2010). Autoantibodies in rheumatoid arthritis: rheumatoid factors and anticitrullinated protein antibodies. *QJM*, 103(3):139–46.

Srikrishna, G., Panneerselvam, K., Westphal, V., Abraham, V., Varki, A., and Freeze, H. H. (2001). Two proteins modulating transendothelial migration of leukocytes recognize novel carboxylated glycans on endothelial cells. *J. Immunol.*, 166(7):4678–88.

St. Clair, E. W., van der Heijde, D. M. F. M., Smolen, J. S., Maini, R. N., Bathon, J. M., Emery, P., Keystone, E., Schiff, M., Kalden, J. R., Wang, B., DeWoody, K., Weiss, R., Baker, D., and Active-Controlled Study of Patients Receiving Infliximab for the Treatment of Rheumatoid Arthritis of Early Onset Study Group (2004). Combination of infliximab and methotrexate therapy for early rheumatoid arthritis: A randomized, controlled trial. *Arthritis Rheum.*, 50(11):3432–3443.

Steenvoorden, M. M. C., Toes, R. E. M., Ronday, H. K., Huizinga, T. W. J., and Degroot, J. (2007). RAGE activation induces invasiveness of RA fibroblast-like synoviocytes in vitro. *Clin. Exp. Rheumatol.*, 25(5):740–2.

Stephens, D. J. and Allan, V. J. (2003). Light microscopy techniques for live cell imaging. *Science*, 300(5616):82–6.

Stuker, F., Ripoll, J., and Rudin, M. (2011). Fluorescence Molecular Tomography: Principles and Potential for Pharmaceutical Research. *Pharmaceutics*, 3:229–274.

Sunahori, K., Yamamura, M., Yamana, J., Takasugi, K., Kawashima, M., Yamamoto, H., Chazin, W. J., Nakatani, Y., Yui, S., and Makino, H. (2006). The S100A8/A9 heterodimer amplifies proinflammatory cytokine production by macrophages via activation of nuclear factor kappa B and p38 mitogen-activated protein kinase in rheumatoid arthritis. *Arthritis Res. Ther.*, 8(3):R69.

Suryono, J.-i., Kido, J.-i., Hayashi, N., Kataoka, M., and Nagata, T. (2005). Calprotectin Expression in Human Monocytes: Induction by Porphyromonas gingivalis Lipopolysaccharide, Tumor Necrosis Factor-α, and Interleukin-1β. *J. Periodontol.*, 76(3):437–442.

Szekanecz, Z., Besenyei, T., Paragh, G., and Koch, A. E. (2009). Angiogenesis in rheumatoid arthritis. *Autoimmunity*, 42(7):563–73.

Taylor, P. C. and Feldmann, M. (2009). Anti-TNF biologic agents: still the therapy of choice for rheumatoid arthritis. *Nat. Rev. Rheumatol.*, 5(10):578–582.

Tchetverikov, I., Verzijl, N., Huizinga, T. W., TeKoppele, J. M., Hanemaaijer, R., and DeGroot, J. (2003). Active MMPs captured by alpha 2 macroglobulin as a marker of disease activity in rheumatoid arthritis. *Clin. Exp. Rheumatol.*, 21(6):711–8.

Thompson, D., Pepys, M. B., and Wood, S. P. (1999). The physiological structure of human C-reactive protein and its complex with phosphocholine. *Structure*, 7(2):169–177.

Thorek, D. L., Robertson, R., Bacchus, W. A., Hahn, J., Rothberg, J., Beattie, B. J., and Grimm, J. (2012). Cerenkov imaging - a new modality for molecular imaging. *Am. J. Nucl. Med. Mol. Imaging*, 2(2):163–73.

Thorey, I. S., Roth, J., Regenbogen, J., Halle, J. P., Bittner, M., Vogl, T., Kaesler, S., Bugnon, P., Reitmaier, B., Durka, S., Graf, A., Wöckner, M., Rieger, N., Konstantinow, A., Wolf, E., Goppelt, A., and Werner, S. (2001). The Ca2+-binding proteins S100A8 and S100A9 are encoded by novel injury-regulated genes. *J. Biol. Chem.*, 276(38):35818–25.

Tins, B. J. and Butler, R. (2013). Imaging in rheumatology: reconciling radiology and rheumatology. *Insights Imaging*, 4(6):799–810.

Tummers, W. S., Kimura, R. H., Abou-Elkacem, L., Beinat, C., Vahrmeijer, A. L., Swijnenburg, R.-J., Willmann, J. K., and Gambhir, S. S. (2018). Development and Preclinical Validation of a Cysteine Knottin Peptide Targeting Integrin $\alpha v\beta 6$ for Near-infrared Fluorescent-guided Surgery in Pancreatic Cancer. *Clin. Cancer Res.*, 24(7):1667–1676.

Tzoumas, S., Deliolanis, N., Morscher, S., and Ntziachristos, V. (2014). Unmixing molecular agents from absorbing tissue in multispectral optoacoustic tomography. *IEEE Trans. Med. Imaging*, 33(1):48–60.

van de Ven, S. M. W. Y., Elias, S. G., Wiethoff, A. J., van der Voort, M., Nielsen, T., Brendel, B., Bontus, C., Uhlemann, F., Nachabe, R., Harbers, R., van Beek, M., Bakker, L., van der Mark, M. B., Luijten, P., and Mali, W. P. T. M. (2009). Diffuse optical tomography of the breast: preliminary findings of a new prototype and comparison with magnetic resonance imaging. *Eur. Radiol.*, 19(5):1108–1113.

van Eijk-Hustings, Y., van Tubergen, A., Boström, C., Braychenko, E., Buss, B., Felix, J., Firth, J., Hammond, A., Harston, B., Hernandez, C., Huzjak, M., Korandová, J., Kukkurainen, M. L., Landewé, R., Mezieres, M., Milincovic, M., Moretti, A., Oliver, S., Primdahl, J., Scholte-Voshaar, M., de la Torre-Aboki, J., Waite-Jones, J., Westhovens, R., Zangi, H. A., Heiberg, T., Hill, J., and EULAR (2012). EULAR recommendations for the role of the nurse in the management of chronic inflammatory arthritis. *Ann. Rheum. Dis.*, 71(1):13–9.

Van Lint, P. and Libert, C. (2007). Chemokine and cytokine processing by matrix metalloproteinases and its effect on leukocyte migration and inflammation. *J. Leukoc. Biol.*, 82(6):1375–81.

van Meurs, J. B., van Lent, P. L., van de Loo, A. A., Holthuysen, A. E., Bayne, E. K., Singer, I. I., and van den Berg, W. B. (1999). Increased vulnerability of postarthritic cartilage to a second arthritic insult: accelerated MMP activity in a flare up of arthritis. *Ann. Rheum. Dis.*, 58(6):350–6.

Verma, R. P. and Hansch, C. (2007). Matrix metalloproteinases (MMPs): Chemical-biological functions and (Q)SARs. *Bioorg. Med. Chem.*, 15(6):2223–2268.

Vermeij, E. A., Koenders, M. I., Blom, A. B., Arntz, O. J., Bennink, M. B., van den Berg, W. B., van Lent, P. L., and van de Loo, F. A. (2014). In Vivo Molecular Imaging of Cathepsin and Matrix Metalloproteinase Activity Discriminates between Arthritic and Osteoarthritic Processes in Mice. *Mol. Imaging*, 13:1–10.

Viemann, D., Strey, A., Janning, A., Jurk, K., Klimmek, K., Vogl, T., Hirono, K., Ichida, F., Foell, D., Kehrel, B., Gerke, V., Sorg, C., and Roth, J. (2005). Myeloid-related proteins 8 and 14 induce a specific inflammatory response in human microvascular endothelial cells. *Blood*, 105(7):2955–2962.

Vogl, T., Eisenblätter, M., Völler, T., Zenker, S., Hermann, S., van Lent, P., Faust, A., Geyer, C., Petersen, B., Roebrock, K., Schäfers, M., Bremer, C., and Roth, J. (2014). Alarmin S100A8/S100A9 as a biomarker for molecular imaging of local inflammatory activity. *Nat. Commun.*, 5:2329–2339.

Vogl, T., Gharibyan, A. L., and Morozova-Roche, L. A. (2012). Pro-Inflammatory S100A8 and S100A9 Proteins: Self-Assembly into Multifunctional Native and Amyloid Complexes. *Int. J. Mol. Sci.*, 13(3):2893–2917.

Vogl, T., Leukert, N., Barczyk, K., Strupat, K., and Roth, J. (2006). Biophysical characterization of S100A8 and S100A9 in the absence and presence of bivalent cations. *Biochim Biophys Acta*, 1763.

Vogl, T., Ludwig, S., Goebeler, M., Strey, A., Thorey, I. S., Reichelt, R., Foell, D., Gerke, V., Manitz, M. P., Nacken, W., Werner, S., Sorg, C., and Roth, J. (2004). MRP8 and MRP14 control microtubule reorganization during transendothelial migration of phagocytes. *Blood*, 104(13):4260–4268.

Vogl, T., Tenbrock, K., Ludwig, S., Leukert, N., Ehrhardt, C., Zoelen, M. A., Nacken, W., Foell, D., Poll, T., and Sorg, C. (2007). Mrp8 and Mrp14 are endogenous activators of Toll-like receptor 4, promoting lethal, endotoxin-induced shock. *Nat Med*, 13.

Wang, C., Bao, C., Liang, S., Fu, H., Wang, K., Deng, M., Liao, Q., and Cui, D. (2014). RGD-conjugated silica-coated gold nanorods on the surface of carbon nanotubes for targeted photoacoustic imaging of gastric cancer. *Nanoscale Res. Lett.*, 9(1):264.

Wang, S., Hossack, J. A., and Klibanov, A. L. (2018). Targeting of microbubbles: contrast agents for ultrasound molecular imaging. *J. Drug Target.*, pages 1–15.

Wang, Y.-T., Chiu, N.-T., Chen, M.-J., Huang, J.-J., Chou, H.-H., and Chiou, Y.-Y. (2005). Correlation of renal ultrasonographic findings with inflammatory volume from dimercaptosuccinic acid renal scans in children with acute pyelonephritis. *J. Urol.*, 173(1):190–194.

Waschkau, B., Faust, A., Schafers, M., and Bremer, C. (2013). Performance of a new fluorescence-labeled MMP inhibitor to image tumor MMP activity in vivo in comparison to an MMP-activatable probe. *Contrast Media Mol Imaging*, 8.

Weinblatt, M. E., Keystone, E. C., Furst, D. E., Moreland, L. W., Weisman, M. H., Birbara, C. A., Teoh, L. A., Fischkoff, S. A., and Chartash, E. K. (2003). Adalimumab, a fully human anti-tumor necrosis factor α monoclonal antibody, for the treatment of rheumatoid arthritis in patients taking concomitant methotrexate: The ARMADA trial. *Arthritis Rheum.*, 48(1):35–45.

Werner, S. G., Langer, H.-E., Ohrndorf, S., Bahner, M., Schott, P., Schwenke, C., Schirner, M., Bastian, H., Lind-Albrecht, G., Kurtz, B., Burmester, G. R., and Backhaus, M. (2013). Inflammation assessment in patients with arthritis using a novel in vivo fluorescence optical imaging technology. *Ann. Rheum. Dis.*, 72(1):156–156.

Wheeler, B. L., Nagasubramanian, G., Bard, A. J., Schechtman, L. A., and Kenney, M. E. (1984). A silicon phthalocyanine and a silicon naphthalocyanine: synthesis, electrochemistry, and electrogenerated chemiluminescence. *J. Am. Chem. Soc.*, 106(24):7404–7410.

Wooley, P. H., Seibold, J. R., Whalen, J. D., and Chapdelaine, J. M. (1989). Pristane-induced arthritis. the immunologic and genetic features of an experimental murine model of autoimmune disease. *Arthritis Rheum.*, 32(8):1022–1030.

Wu, R., Duan, L., Cui, F., Cao, J., Xiang, Y., Tang, Y., and Zhou, L. (2015). S100A9 promotes human hepatocellular carcinoma cell growth and invasion through RAGE-mediated ERK1/2 and p38 MAPK pathways. *Exp. Cell Res.*, 334(2):228–238.

Xu, K. and Geczy, C. L. (2000). IFN-gamma and TNF regulate macrophage expression of the chemotactic S100 protein S100A8. *J. Immunol.*, 164(9):4916–23.

Xu, K., Yen, T., and Geczy, C. L. (2001). Il-10 up-regulates macrophage expression of the S100 protein S100A8. *J. Immunol.*, 166(10):6358–66.

Yamaoka, K. (2016). Janus kinase inhibitors for rheumatoid arthritis. *Curr. Opin. Chem. Biol.*, 32:29–33.

Yang, S., Tian, H., Xiao, H., Shang, X., Gong, X., Yao, S., and Chen, K. (2001). Photodegradation of cyanine and merocyanine dyes. *Dye. Pigment.*, 49(2):93–101.

Yao, J. and Wang, L. V. (2011). Photoacoustic tomography: fundamentals, advances and prospects. *Contrast Media Mol. Imaging*, 6(5):332–45.

Yoshihara, Y., Nakamura, H., Obata, K. i., and Yamada, H. (2000). Matrix metalloproteinases and tissue inhibitors of metalloproteinases in synovial fluids from patients with rheumatoid arthritis or osteoarthritis. *Ann. Rheum. Dis.*, 59(6):455–461.

Zinnhardt, B., Viel, T., Wachsmuth, L., Vrachimis, A., Wagner, S., Breyholz, H.-J., Faust, A., Hermann, S., Kopka, K., Faber, C., Dollé, F., Pappata, S., Planas, A. M., Tavitian, B., Schäfers, M., Sorokin, L. M., Kuhlmann, M. T., and Jacobs, A. H. (2015). Multimodal Imaging Reveals Temporal and Spatial Microglia and Matrix Metalloproteinase Activity after Experimental Stroke. *J. Cereb. Blood Flow Metab.*, 35(11):1711–1721.

Zreiqat, H., Howlett, C. R., Gronthos, S., Hume, D., and Geczy, C. L. (2007). S100A8/S100A9 and their association with cartilage and bone. *J. Mol. Histol.*, 38(5):381–391.

A Abbreviations

ACPA	Anti-citrullinated protein antibody
AF443	MMP targeting ligand
AIA	Antigen induced arthritis
bCII	Bovine collagen type II
CCD	Charge-coupled device
CCP	Citrullinated protein
CD	Cluster of differentiation
CES271	S100A8/A9 targeting ligand
CIA	Collagen induced arthritis
CRP	C reactive protein
CSV	Comma separated values
CT	Computed tomography
CTGF	Connective tissue growth factor
CXCL	Chemokine (C-X-C motif) ligand
Cy5.5	Cyanine5.5
DAMP	Disease-associated molecular pattern
DAPI	4',6-diamidino-2-phenylindole
DAS	Disease activity score
DMARD	Disease modifying antirheumatic drug
ECM	Extracellular matrix
EM	Electromagnetic
EPR	Enhanced permeability and retention
ERK	Extracellular signal-regulated kinase
ESR	Erythrocyte sedimentation rate
Fc	Fragment crystallizable
FCS	Fetal calf serum
FDG	Fludeoxyglucose
FGF	Fibroblast growth factor

FLS	Fibrocyte-like synoviocyte
FMT	Fluorescence molecular tomography
FRET	Förster resonance energy transfer
FRI	Fluorescence reflectance imaging
GC	Glucocorticoid
H&E	Haematoxylin and Eosin
HKMT	Heat-killed mycobacterium tuberculosis
i.v.	Intravenous
ICAM	Intercellular adhesion molecule
ICG	Indocyanine green
IFN-γ	Interferon gamma
Ig	Immunoglobulin
IGF	Insulin-like growth factor
IL	Interleukin
IRAK	Interleukin-1 receptor-associated kinase
IRDye 800CW	Infrared Dye 800CW
kDa	Kilo-Dalton
L1	*see S100A9*
Mac-3	Lysosome-associated membrane protein 2
MAPK	Mitogen-activated protein kinase
MCP	Membrane cofactor protein
MCV	Mutated citrullinated vimentin
MFP	Mean free path
MHC	Major histocompatibility complex
MMP	Matrix metalloproteinase
MRI	Magnetic resonance imaging
mRNA	Messenger ribonucleic acid
MRP14	*see S100A9*
MRP8	*see S100A8*
MT-MMP	Membrane type matrix metalloproteinase

MTX	Methotrexate
NF-ϰB	Nuclear factor kappa-light-chain-enhancer of activated B cells
NIR	Near-infrared
NSAID	Nonsteroidal anti-inflammatory drug
OA	Osteoarthritis
OPO	Optical parametric oscillator
PA	Photoacoustic
PAMP	Pathogen-associated molecular pattern
PET	Positron emission tomography
PFA	paraformaldehyde
PKC	Protein kinase C
RA	Rheumatoid arthritis
RAGE	Receptor for advanced glycation end products
RAP1-GTP	Ras-related protein - GTP binding protein
RF	Rheumatoid Factor
ROC	Reciever operating characteristic
ROI	Region of interest
ROS	Reactive oxygen species
S100A8/A9	Heterodimer S100 protein A8 and A9
SBR	Signal to background ratio
SMC	Synovial mesenchymal cells
SPECT	Single photon emission computed tomography
TIMP	Tissue inhibitor of matrix metalloproteinases
TLR	Toll-like receptor
TMFP	Transport mean free path
TNB	Tris-NaCl-blocking
TNFα	Tumor necrosis factor alpha
US	Ultrasound
UV	Ultraviolet
VEGF	Vascular endothelial growth factor

Z	Atomic number

B List of Figures

1 Overview of Rheumatoid Arthritis progression 4
2 Arthritic Joint 5
3 Imaging modalities as a function of sensitivity and spatial scale 9
4 Jablonski diagram 11
5 ICG fluorescence characteristics 12
6 Imaging windows in the electromagnetic spectrum 13
7 FRI images of tracer distribution in organs *in vivo* and *ex vivo* 15
8 CES271-IRDye 800CW, S100A8/A9 tracer 19
9 AF443-Cy5.5, MMP Tracer 22
10 Image analysis Regions of Interest (ROI) 30
11 Experimental setup 32
12 Onset phase longitudinal imaging 33
13 S100A8/A9 and MMP signal in the onset phase 35
14 Resolution phase longitudinal imaging 37
15 S100A8/A9 and MMP signal in the resolution phase 38
16 Imaging and histological corroboration of target presence 40
17 Resolved inflammation and deformation 41
18 Single joint case study 42
19 Blood pool concentrations of MMP tracer in mouth region pre- and post-injection 43
20 FDG-PET in CIA 44
21 Thresholding of paws based on SBR to compare area and fraction methods . 46
22 Receiver operating characteristics of thresholded SBR images of MMP and S100A9 tracers in the onset and resolution phase 47

C List of Tables

1 Extra-articular symptoms and conditions related to Rheumatoid Arthritis . . 2

D Acknowledgements

My most sincere thanks to my thesis advisor and Doktorvater, **Michael Schäfers**, first and foremost for the opportunity to study and work at the EIMI. You saw potential in me before I had any experience in this field. I was very excited and you worked to temper this chaotic exuberance into a practical and efficient manner of work. I want to thank you for the funding opportunities that you have provided and encouraged me to apply for, it has allowed me the scientific autonomy to create projects, to start collaborations, to make mistakes, to work in labs internationally and to travel to many conferences around the world, which have helped me better understand and stay abreast of the many fields within molecular imaging as well as build a professional network. Not only professionally, but also personally, you supported me through a difficult time in my life, providing guidance and connections when I needed them most. Thank you for everything you have done for me.

As supervisor, **Sven Hermann**, you were absolutely integral to my time at the EIMI. I appreciate the almost daily support and discussions that have shaped my scientific knowledge and project trajectories. I want to thank you for the patience you showed during my development as a scientist. Not only do you help me and have your own projects but you also manage to keep abreast and support each project that passes through the EIMI. I find it inspiring and I know that without you, the EIMI would not be what it has been for me.

Thank you to the members of my committee, **Xiaoyi Xiang** and **Wiebke Herzog**. Xiaoyi, you helped recruit me at the beginning and I began my time in Münster in your lab. I am thankful for the opportunity to study here and that you have followed me throughout my PhD. Thank you Wiebke for your insightful and detailed approach during thesis committee meetings.

I am indebted to **Martin Wild** and **Sylvia Krüger** for their organization and work for the CiM-IMPRS Graduate School. You helped me get settled and provided support throughout my time as a PhD student in Münster.

I want to thank **Cristian Strassert** for the successful collaboration, exchange of ideas and teaching me so much about coordinated metal macrocycles. A great deal of the work during my PhD was facilitated by you and **Sebastian Wilde**. I appreciated your responsiveness and it has been a joy to work so closely with you.

Santi Nonell for his help setting up and conducting the initial Naphthalocyanine experiments as well as the generous use of his lab and the opportunity to feel at home among a fantastic team over four years. Caragols - **Oriol** and **Bea**, the ever helpful **Joachim** and **Roger**, **Ruben**, **Cormac**, **Jaume**, **Eli Bou**, and all of the **FotoQs**. Thank you for your help in the lab and your friendship outside of it. I'll always look back very fondly on our summers.

Thomas Vogl, **Johannes Roth** and **Stefanie Zenker** for the fruitful collaboration and

the experiments, analysis and grant applications that we undertook together. Your biological expertise and input regarding S100A8/A9 and Arthritis in general was invaluable.

I would like to thank **Andreas Faust** and the **EIMI chemistry group** for their work developing tracers, producing them, and aiding with analysis, as well as providing space for collaborations.

Michael Kuhlmann, thanks for letting us invade your office. You filled my first year with fun and also taught me a lot about my new home. I appreciate the work you put into writing the Tierversuchsanträge and your flexibility regarding experimental planning.

Christoph Denk for our collaboration. Although the work remains unfinished and did not make it into this thesis, it helped define my time at the EIMI and was an amazing experience, filled with stories. From our first meeting while Couch Surfing to your overnight trip driving from Vienna to your time in Münster to our trip to Hawaii. We learned to distrust literature together, we planned and dreamed and fought for our results.

Stefanie Fingerhut for her time and scientific input, which made the invisible quantifiable.

Alexa for her work helping to establish and maintain the MSOT machine here at the EIMI. And **Richard** for his help in carrying out MSOT experiments.

Thank you to the techs **Steffi**, **Sarah K.**, **Roman**, **Ina**, **Richard**, **Irmgard**, **Christa** and **Christina** for the help with practical planning, conducting and analysis of experiments throughout my time at the EIMI. It was through your efforts that I was able to conduct so many projects at the same time, through your flexibility that I was able to establish new protocols and through your patience and guidance that I was able to shed the name "Captain Chaos" and learn to work cleanly and efficiently. **Dirk**, **Sarah E.**, **Michael K.** and **Sonja**, thank you for the surgical help and interventions that you performed and taught me to perform. Thanks to **Wiebke**, **Nina**, **Sarah K.** and **Sandra** for help with ordering supplies and procuring so many SOP numbers.

The technical team that helped keep everything running deserves many thanks. **Klaus Schäfers**, **Christian**, **Sönke**, **Björn**, **Manny** and **Konstantin** thank you for programming SMARD and MEDgical, helping integrate my code, teaching me to use tools, managing my odd account setup, servicing the many machines we use to do our work and at one point, helping to fix my bike.

Nina Knubel for help with illustration and design as well as great conversations.

I want to thank **Bastian** and **Lisa** for initially "finding" me in the crowd of applicants and encouraging me to meet with Michael and to come to the EIMI. Not only did you manage to aid me to find a position, you helped me integrate with the team and helped me both at work and outside of work from the beginning of my time here until the very end and served

as good role models scientifically and great friends personally.

Mahesh for his initial work on the Arthritis project and for being a great friend in the first years of this PhD. I never felt like I was going it alone.

Florian for taking the time to help me understand the theoretical underpinnings of nuclear imaging modalities and the many wonderful discussions both at work and privately that brightened my time here in Münster.

Mirco and **Konstantin**, **Inga** and **Sarah E.**, **Lynn** and **Sarah K.**, thank you for the fun we had at work and outside of it. Each of you pitched in to fix the myriad small things that I needed help with day to day. And you were great friends, bringing humor and fun to our workplace.

As well as **Sonja**, **Katrin**, **Jeanette**, **Dominic**, **Cristina**, **Claudia**, and **Xin** for their scientific input in meetings and help and guidance in the lab.

Thanks to **Bastian**, **Lisa**, **Sarah E.**, **Lynn**, **Michael**, **Sven**, **Cristian**, **Thomas** and **Marta** for corrections to this thesis.

Thank you to **Elisabeth** for your help with so many organizational things and for nice weekly chats that pepped me up with times were tough.

I want to extend a thank you to everyone at the **EIMI**, named or unnamed, for all of the things, large and small, you each have done to bring me to this goal and to create for me a nice life here in Münster.

Thank you to **Krzysztof**, **John**, **Wojciech**, **Kamma**, **Marta**, **Eva**, **Haraldur**, **Hélène** and **Linda**. My friends near and far who each have played a role in everything from forming my critical thinking and providing intellectual inspiration to daily discussions and support, love and bringing times of happiness when things were difficult.

And finally, to my family. **Mom** and **Dad**, thank you for the love, emotional support and help you have given me over the past decade in higher education. And for the opportunities you have given me from the time I was young to explore my interests and expand my experiences. To **Collin**, thank you for looking out for, standing up for, putting up with, having fun with, being different from, and soldiering on with me. In some odd way, we've always been side by side. Love you all.

E Curriculum Vitae